The extremes of the *Fermi*-LAT energy ranges: the *Fermi* Low Energy (1FLE) catalog and a detailed investigation of HESS J1825-137 above 100 GeV

Die Extrembereiche der *Fermi*-LAT Energien: der *Fermi* Low-Energy (1FLE) Katalog und eine detaillierte Untersuchung von HESS J1825-137 oberhalb von 100 GeV

Der Naturwissenschaftlichen Fakultät
der Friedrich-Alexander-Universität Erlangen-Nürnberg
zur Erlangung des Doktorgrades Dr. rer. nat.

vorgelegt von
Giacomo Principe
aus Mirano (Venedig)

Als Dissertation genehmigt von der Naturwissenschaftlichen Fakultät der Friedrich-Alexander-Universität Erlangen-Nürnberg

Tag der mündlichen Prüfung:	
Vorsitzender der Promotionkommission:	Prof. Dr. Georg Kreimer
Gutachter:	Prof. Dr. Stefan Funk

Abstract

In the last decades, important improvements have been made in the γ-ray astronomy. Thanks to the fact that photons travel in straight lines it is possible to search and localize the sites where γ rays are produced in the Universe. Several γ-ray point-source analyses have been performed by space- and ground-based telescopes in the MeV to TeV energies. In particular, the imaging Compton telescope (COMPTEL) onboard NASA's *Compton Gamma-Ray Observatory* detected sources below 30 MeV, while catalogs of point sources released by the *Fermi* Large Area Telescope (LAT) and EGRET collaborations use energies above 100 MeV. Because the *Fermi* LAT is able to detect γ rays with energies as low as 20 MeV, a catalog of γ-ray sources detected in the energy range between 30 and 100 MeV is presented in this work for the first time. This catalog closes the gap of point source analysis between the COMPTEL catalog and the *Fermi*-LAT catalogs. The first part of this work contains the details of the analysis and results of the first catalog of γ-ray sources detected between 30 and 100 MeV with *Fermi* LAT.

Subsequently, a detailed study of the evolution of the pulsar wind nebula (PWN) HESS J1825-137 is presented. PWNe are archetypal celestial sources, in which it is possible to test the theoretical models for the particle acceleration mechanisms. The analysis of the HESS J1825-137 has been performed using 10 years of *Fermi*-LAT data between 1 GeV and 1 TeV.

The second part of this work focuses on the characterization and performance verification of the photon detectors planes (PDPs) for the camera of the medium-sized telescopes of the Cherenkov Telescope Array (CTA), which is the next generation ground-based observatory for γ-ray astronomy at very-high energies.

Zusammenfassung

In den letzten Jahrzehnten wurden wichtige Verbesserungen in der Gammastrahlungsastronomie erreicht. Dank der Tatsache, dass Photonen sich geradlinig bewegen, ist es möglich, ihre Entstehungsorte im Universum zu lokalisieren. Mehrfach wurde nach Gammastrahlung von Punktquellen mit Satelliten und bodengebundenen Teleskopen im Energiebereich von MeV bis TeV gesucht. Insbesondere das Compton Teleskope (COMPTEL), an Bord des NASA *Compton Gamma-Ray Observatory*, entdeckte Quellen unterhalb von 30 MeV, während Punktquellenkataloge, die von den *Fermi* Large Area Telescope (LAT) und EGRET Kollaborationen veröffentlicht wurden, nur Energien über 100 MeV verwendeten. Da *Fermi*-LAT Gammastrahlung mit Energien ab 20 MeV detektieren kann, wird ein Katalog von Gammastrahlungsquellen im Energiebereich zwischen 30 und 100 MeV in dieser Arbeit zum ersten Mal vorgestellt. Dieser Katalog schließt die Lücke der Punktquellensuche zwischen dem COMPTEL Katalog und den *Fermi*-LAT Katalogen. Der erste Teil dieser Arbeit enthält die Ergebnisse des ersten Katalogs von Gammastrahlungsquellen, die zwischen 30 und 100 MeV mit *Fermi* LAT entdeckt wurden, und die Details der Analyse.

Anschließend wird eine detaillierte Studie zur Entwicklung des Pulsar-Windnebels (PWN) HESS J1825-137 wird vorgestellt. PWNe sind gute Kandidaten, an denen theoretischen Modelle für Teilchenbeschleunigungsmechanismen getestet werden können. Die Analyse von HESS J1825-137 wurde unter Verwendung von 10 Jahren *Fermi*-LAT Daten im Energiebereich zwischen 1 GeV und 1 TeV durchgeführt.

Der zweite Teil dieser Arbeit konzentriert sich auf die Charakterisierung und Leistungsüberprüfung von photon detector planes (PDPs). Diese werden für die Kamera der mittelgroßen Teleskope (MST) des Cherenkov Telescope Array (CTA) entwickelt, welches die nächste Generation für bodengebundenen Gammastrahlungsastronomie bei sehr hohen Energien ist.

Contents

Part I

The construction of the *Fermi* Low Energy (1FLE) catalog and the analysis of the pulsar wind nebula HESS J1825-137

Preface

The first part of this thesis is dedicated to the study of γ-ray sources detected using *Fermi*-LAT data. Although LAT is able to detect photons with energies as low as 20 MeV, all previous catalogs released by the *Fermi*-LAT collaboration were produced using optimized analysis focused on energies larger than 100 MeV. In the same way, the EGRET telescope, which is a preceding γ-ray experiment, measured γ-rays from 20 MeV to 30 GeV. However, the catalogs released by the EGRET collaboration only used data above 100 MeV. At lower energies, COMPTEL analyzed the γ-ray sky between 0.75 and 30 MeV. Therefore, the energy range from 30 MeV to 100 MeV was not covered yet by any of the previous γ-ray point source (PS) analyses. Thanks to the fact that *Fermi* LAT can observe photons with energies as low as 20 MeV, a catalog of γ-ray sources detected in the energy range between 30 and 100 MeV is presented in this work for the first time.

The *Fermi* low energy catalog (1FLE) closes the gap of point source analysis between the COMPTEL catalog and the *Fermi*-LAT catalogs. One of the main challenges in the analysis of point sources is the determination of the background diffuse emission model. This thesis makes use of a background-independent method to search for point-like sources based on a wavelet transform implemented in the PGWave tool. The 1FLE contains 198 sources detected above 3 σ significance with eight years and nine months of *Fermi*-LAT data. In the 1FLE catalog, 189 sources are contained also in the *Fermi*-LAT Telescope third source (3FGL) catalog: 148 are extragalactic, 22 are Galactic, and 17 are unclassified sources in the 3FGL.

The last chapter of this part focuses on the study of the evolution of the pulsar wind nebula (PWN) HESS J1825-137. Despite observations of several PWNe many open questions remain. In particular, the mechanism of particles acceleration at the termination shock is not yet completely understood. The PWN HESS J1825-137 is an archetypal system where it is possible to test candidate models for the particle acceleration mechanisms. The analysis performed in this work has been performed with 10 years of *Fermi*-LAT data between 1 GeV and 1 TeV. The chapter presents also the first energy-dependent analysis of the PWN HESS J1825-137 made with *Fermi*-LAT data.

The first part of this thesis is structured as follow:

- The first chapter contains a brief introduction of the γ-ray science. In particular, it

introduces the celestial sources observed at γ-ray energies and the methods used for γ-ray detection.

- The second chapter presents the *Fermi* LAT instrument and standard analysis tools: the structure, the event reconstruction and the data analysis tools.
- The third chapter illustrates the wavelet transform method used for the point source analysis in this work.
- The fourth chapter is dedicated to derivation of the 1FLE catalog.
- The results of the first catalog of *Fermi*-LAT sources below 100 MeV are discussed in the fifth chapter.
- The sixth chapter presents the results of analysis of the PWN HESS J1825-137 performed using 10 years of *Fermi*-LAT data between 1 GeV and 1 TeV.

CHAPTER 1

Introduction on gamma-ray science

Already at the end of the 1940s, long before experiments detected the first γ-rays emitted by cosmic sources, scientists (i.e., Feenberg and Primakoff) predicted that the Universe should be producing such high-energy photons. Nowadays the γ-ray astronomy has reached remarkable progress and high-energy observations of the Universe represent a firmly established discipline in modern astrophysics.

Thanks to the fact that γ-ray photons travel in straight lines, from their origin to the Earth, it is possible to localize the sites where γ rays are produced in the Universe. The γ-ray observations provide important information about the physics of the cosmic objects, e.g., the possibility to constrain the particle acceleration mechanisms inside the source. The γ-ray radiation of relativistic particles has been detected on a wide range of astronomical scales: from compact objects such as neutron stars, with a mass starting from 1.1 $M_\odot$ (solar mass) (Özel et al. 2012), to cosmological scales such as other galaxies and active galactic nuclei (AGN), that have a mass up to 10^{10} $M_\odot$ (Kozłowski 2017).

In Section 1.1 a short summary about the history of the γ-ray observations is presented. The main science cases and questions for the γ-ray astrophysics are discussed in Section 1.2. Section 1.3 contains a review of the astrophysics objects producing γ-rays, as well a short description of the most important γ-rays sources, namely AGN and pulsar, that are also objects of study in the first part of this work. In the last section (Section 1.4) the two γ-rays observation methods, from space and ground, are discussed.

1.1 The history of the gamma-ray observations

Since γ rays coming from the space are absorbed by the Earth's atmosphere, balloons or spacecraft were initially used to search for γ rays. The first measurements were performed with a series of rockets and balloon experiments searching for γ-ray emission from the

sources of CRs. In 1958 a seminal paper by Morrison (Morrison 1958) presented first estimates of the fluxes of cosmic γ-ray sources (as a result of CR interactions).

After that space-based observatories started to be launched. The first satellites experiments were investigating γ ray in the energy region around 100 MeV. The first γ-ray telescope was carried into orbit with the Explorer 11 satellite in 1961 (Kraushaar & Clark 1962). It picked up less than 100 cosmic γ-ray photons. The observed photons were measured from all directions in the Universe, suggesting the possible existence of a uniform γ-ray background.

The series of satellites called Vela satellites (Klebesadel et al. 1973) were launched between 1963 and 1970, they were the first to detected γ-ray bursts. The first detection of significant γ-ray emission from the Milky Way was made in 1967 by the γ-ray detector aboard the OSO-3 satellite (Kraushaar et al. 1972). In total it detected 621 cosmic γ rays. Figure 1.1 shows the schematic of the OSO-3 telescope, on the left, and the γ-ray discovery map on the right.

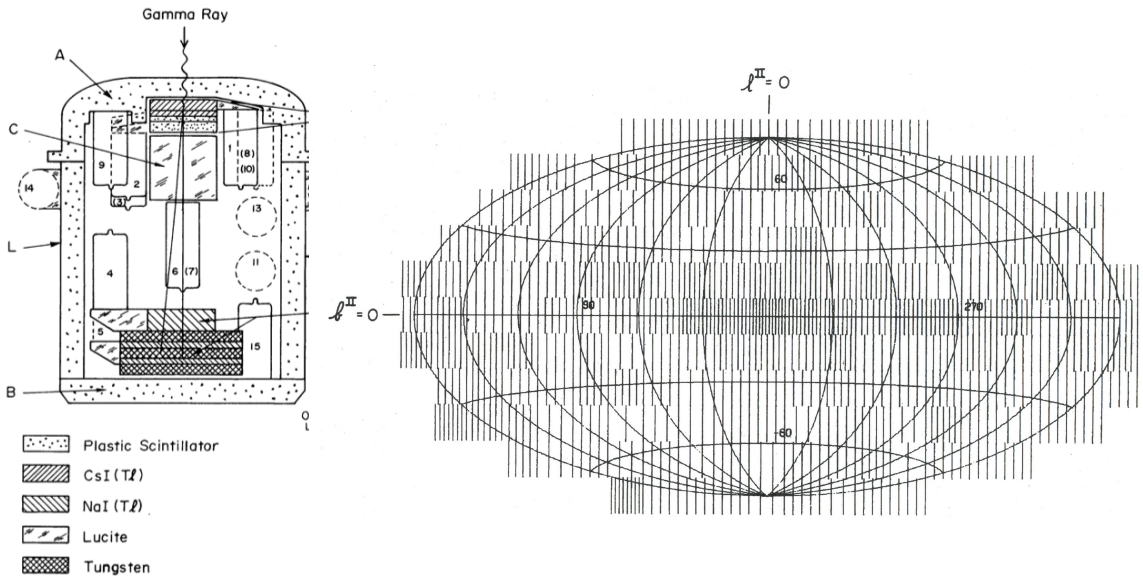

Figure 1.1: *Left: scale drawing of the OSO 3 detector. Right: the γ-ray discovery map, made with the data from Clark and Kraushaar's 1967 OSO 3 experiment. The number of γ-ray events recorded per solid angle on the sky is indicated by the density of vertical lines. The map illustrates the crucial concentration of events toward the center, which is the center line of the Milky Way. The plots are taken from Kraushaar et al. (1972).*

In the following years many improvements in the technology used in space-based detectors brought orders-of-magnitude improvement in the space instruments such as SAS-2 (Fichtel et al. 1975), COS-B (Bignami et al. 1975), and EGRET (Hartman et al. 1992). Starting in the 1950s, scientists have developed ideas for detecting high-energy γ rays from the ground using the Cherenkov light emitted in the atmospheric shower. They used the

fact that in the interactions between γ rays and the atmosphere, the primary γ rays transform into shower of particles that can be detected on the ground. Thanks to the measures of the secondary products it is possible to infer the properties of the astrophysical γ rays.

The first Cherenkov (optical) emission from atmospheric showers was detected in the early 1950s (Galbraith & Jelley 1953). From the early measurements it became clear that in order to study γ rays with Cherenkov detectors one needs to distinguish the showers created by gamma rays from the much more numerous showers created by hadronic cosmic rays. from those coming from astrophysical γ rays. Distinguishing them turned out to be really challenging. Jelley and Porter, in a paper published in 1963 (Jelley & Porter 1963), introduced the idea of distinguishing different shower developments in the atmosphere thanks to the image shape in the detector. More than twenty-five years have passed between the formulation of the idea and realization thanks to sufficient improvements in technology in order to allow the detection from ground at TeV γ-ray energies of the first astrophysical source (the Crab Nebula) (Weekes et al. 1989). In particular this result was reached thanks to the use of pixelated camera to exploit the difference in shape of the atmospheric shower between γ rays and protons, in order to suppress the large background. Another important step in the ground-based γ-ray observations was the use of stereoscopic systems connecting several imaging Cherenkov telescopes together in order to view the shower from different angles, further suppressing the background.

Current Cherenkov telescopes employ systems of more than one telescope with 1000 to 2000 pixels cameras, in order to cover a field of view of about 5°diameter. The Cherenkov telescopes are MAGIC (Aleksić et al. 2016), H.E.S.S. (Pühlhofer & for the H. E. S. S. collaboration 2018) and VERITAS (Park & VERITAS Collaboration 2015).

1.2 Science with gamma rays

A big advantage of γ rays compared to CRs is the fact that γ rays travel in a straight line and can reveal the sites of proton (and electron) acceleration in the Universe. This property is important to study both acceleration and propagation aspects of the study of CRs: the sites of particle acceleration are indicated by γ-ray sources, instead information about the propagation of relativistic particles in the interstellar medium is provided by the spatial distribution of the diffuse component of the radiation.

High energetic photons are formed in the interaction between accelerated charged particles (e.g., protons, nuclei, electrons, and positron) and interstellar gas, low energy photons, or magnetic field.

The places (and mechanisms), where the γ rays are originated, are the gas densities (pion decay and bremsstrahlung) and magnetic (synchrotron emission) or radiation (inverse Compton scattering) fields. It is possible to accurately resolve them thanks to multiwaveband studies of the region. The detection of γ rays allow the determination of the detailed spatial and energy distribution of high-energy charged particles in our Universe.

Apart from the fact that exploiting the acceleration and propagation mechanisms remains one of the major goal, other exciting aspects of the discoveries, connected to the γ-ray origins, have been revealed by recent observations (e.g. the detection of γ rays and gravitational wave from the merging of two neutron stars (Abbott et al. 2017) as well as the observation of a flaring blazar coincident with the high-energy neutrino IceCube-170922A (IceCube Collaboration et al. 2018)). Other interesting studies at γ ray energy are the physic of relativistic outflows, i.e., pulsar winds and AGN jets, as well other interesting issues related to cosmological probes of extragalactic radiation and magnetic fields using the beams of γ rays emitted by objects located at large redshifts.

To summarize, some of the key topics in the γ-ray astronomy are:

- the origin of the CRs: which sources provide the bulk of the galactic CRs? Which are the mechanisms responsible for CRs particle acceleration?
- DM annihilation: γ-ray observations gives the possibility to indirectly detect signatures of DM;
- relativistic outflow: the accretion of material onto black holes and other very compact objects often leads to the formation of a collimated jet of plasma. The formation and evolution of collimated jets are still not fully understood and could be better understood with γ-ray observations;
- cosmological questions: AGNs, the main extragalactic γ-ray sources, thanks to their large distances from us, can be used to understand the intergalactic medium and to test property of the quantum gravity.

1.3 Gamma-ray sources

Celestial objects produce γ rays with two possible emission mechanisms depending on the type of the accelerated particle that emits the photons: the leptonic emission and the hadronic emission. The spectrum of a leptonic emission has two main features: the synchrotron emission at low energy and the inverse compton (IC) emission at high energy. The hadronic emission is characterized by the synchrotron emission from secondary electrons at low energy and the π^0 decay at high energy.

Thanks to the improved facilities, in the last years, it has been possible to detect several thousand of γ-ray sources. The last general catalog released by the *Fermi*-LAT collaboration in the energy range between 100 MeV and 300 GeV, the 3FGL catalog (Acero et al. 2015), contains more than three thousands sources (see Figure 1.2).

Instead at higher energies, in the TeV range, the TeVCat catalog (Wakely & Horan 2008) contains more than two hundred sources. Below 30 MeV, the most recent COMPTEL telescope has detected 26 sources (Schönfelder et al. 2000). In the rest of this section, we survey models and main characteristics of pulsars and AGNs (see Sections 5.2.1 and 6).

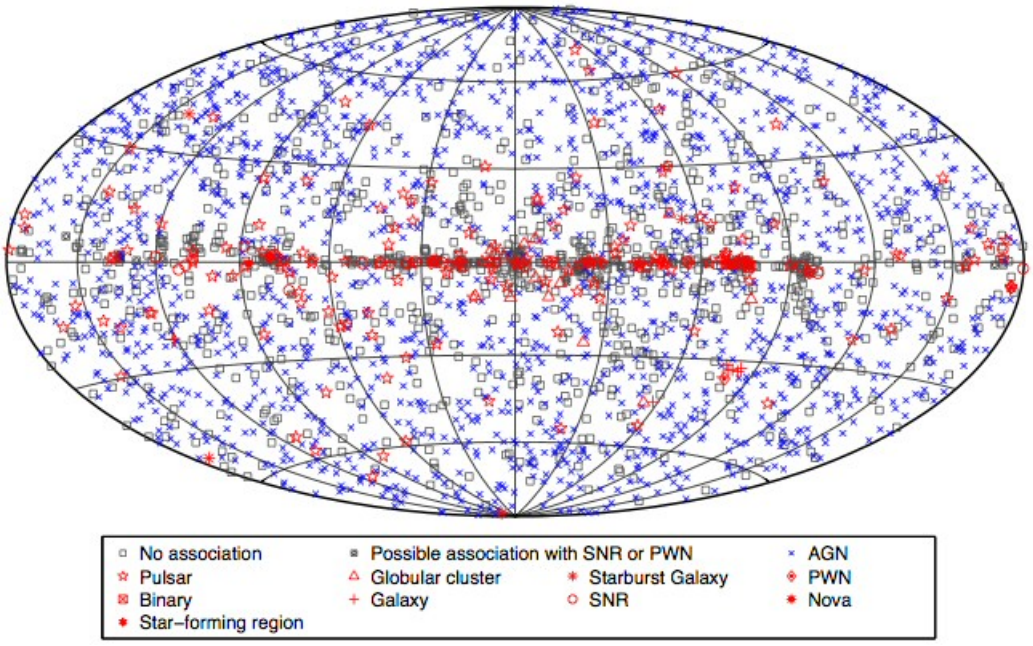

Figure 1.2: *Source map, in Galactic coordinates, of the celestial objects contained in the last general catalog, namely the 3FGL, released by the Fermi-LAT collaboration. The plot is taken from Acero et al. (2015).*

1.3.1 Gamma-ray pulsars and pulsar wind nebulae

The first sources identified in the γ-ray astronomy were pulsars. Only two sources, namely the Crab and the Vela pulsar were identified in 1970s. A pulsar is a highly magnetized rotating neutron star which emits a beam of electromagnetic radiation. Neutron stars (NSs) thanks to their rapidly rotating, strong magnetic fields are efficient particle accelerators. The accelerated particles (mostly electrons and positrons) are transported into a highly magnetized surrounding, which is an optimal environment to make them radiate high-energy γ ray (Caraveo 2014).

Gamma-ray pulsar detection

While in the radio wavelengths the pulsars can be detected by short-time pulsations, it is not possible to do the same in the γ-rays energies. In order to observe their pulsation in γ ray, i.e., to build a statistically significant light curve, photons collected over weeks to years have to be properly phased, folding their arrival times according to precise timing parameters. In particular the photon arrival time must be converted to the Solar System barycenter. Since this correction is position sensitive, a precise source position for performing a search for pulsations in γ rays is needed. Thanks to the high performances reached with the current γ-ray telescopes (e.g., *Fermi*, AGILE), it has been possible to detect more

than 100 pulsars so far (Abdo et al. 2013).

Gamma-ray pulsar model

At the end of the 1960s, Goldreich and Julian proposed that the pulsar magnetosphere is not a vacuum but it should be filled with plasma, since the induced electric force can win over the gravitational pull on surface charges (Goldreich & Julian 1969). This idea brought Sturruck to suggest the presence of a polar cap (PC) acceleration zone (Sturrock 1971). In the PC model the particles, accelerated by rotation-induced electric fields above the PC, are assumed to move along the dipole magnetic (B) field lines and produce curvature radiation. In this environment, photons above 1 GeV are absorbed by the B field and produce pairs of electron and positrons, which radiate synchrotron photons and produce a second generation of pairs. The process continues until the synchrotron photons no longer reach the energetic requirements for pair production and can escape to contribute to the high-energy pulsar emission. A coherent process, which involved remaining pairs, is responsible for the radio emission.

Later, thanks to measurements performed with COS-B on Vela and Crab, it was suggested that the measured γ- ray emission accounted for at least 10^{-3} of their rotation energy loss $\dot{E}$:

$$\dot{E}_{rot} = -4\pi^2 I \dot{P} P^{-3} \tag{1.1}$$

where P and $\dot{P}$ are the pulsar period and period derivative, respectively, whereas I is the moment of inertia assumed to be 10^{45} g cm^{-2}.

The slot gap (SG) model is ana alternative model developed by Arons (Arons 1981). In the SG model pair creations take place along favorably curved B-field lines above the PCs and far from the NS surface.

Despite the Crab presents similar light curves at all wavelengths, for Vela the light curves are radically different at different wavelengths (Bignami & Hermsen 1983). This motivated Cheng et al. (1986) to propose an outer magnetosphere model, wherein particles are accelerated within the vacuum outer gap (OG) extending from the null surface to the light cylinder. The γ rays are then produced far from the NS surface, mainly by curvature and synchrotron radiation of the accelerated particles. Figure 1.3 presents a modified version of the OG model designed by Chiang & Romani (1994).

With the EGRET instrument (Hartman et al. 1992) an old recycled millisecond pulsar (MSP) was observed for the first time. MSPs are characterized by extremely fast rotation coupled with a magnetic field significantly lower than that one of normal pulsars. Later on, it was observed that all pulsars exhibit a power law spectral shape with a high-energy cutoff (Thompson 2004). Figure 1.4 shows the main characteristics of all the gamma-ray pulsar detected with *Fermi*-LAT and contained in the last *Fermi*-LAT pulsar catalog (Abdo et al. 2013).

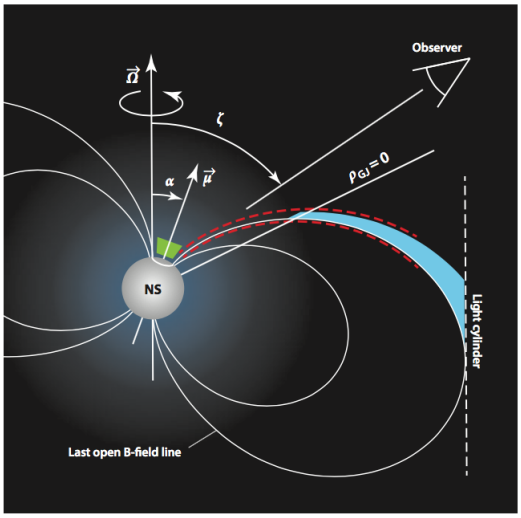

Figure 1.3: *Scheme of a neutron star (NS) magnetosphere. The internal emission regions are highlighted: polar cap (PC) model is in green, outer gap (OG) model in dark blue, and slot gap (SG) model in red. The plot is taken from Caraveo (2014).*

Pulsar Wind Nebulae

The supernova explosion, due to the collapse of a massive star, creates a stellar ejecta, with a mass of several solar masses, expanding at 10^4 km s^{-1} into surrounding circumstellar (CSM) medium. The ambient gas is heated and compressed by the resulting forward shock. As described in Slane (2017), when the material is swept by the shock, the deceleration drives a reverse shock (RS) back into the cold ejecta, heating the metal-enhanced gas to X-ray-emitting temperatures. The collapsed core is a rapidly-spinning, highly magnetic neutron star that generates an energetic wind of particles and magnetic field. Pulsar wind nebulae (PWNe) develop when the energetic particle wind collides with its surroundings, particularly with the supernova ejecta, forming a termination shock. The evolution of the PWN is determined by the properties of the central pulsar, its host supernova remnant (SNR), and the structure of the surrounding CSM/ISM.

Figure 1.5 shows a simulation of a PWN expanding into an SNR. The emission from the relativistic particles is a combination of synchrotron radiation and IC radiation associated with the upscattering of ambient photons. PWN can be used as natural laboratories relativistic astrophysics with the advantage of having a well localized energy source, the spin-down power of the pulsar.

1.3.2 Active Galactic Nuclei

Active Galactic Nucleus (AGN) is a compact region at the center of a galaxy that displays an extraordinary luminosity, up to 10^{49} erg s^{-1}, originated mainly by the central region.

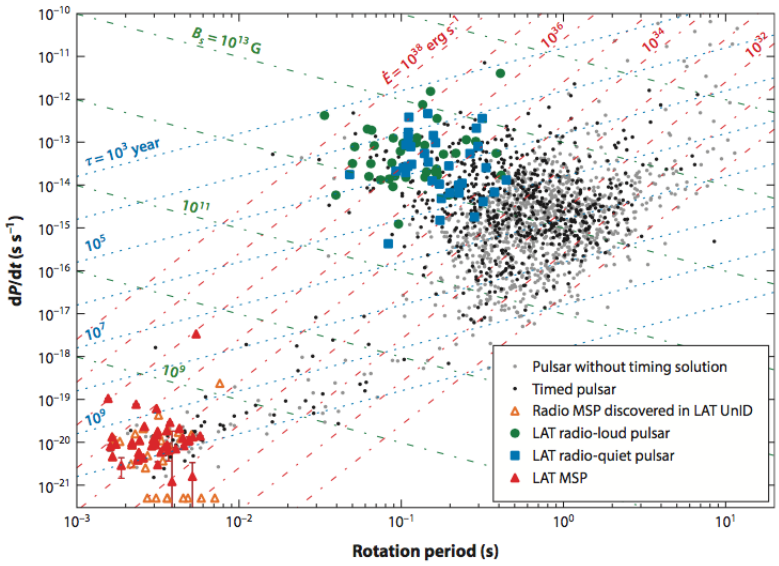

Figure 1.4: *P-Pdot diagram fro the known pulsars. The MSPs are represented with red triangles, radio-quiet pulsars with blue squares, radio-loud young ones with green dots. The black dots are timed but undetected pulsars in gamma-rays, and grey ones are pulsars for which we have not folded the gamma-rays. The horizontal line of triangles indicates the spin period of MSPs found in radio searches of Fermi unidentified sources, for which the spindown rate has not yet been published, and gamma-ray pulsations have not yet been seen. The plot is taken from Smith et al. (2017).*

A galaxy hosting an AGN is called an "active galaxy". AGNs are also used to probe the Universe on a cosmological scale, in order to understand the formation and evolution of the Universe. There are several types of active galaxies: Seyferts, quasars, and blazars.

Unified Model

The general accepted model for the AGN is illustrated in Figure 1.6. In the center, lies a Super Massive Black Hole (SMBH) with a mass in the range $10^6 \div 10^{10} M_\odot$ whose gravitational potential energy is the ultimate source of the AGN luminosity. The SMBH has a Schwarzschild radius $r_S = \dfrac{2GM_\odot}{c^2}$, between 10^{-7} pc and 10^{-3} pc. Matter pulled toward the black hole loses angular momentum through viscous or turbulent processes forming an accretion disk, which emits at ultraviolet and soft X-ray wavelengths. Clouds of gas moving rapidly in the potential of the black hole, the so called "broad-line clouds", produce strong optical and ultraviolet emission lines. Optical and ultraviolet radiation may be obscured along the lines of sight by a torus or warped disk of gas and dust located outside the accretion disk. Outside the torus, slower moving clouds of gas produce narrow emission lines. These are located in the Narrow Line Region (NLR), at about 100 pc from the SMBH. Some of the AGNs present outflows of energetic particles along the axis of the

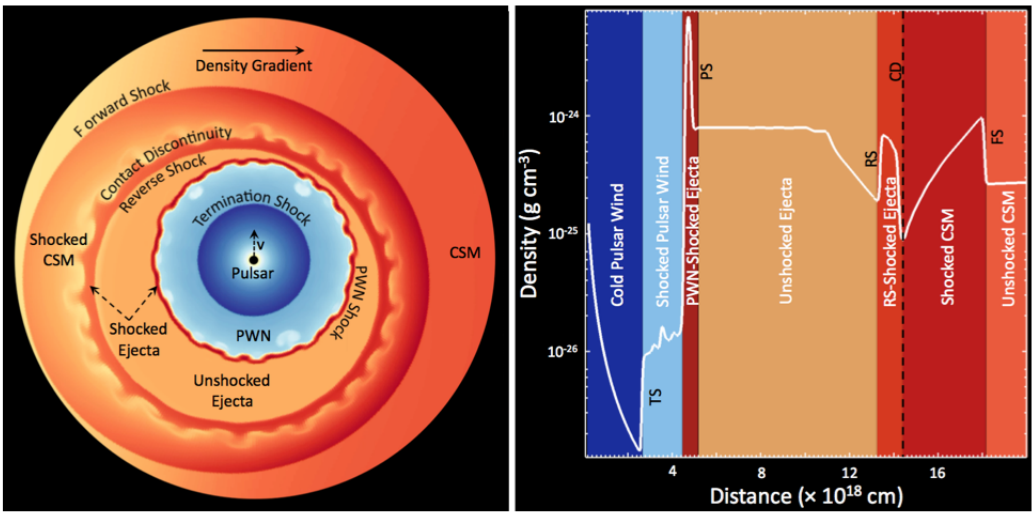

Figure 1.5: *Simulated image of a PWN evolving within its host SNR. The plot is taken from Slane (2017).*

disk or torus, forming collimated radio-emitting jets. The plasma in the jets streams outwards at very high velocity, beaming the radiation relativistically in the forward direction. The jets can extend for more than 1 Mpc from the central black hole and emits radiation at all wavelengths.

This asymmetric model of AGN implies radically different observational appearance depending on the viewing angle. This historically brought to different classes of sources, but all with the same physical properties.

Classification of Active Galactic Nuclei

The AGN Unified Model Antonucci (1993) differentiates the topologies of AGN classes by the different angle between the observer and the jet axis. If this angle is very small, the jet is almost pointing toward the observer, resulting in a strong continuum and an extreme variability, this object is called *blazar*. Increasing the angle, at first we may see the BLR, but then the dust torus starts to obscure the central region, so that only the NLR can be observed.

Following the guidelines of the classification based on the radio/optical flux ratio, the conventional separation of AGN in *radio-quiet* and *radio-loud* objects depends on the value of the flux ration between radio (5GHz) and optical (B band) emissions (Kellermann et al. 1989). In radio quiet objects the jet and jet-related emission can be neglected. Instead in radio-loud objects the contribution from the jet(s) and the lobes dominates the luminosity of the AGN, at least in the radio, but possibly at other or even all wavelengths. Based on the characteristics of their optical and ultraviolet spectra, AGN can be divided into the three main classes shown in table 1.1.

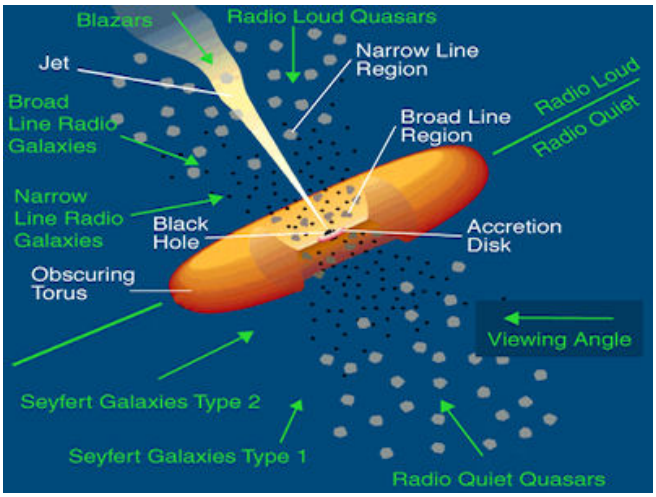

Figure 1.6: *A schematic figure for an AGN (not to scale). Surrounding the central black hole there is a luminous accretion disk. Broad emission lines are produced in clouds orbiting above the disk, this area is the Broad Line Region (BLR). A thick dusty torus (or warped disk) obscures the BLR from transverse line of sight; some continuum and broad-line emission can be scattered into those lines of sight by hot electrons that pervade the region. Narrow lines are produced in clouds much farther from the central source, this area is the Narrow Line Region (NLR). Radio jets, shown here as the diffuse jets characteristic of low-luminosity, emanate from the region near the black hole, initially at relativistic speeds.*

AGN taxonomy			
Radio Loudness	Type 2 (Narrow Line)	Type 1 (Broad Line)	Type 0 (Unusual)
Radio Quiet	Seyfert 2	Seyfert 1, QSO	
Radio Loud	NLRG (FRI,FR II)	BLRG (SSRQ, FSRQ)	Blazars (BL Lac,FSRQ)
Decreasing angle to line of sight →			

Table 1.1: *AGN classification adapted from Urry & Padovani (1995). In the Unified Model the passage from one type to another is driven by the change of the angle between jet and the line of sight.*

Blazar Optical Classification

Blazar's classification depends on the details of their appearance in the optical band where they emit a mix of three types of radiation: a non-thermal, jet-related, component; thermal radiation coming from the accretion onto the super-massive black hole and from the broad-line region, hereinafter BLR (at least in most radio-selected sources); and light from the host (giant elliptical) galaxy. The left plot of Figure 1.7 shows the *Fermi* blazar sequence exploiting the complete sample of blazars with known redshift detected by the *Fermi* satellite after 4 years of operations, 3LAC catalog (Ackermann et al. 2015). The right

plot shows the average (over 4 years) γ-ray luminosity as a function of the redshift. From the plot it is clear that BL Lacs have lower redshifts and smaller γ-ray luminosities (K-corrected, integrated in the rest frame 0.1–100 GeV band) than FSRQs.

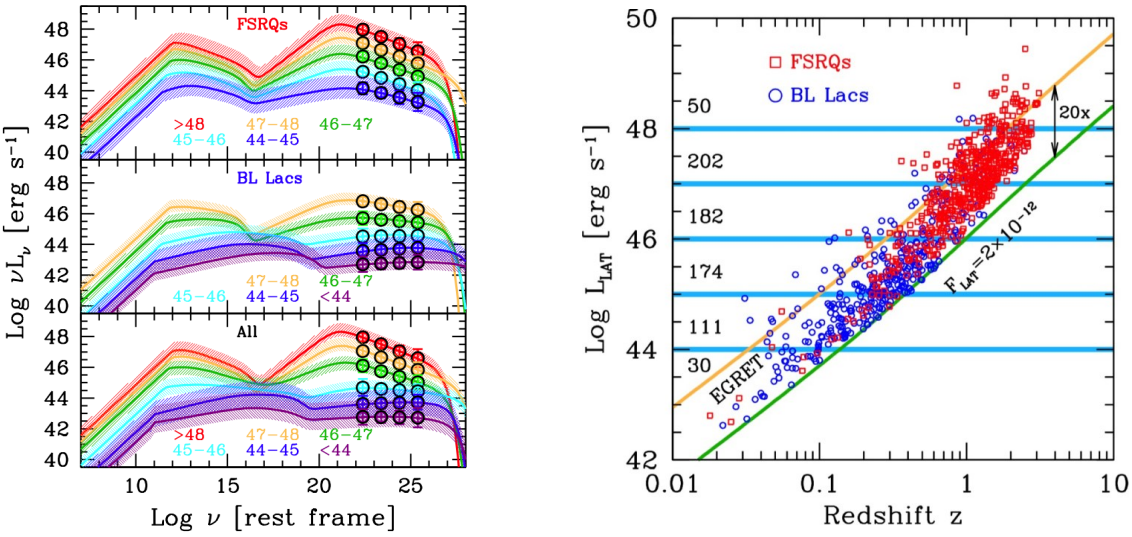

Figure 1.7: *Left: The Fermi blazar sequence Ghisellini et al. (2017), obtained for different bins of the logarithm of the γ-ray luminosities (indicated by the labels) for FSRQs only (top), BL Lacs (mid) and for all sources (bottom) contained in the 3LAC catalog Ackermann et al. (2015). Right: average (over 4 years) γ-ray luminosity as a function of the redshift. Blue circles are BL Lacs, red squares are FSRQs. The green line corresponds to a flux limit of 2×10^{-12} erg cm^{-2} s^{-1} in the 0.1–100 GeV band (appropriate for Fermi-LAT), and the orange line corresponds to an approximate limit for EGRET. The plots are taken from Ghisellini et al. (2017).*

Blazars are divided into the following three subclasses Giommi et al. (2012):

- Flat spectrum radio quasars (FSRQs), with the peak frequency of the synchrotron component detected in the IR-optical region and the high-energy γ-ray component dominating the luminosity.

- High-energy peaked BL Lac objects (HBLs, above all X-ray selected BL Lac objects), with the synchrotron-peak frequency generally located in the UV/soft-X-ray region and the high and low energy components showing similar luminosity.

- Low-energy peaked BL Lac objects (LBLs, above all radio selected BL Lac objects) with luminosity and synchrotron-peak frequency intermediate between the above sub classes.

1.4 Gamma-ray observation methods

The energy range covered by the γ-ray observations is of about 7 decades and, since a typical flux index of the γ-ray sources is around 2 ($F \sim E^{-2}$), an expected flux difference between the low- and high-energy range is of 14 decades. Namely at low-energy (around 100 MeV), a bright source, such as the Vela pulsar, presents a flux of $\sim 10^{-1}$ photons m^{-2} s^{-1} (or the Crab Nebula, $\sim 10^{-3}$ photons m^{-2} s^{-1}), while the brightest sources at the high-energy boarder, i.e., the Crab Nebula, has a flux of $\sim 10^{-7}$ photons m^{-2} s^{-1}. Although the best solution to cover the entire energy range will be to build instruments with detection areas that are as large as possible, in the low-energy range detectors with an area of less than a square meter are appropriate, whereas in the high-energy range (>50 GeV) detectors areas of several hundreds of square meters are needed. Therefore it is not possible with a single technique or instrument to cover the whole energy range.

All γ-rays are blocked by the atmosphere from reaching the ground. Therefore, their direct detection is possible only with space-based instruments. At higher energies, since it is not possible to deploy in space instruments with a large dimension, a ground-based technique is needed. While in space it is possible to directly observe γ rays, ground-based telescopes operate on the principle of detecting secondary products of the interaction between γ rays and the atmosphere. Two techniques are currently adopted for the γ-ray observation with ground-based telescopes: imaging atmospheric Cherenkov telescopes (ICATs) and water Cherenkov telescopes.

Figure 1.8 show the differential sensitivity of the existing and under-construction space (*Fermi*-LAT) and ground (H.E.S.S. and CTA for the IACTs, and HAWC for the water Cherenkov telescopes) based telescopes.

1.4.1 Space based gamma-ray observations

The principle used by the space-based telescopes to detect γ-ray is the pair production in the detector. They usually observe the sky in the energy range between $\sim$ 20 MeV and $\sim$ 300 GeV, whereas at higher energy a much larger detector is needed. A space-based γ-ray detector is usually made by the following elements:

- a tracker, it measures the tracks of the electron and positron produced in the pair creation of the γ-ray,
- a calorimeter: it measures the energy of this electron-positron pair (consequently also of the primary γ-ray),
- anticoincidence detector: it is used for the veto of the charged-particle background.

An advantage of the space-based telescopes over the ground-based ones, is that the space detectors can be calibrated in the laboratory.

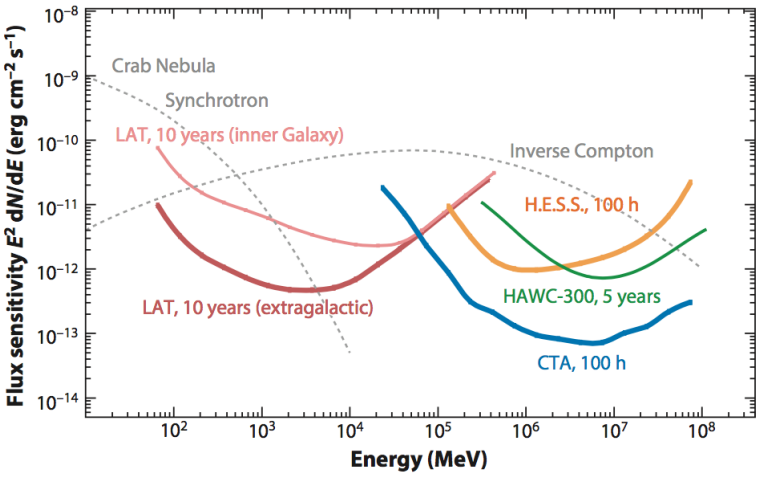

Figure 1.8: *Differential sensitivity (integral sensitivity for 4 bins of energy per decade) for a minimum significance of 5σ in each bin, minimum 10 events per bin. For comparison, the synchrotron and inverse Compton measurements for the brightest persistent TeV source, the Crab Nebula, are shown as dashed gray curves. The plot is taken from Funk (2015).*

One of the first γ-ray satellites was COS-B. It was launched in 1977 and it was the first to produce a detailed map of the sky at γ-ray wavelengths (Swanenburg et al. 1981).

The existing γ-ray satellites are *Fermi* (Atwood et al. 2009) and AGILE (Astrorivelatore Gamma ad Immagini Leggero - Light Imager for Gamma-ray Astrophysics) (Tavani et al. 2009).

The *Fermi* γ-ray space telescope is described in detail in the following Chapter 2.

1.4.2 Ground-based gamma-ray observations

Ground-based observatories indirectly detect γ rays measuring the secondary products of the interaction between γ rays and the atmosphere. As described in Völk & Bernlöhr (2009) pairs of $e^{\pm}$ are produced in the atmosphere, at an altitude of about 10 to 20 km, from high-energy cosmic γ rays. Due to Bremsstrahlung they create over the next radiation length new γ rays, which generate new pairs, etc., making a shower of $e^{\pm}$ until the energy of the final generation of electrons becomes so small that the ionization mechanism dominates. The result of these processes is called electromagnetic air shower It exists for about 10^{-4} seconds while traversing the atmosphere. Since it is not possible to reproduce this effect in the laboratory the most realistic and complete description of the physical processes and the corresponding results in the detector(s) is given by Monte Carlo (MC) simulations

Not only γ rays penetrate into the atmosphere, but also charged energetic nuclei (cosmic rays). Most of them are protons. They undergo hadronic interactions producing mainly neutral (π^0) or charged ($\pi^{\pm}$) pions. The neutral pion subsequently decays into two gammas

producing again pairs of $e^{\pm}$, instead the charged pions produce electrons positrons and two neutrinos via the $\pi \rightarrow \mu \rightarrow e$. The background air showers are therefore a mix of hadronic and electromagnetic nature. In particular due to the large transverse momentum transfer in hadronic interactions the hadronic shower component is broad and irregular compared to the electromagnetic component (see Figure 1.9). Since the flux of cosmic-ray particles is much larger (a factor of about 10^3) than that of γ rays, a large background is observed in the ground-based γ-ray astronomy. Because no anti-coincidence shield can be applied as in space detectors, the background signal needs to be separated from the γ-ray signal directly in the data. Despite some asymmetry, the shower image of a γ ray in the camera has the shape of an ellipse. The orientation of major axis of the ellipse indicates the direction of incoming $e^{\pm}$ shower. It is also possible to distinguish the gamma shower from the hadronic one in the camera looking at the shape of the ellipse. The hadronic shower has a broader and more irregular shape compared to a shower originating from a gamma ray.

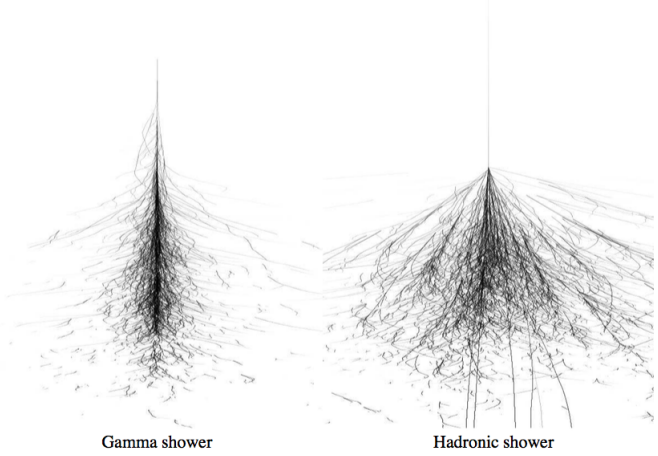

Figure 1.9: *The two plots show the different character of γ showers and hadronic showers. The γ shower is narrow and approximately axially symmetric about the direction of the primary photons. Instead the hadronic shower is irregular and broad since it may contain several electromagnetic subshowers. The figure is taken from Bernlöhr (2008).*

For a given γ ray of about 100 GeV only few energetic photons or electrons reach the ground, the electron shower from the original γ ray are still observable with optical telescopes through their Cherenkov radiation in the optical range. Since at the edge of the light pool most of the light from a γ-ray shower arrives within few ns, it is necessary to use fast photomultiplier cameras for the telescopes in order to observe the Cherenkov light and to suppress the dominant night sky background. An alternative is to observe the Cherenkov light emitted by the seondary particles when they interact with material (e.g., water) inside big tanks.

Imaging atmospheric Cherenkov telescopes

The IACTs project the Cherenkov light of the air showers with mirrors onto a fast camera, positionated at focal plane of the mirrors. They measure the angular distribution of the Cherenkov light from the air showers.

Due to the weakness of the Cherenkov light, they require large light collection devices. The atmospheric Cherenkov light emission from a single particle is characterized by a forward cone with an opening angle $\theta \sim 1^\circ$ that increases downwards. The Cherenkov light (mainly blue) arrives in a ring on the ground with a typical radius of$\sim$ 120 m at an altitude of $\sim$2,000 m.

For background rejection and for the angular resolution stereoscopic observations are used. They significantly suppress hadronic showers in which long-lived muons can trigger individual telescopes. The spacing of the telescopes is therefore on the order of $\sim$100 m.

Figure 1.10 shows a schematic picture of a shower from a cosmic γ-ray source, illuminating an array of IACTs on the ground. The observation time of IACTs is limited to clear and moonless nights.

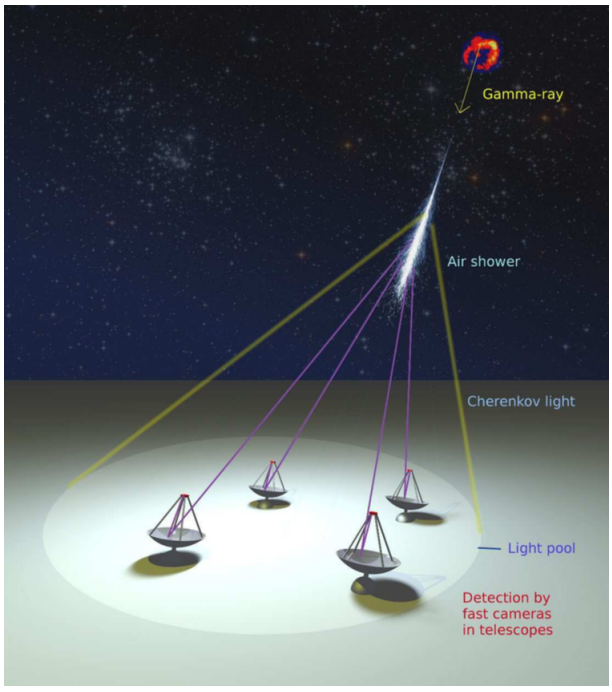

Figure 1.10: *A schematic representation of a Cherenkov light pool that illuminates an array of telescopes. The figure is taken from Bernlöhr (2008).*

The currently working IACTs are MAGIC (Aleksić et al. 2016), H.E.S.S. (Pühlhofer & for the H. E. S. S. collaboration 2018) and VERITAS (Park & VERITAS Collaboration 2015). The Cherenkov telescope array (CTA, CTA Consortium (2017)), the next generation of IACTs, is presented in the second part of this work.

Water Cherenkov detectors

While IACTs detect the Cherenkov light of the shower particles in the atmosphere, water Cherenkov detectors detect the Cherenkov light of the shower particles inside the detector (water tanks). They operate at a higher energy threshold than IACTs, because they require the shower particles to reach the ground. Therefore the detectors are typically located at higher altitudes. Thanks to the combination of a large field of view and a nearly 100% duty cycle, these detectors are well suited for studying transient sources and performing unbiased sky surveys. Since the water Cherenkov detectors require the particles to reach the ground, therefore the disadvantage is that threshold is usually higher ($\sim$100 GeV) than IACTs' one, but they have the advantage that they can operate continuously, instead the IACTs can operate only in the dark, at nighttime, in order to be able to detect the faint Cherenkov light emitted by the particle shower.

The high altitude water Cherenkov observatory (HAWC, HAWC Collaboration et al. 2013) is the main existing water Cherenkov detector. It consists of 300 steel tanks, each 4 m high and 7.3 m in diameter, holding 188,000 L of water. It is located at Sierra Negra in Mexico at an altitude of 4,100 m. Figure 1.11 presents the photo of the HAWC observatory. It follows the principle tested by its predecessor Milagro (Atkins et al. 2000), where the water Cherenkov technology for γ-ray astronomy has been successfully proven.

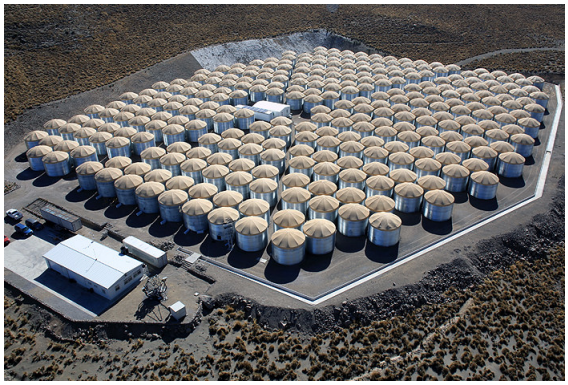

Figure 1.11: *Photo of the HAWC observatory located at Sierra Negra in Mexico at an altitude of 4,100 m. The photo is taken from Nisa (2018).*

CHAPTER 2

The *Fermi* gamma-ray space telescope

The *Gamma-ray Large Area Space Telescope* (GLAST) satellite (Ackermann et al. 2012) has been successfully launched on 11 June 2008. It is orbiting around Earth at an altitude of $\sim$ 565 km and with an orbital inclination of 25.6°. The satellite was then renamed as *Fermi Gamma Ray Space Telescope* after starting its scientific mission on 11 August 2008.

The aim of the mission is to observe the sky in the γ-ray energy band. In particular some of the main objectives are:

- to explore the most extreme environments in the Universe and the origin of cosmic ray;
- to determine the origin of the diffuse γ-ray background;
- to study the process of particle acceleration in Galactic and extragalactic sources;
- to study the energy of gamma-ray bursts (GRBs);
- to search for signals from Dark Matter;
- to explain how black holes accelerate immense jets of material to nearly speed of light.

With its two instruments it has an energy coverage that goes almost continuously from 8 keV to 300 GeV (until 2 TeV with the new Pass8). This makes the *Fermi* satellite a fundamental instrument to connect the X-ray observations with the data taken in the TeV band by ground-based Cherenkov telescopes.

The *Fermi* spacecraft operates in different observing modes. Transitions between modes may be operated from ground or autonomously. The *survey mode* is the primary observing mode for *Fermi*. In this mode the satellite scans the whole sky. During the orbit it sweeps the sky from the local zenith to the celestial pole with an angle named *rocking angle*. At

the end of each orbit, the satellite turns on the other side of the orbital plane and continues the observations looking the other hemisphere in the same way. Uniformity of exposure is achieved by *rocking* the pointing perpendicular to the orbital motion. The default profile rocks the instrument axis 35°north for one orbit, then 35°south for one orbit, resulting in a two-orbit periodicity (one orbit lasts around 90 minutes). The maximum rocking angle is 60°. The current rocking angle is 50°. Therefore, thanks to its large field of view, *Fermi* can observe uniformly the sky every 3 hours. It occasionally operates in *pointing mode* to study interesting transient phenomena like GRBs. The pointing accuracy is $< 2°(1\sigma$, goal of $<0.5°)$, and the uncertainty of the pointing is <10 arcsec (goal <5 arcsec).

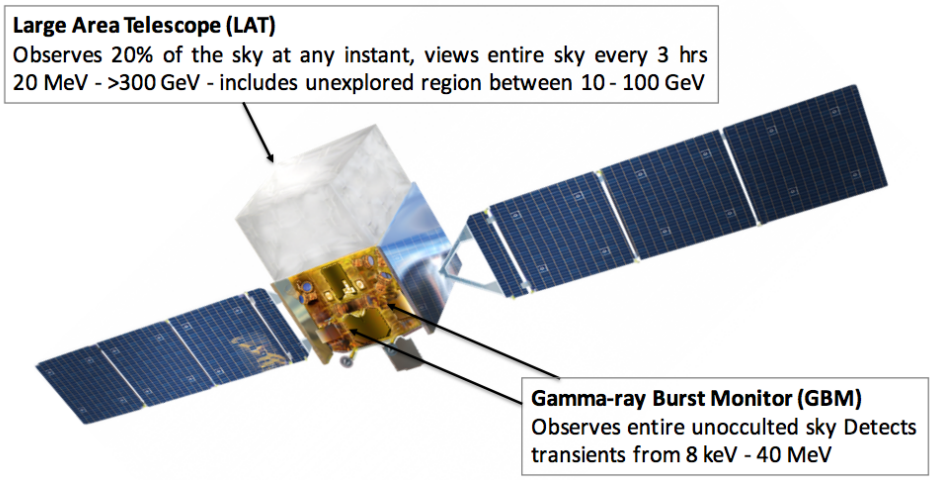

Figure 2.1: *The Fermi satellite with the position of its two instruments: the LAT and GBM.*

As it is shown in Figure 2.1, the spacecraft contains two instruments:

- the *Gamma-Ray Burst Monitor* (GBM) covers the energy band between 8 keV and 40 MeV,
- the *Large Area Telescope* (LAT) for the energy range from 20 MeV to 2 TeV.

The GBM (Meegan et al. 2009) is dedicated to the analysis of transient sources like GRBs and transient phenomena. It is made by two different kind of scintillation detectors with a time resolution of 2 μs. The first one is composed by 12 Sodium Iodide (NaI) disks, each one connected directly with a photomultiplier tube (PMT) and covering an energy range that goes from 8 keV to 1 MeV. The second one is composed by two Bismuth Germanate (BGO) cylinders, each of them with two PMTs connected, sensitive to the energy band between 150 keV and 40 MeV, providing also an overlap with the NaI detectors. Three NaI detectors are located in each corner of the spacecraft, oriented in different direction for a better sky coverage. The BGO cylinders are mounted on the opposite side of the satellite.

The LAT (Atwood et al. 2009), the main instrument onboard the *Fermi* satellite, is a pair conversion telescope. Thanks to its large field of view (2.4 sr), in a single orbit it can cover 75% of the sky. More details of this telescope are presented in the following sections.

2.1 The Large Area Telescope

The LAT is a wide field-of-view (FoV) imaging γ-ray telescope with large effective area combined with good energy and angular resolution. Its key feature is the wide effective area for the e^+e^- pairs production in the interaction of gamma photons with matter.

The LAT is a pair conversion detector: γ-rays penetrate into the detector (the tracker) and interact with a high Z converter material, in this case tungsten, to produce an electron-positron pair. This pair is tracked through the instrument by silicon strip detectors. Since the γ-ray energy is much larger than the rest mass of the electron and positron, both particles will travel predominantly in the direction of the incident photon. Therefore the reconstructed direction on the incoming γ-ray is limited by multiple scatterings of the pair components in the tracker material as well as the spatial resolution of the tracker. At the bottom of the LAT a calorimeter made of CsI (Tl) is placed, which provides the measurement of the energy.

2.1.1 LAT Structure

The LAT is a pair conversion detector composed by a 4×4 array of towers (measuring 43.25 cm × 43.25 cm × 84 cm). A segmented anti-coincidence detector, used to reject the background signal due to the incoming charged particles, covers the tracker array. In each tower a converter-tracker module is located on top of the corresponding calorimeter module while on the bottom the tower electronic modules (TEM) are placed with a programmable trigger and data acquisition system (DAQ). A foam thermal blanket surrounds everything, providing a light-tight cover and preventing damage by micro-meteor hits. Figure 2.2 provides a cutaway view showing the design of the LAT.

The anti-coincidence detector

The anti-coincidence detector (ADC) is the first defense of the LAT against the large background given by charged cosmic rays. In fact it has the role to discriminate between photons and charged particles, the latter have a flux over five order of magnitude higher than the γ-ray flux. The shielding is made of segmented plastic scintillators in polyvinyl-toluene (PVT) with 89 sections, each one connected through wavelength-shifting fibers to 2 PMTs. The design efficiency in the rejection of unitary charged particles is 99.97%, averaged on the 8.6 m^2 of the detector surface.

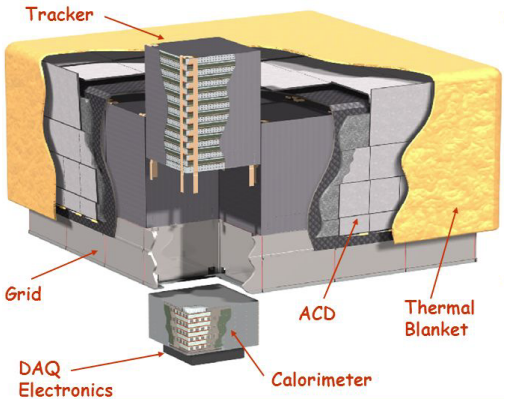

Figure 2.2: *Cutaway view showing the design of the LAT. Each tower in the 4×4 array includes a tracker module and a calorimeter module. Its real dimensions are* 1.8 m × 1.8 m × 0.72 m.

The tracker

The tracker has two different aims: to convert the photon in a e^+e^- pair and to reconstruct the particles path in order to obtain the original photon trajectory. It is constituted by an array of 4×4 columns of 40×40 cm^2 with 18 layers in a carbon structure. The first 16 trays are made of 2 silicon strip detectors (SSD) and they are spaced by tungsten foils. This metal has an atomic number $Z = 74$, in order to increase the pair production cross section (which increases with Z^2).

The calorimeter

Below each tower is positioned a calorimeter module of 96 CsI crystals doped with Thallium. The crystals are arranged in eight-layers rotated by 90° with respect to the upper one, forming an $x - y$ array. They are read out by photo-diodes at each sides, giving both longitudinal and transverse information about the energy deposition pattern. The calorimeter provides the measurement of the energy deposited by the shower initiated by a e^+e^- pair, as well the reconstruction of the shower development, in order to discriminate hadronic showers.

The trigger

The trigger analyzes signals from the tracker, the calorimeter and the ADC. A trigger from the tracker is sent in case of a signal present in at least three $x - y$ layers in a row. The calorimeter has instead two primitive triggers, the CAL-LO that is provided when a single calorimeter log has an amount of released energy > 100 MeV, and the CAL-HI for an amount of released energy greater than 1 GeV. The trigger signal provided by the ACD distinguishes the discriminating signals between charged particle signal near a triggering tower and heavy nuclei of carbon, nitrogen and oxygen (CNO). Those triggers are also

used for calibration purposes. In addition to *physical-event* triggers, a periodic trigger is used to monitor the performance of the instrument.

The DAQ

Triggers and readout phases are managed by the DAQ. It also performs an onboard filtering of the collected data, in order to reduce the transmission event rate and to provide a quick answer to transient phenomena. The DAQ processes the captured event data into a data stream with an average bit rate of 1.2 Mbps for the LAT.

2.2 Event Reconstruction and Classification

The event analysis process performed on ground starts as soon as the data are downlinked to Earth. If one considers that the LAT detects several hundred events every second, this is particularly challenging because it is needed to transform the individual channel signals into a particle interaction pattern.

The main steps of the event analysis process can be summarized as follows.

- Data are decompressed and individual channel information are converted to more physically motivated pattern (e.g. grouping signals in the ACD by tile).
- The reconstruction of the event is achieved by applying pattern recognition and fitting algorithms commonly used in high-energy particle physics experiments. Individual tracker tracks and energy clusters in the calorimeter are correlated to signals in the ACD. Therefore figures of merit for events are created.
- Various analysis techniques are then used to determine the energy and direction of the event, as well to verify if the event is really due to a γ-ray interaction.
- Event selection criteria are applied to populate the various γ-ray event classes.

In addition to these procedures, the processing pipeline automatically verifies the data integrity at each step and provides all the ancillary data products related to calibration and performance monitoring of the LAT.

The development of the analysis process initially was based and strongly relied on detailed MC simulation of the instrument, and its validation through an on-ground calibration with muons and a beam-test campaign. After the beginning of the mission, the instrument response functions (IRFs), which provide the description of the instrument performance used for data analysis, have been corrected for the discrepancies observed between real (flight) and simulated data (for more information see also Ackermann et al. (2012)).

LAT Monte Carlo modelling

The MC modelling of the LAT has been fundamental for both the event analysis and the studies of the instrument performance, in particular during the pre-launch phase when the instrument and the software infrastructures were designed and developed.

The validation of MC models of the LAT was performed through an on-ground calibration with muons and a beam-test campaign on a "calibration unit", made with detector modules with the same characteristics of those used to build the LAT, including two complete tracker/calorimeter towers. The calibration unit was exposed to photons (up to 2.5 GeV), electrons (between 1 and 300 GeV), hadrons (π and p, from a few GeV to 100 GeV) and ions (C, Xe, 1.5 GeV/n) in different irradiation facilities (Baldini et al. 2007).

Parallel to the on-ground calibration, a further more detailed calibration was scheduled to be carried out in orbit. The calibration effort started after *Fermi* launch and the first results are provided in detail in Abdo et al. (2009a). The LAT performance was fine-tuned by optimizing internal delays and synchronizations, alignment constants and absolute timing.

Track and energy reconstruction

Clusters of spatially adjacent hits in the tracker are combined to determine a three dimension position in the detector thus generating track hypotheses. Two different algorithms are used to generate tracks. The first one is based on the centroid and axis of the energy deposition in the calorimeter. The second one is searching for the line connecting the putative first hit to the deposition centroid in the calorimeter.

Concerning the energy reconstruction, the first step is the conversion of the raw signal into energy depositions for each crystal end. The sum of the energies deposited provides the first raw estimate of the event energy, while the direction of the shower is derived from the 3D centroid and higher moments of the energy deposition.

The first energy estimate is done summing all the energy released in the calorimeter, after which several different algorithms are correcting this rough estimate using the information obtained by the track reconstructions.

Event classification and Background rejection

The intent of the event classification is not only the estimate of the best event direction and energy, but also the reduction of the background in the final data sample. For these aims a series of selection criteria and classification tree generated probabilities (Breiman et al. 1984) are used.

For the determination of the direction, at first, a classification tree selects between the vertex solution, if available, and the best one-track solution. Events are then divided

into four subclasses, according to the conversion point, in the *front* or *back* section of the tracker, and to the vertex properties, namely vertex or one-track events. At the end of the process a best energy and a best direction measurement are assigned to each event, along with the corresponding estimates of the accuracy of the measurements.

After the reconstruction of energy and direction, an additional background rejection stage is applied, improving the on-orbit filtering. The onboard filter is configured in order to reduce the data to fit the available band for the data downlink to the Earth while keeping the largest possible efficiency for γ-ray detection (reducing the signal-to-noise ratio at $\sim 1 : 300$). On ground, the information from all LAT subsystems are examined in detail and several figures of merit are evaluated using automated data-mining techniques.

The final outcome of the on-ground event analysis is energy and direction for each event, with corresponding confidence levels, that the selected event describes a γ-ray and not a background particle. All the described ingredients are used to define standard event classes optimized for a range of scientific objectives and, at the same time, accounting for an obvious trade-off between efficiency, purity and resolution.

The main event classes defined prior to launch and used for the Pass8 dataset are the following:

- The *Transient* class, suitable for studying localized, intense, transient phenomena (e.g. GRBs), has the largest efficiency at the expense of a high residual background rate;
- The *Source* class, it is used for localizing sources with a residual background rate comparable to the extragalactic diffuse rate estimated from EGRET (Sreekumar et al. 1998).
- The *Diffuse* class, expected to achieve a background-rejection factor of the order of 10^6, while keeping an efficiency for γ-ray detection $\sim 80\%$. Its specific aim is the study of diffuse γ-ray emission

2.3 The LAT Instrument Response Function

In high-energy astrophysics, the instrument response functions (IRFs), conventionally represent a high-level model of the instrument response which enables the analysis of the data (IRFs; e.g. Davis (2001)). Canonically the detector response is factored into three terms: efficiency in terms of the effective area, resolutions as point spread function (PSF) and energy dispersion. The LAT IRFs were defined and parametrized prior to launch based on the MC simulations and beam calibration. The IRFs were subsequently updated to take into account effects measured in flight that were not considered in pre-launch performance estimates (Pass8).

2.3.1 IRF definition

The LAT performance is governed primarily by:

- LAT hardware design
- Event reconstruction algorithms
- Background selections and event quality selections

A result of the performance analysis is the production of full IRFs, describing the performance of the instrument as a function of photon energy, incidence angle, conversion point within the instrument, and other important parameters (see Figure 2.3 for the actual effective area and containment angle as a function of the energy of the reconstructed photons).

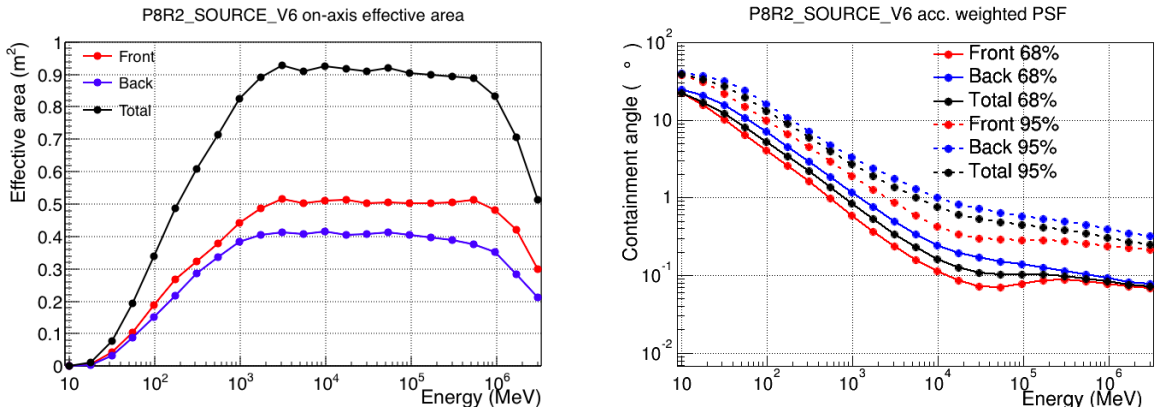

Figure 2.3: *Left: effective area as a function of photon energy for normal incidence photons ($\theta = 0°$). Right: 68% and 95% containment angles of the acceptance weighted PSF for front/back events. The plots are taken from http://www.slac.stanford.edu/exp/glast/groups/canda/lat_ Performance.htm.*

The IRF is the mapping between the incoming photon flux and the detected events. The "detection" depends not only on the LAT hardware but also on the processing that calculates the event parameters from the observable and assigns probabilities that an event is a photon.

Conventionally IRFs are defined as a function R of true photon energy E' and direction $\hat{p}'$, measured photon energy E and direction $\hat{p}$ and time t:

$$\frac{dN}{dtdEd\hat{p}}(E,\hat{p},t) = \int dE'd\hat{p}'R(E,\hat{p}|E',\hat{p}',t)\frac{dN}{dtdE'd\hat{p}'dS}(E,'\hat{p}',t)\,, \tag{2.1}$$

where the differential count rate $\frac{dN}{dtdEd\hat{p}}$ in the instrument phase space (reconstructed energy and direction) is given by the convolution of the source differential flux per unit area

at the detector with the IRFs. The IRFs are factorized into three functions, representing the efficiency, the angular resolution and the energy resolution plus a temporal scaling factor:

$$R(E, \hat{p}|E', \hat{p}', t) = T(t)A(E', \hat{p}')P(\hat{p}|E', \hat{p}')D(E|E', \hat{p}') \,, \tag{2.2}$$

where $T(t)$, the scaling factor, accounts for temporal variations, such as instrument failures, temporary switching off, thermal expansion or the deterioration of instrument components. The lack of consumables makes the LAT performance remarkably stable and therefore this term can be considered equal to 1. The three functions describing the IRFs are:

- the *effective area*, $A(E', \hat{p}')$, which is the detection efficiency for photons of true energy E' and arrival direction $\hat{p}'$ expressed as an area;
- the *PSF*, $P(\hat{p}|E', \hat{p}')$, it is the probability density that a photon with energy E' and arrival direction $\hat{p}'$ has a reconstructed direction $\hat{p}$;
- the *energy dispersion*, $D(E|E', \hat{p}')$, which is the probability density that a photon with energy E' and arrival direction $\hat{p}'$ has a reconstructed energy E.

The LAT IRFs are mainly determined by the hardware design, the event reconstruction algorithms and the event classification and selection. To evaluate the LAT response, a dedicated Monte Carlo simulation is performed. A large number of γ-ray events is simulated in order to cover all possible photon inclination angles and energies with good statistics. This is based on the best available representation of the physics interactions, the instrument, and the on-board and ground processing are used to produce event classes. The comparison between the properties of the simulated events within a given event class and the input photons give the IRFs.

Pass8

There are multiple IRFs delivered with the *Fermi* Science Tools to allow the user the flexibility necessary for the different analysis types. The current LAT data provided by the *Fermi* Science Support Center (FSSC)[1] have been processed using the Pass8 event-level analysis (Atwood et al. 2013). The Pass8 analysis uses an entirely new set of event-level reconstruction algorithms that improve the instrument performance and mitigate pile-up effects. All the results presented in the first part of this work are obtained with the Pass8 event-level analysis.

2.4 Data Analysis

The final results of the data reconstruction is the FT1 file. This is provided as a FITS (Flexible Image Transport System) file, a common file format used in astronomy. The data

[1] http://fermi.gsfc.nasa.gov/ssc/

are presented in a table with all the information about the events: each event is associated with an energy, a direction and some additional pre-computed quantities, as well as a flag which allows the user to select among the predefined event classes. To perform any analysis the information about the spacecraft, e.g., position along the orbit and the inclination, are needed. Those information are contained in the FT2 FITS file. LAT photon data are publicly available through the FSSC, together with the orbital history of the telescope.

The analysis of the data is done with the *Fermi gttools*[2], a set of tools based on the general package of the *ftools*[3], in order to have the maximum compatibility with the analysis of other astrophysics missions.

To use the photon file, the first operation is the selection of the data specifying the region of interest (ROI) of the sky, the time and the energy interval. The maximum zenith angle is also selected in order to avoid the contamination from the Earth albedo, caused by the γ-rays produced in the atmosphere from the interaction with cosmic rays. The second step is to extract data only from the so-called *Good Time Intervals* (GTIs), when the event is considered to be valid. This is done using the FT2 information about the pointing and the live-time history of the spacecraft.

Analysis for a specific Region or Source

The subsequent analysis needs to take into account the dependence of the photon direction to the IRFs. Therefore it is needed to estimate the *live-time cube* which is the exposure time for a given position at a given angle of observation with the LAT normal.

Subsequently it is preformed the calculation of the *exposure map* ε, which is the integration of the IRF over the entire ROI:

$$\varepsilon(E', \hat{p}') = \int_{ROI} dE d\hat{p} dt dR(E, \hat{p}|E', \hat{p}', t) \, . \tag{2.3}$$

Given the previous expression, the predicted number of photons from the source i is:

$$N_{pred} = \int dE' d\hat{p}' S_i(E', \hat{p}') \varepsilon(E', \hat{p}') \, , \tag{2.4}$$

where S_i is the photon intensity of the source i.

At this point, two methods are possible: a background-dependent analysis which is the standard approach in the γ-ray astronomy, or a background-independent method which makes use of wavelet functions in order to eliminate the background in the maps.

For the background dependent method, it is necessary to produce a model of the ROI, considering all known point-like sources in this region and the diffuse emission from the Galactic and isotropic components. The model is written in a XML file, that contains the

[2]http://fermi.gsfc.nasa.gov/ssc/data/analysis/scitools/overview.html
[3]http://fermi.gsfc.nasa.gov/docs/software/ftools/ftools_menu.html

best guess of the locations and spectral forms for the sources. Finally, it is possible to check how likely the model fits to the data using the *maximum likelihood estimation* approach, described in Mattox et al. (1996).

The method of the maximum likelihood estimation, as well the wavelet transform method, are described in the next chapter (respectively in Sections 3.1 and 3.3).

CHAPTER 3

Point source analysis with Wavelet Transforms

A very important goal of the γ-ray astronomy is the search and analysis of Galactic and extragalactic point sources. In this energy range three main features influence the analysis of the γ-ray data with respect to the observations in other wavelengths: the first aspect is the poor statistic. The second one is the difficulty of energy and direction reconstruction for each event, which implies a worse, if compared to other photon frequencies, angular resolution. The third feature is the large background emission contained in the data. As a consequence of these three features it is really important to have an accurate source analysis which search and extract all the information of the γ-ray sources. In general two possible approaches are used in γ-ray source analysis:

- background-dependent methods (e.g., the likelihood method), which require the modeling of the diffuse background,
- background-independent methods (e.g., the wavelet transform method).

The two methods for the γ-ray source analysis are discussed in this chapter. Section 3.1 presents the likelihood analysis. Section 3.2 describes the difficulties of the creation of an accurate diffuse-emission model, which is needed in the likelihood analysis. The wavelet transform method is discussed in Section 3.3. Section 3.4 presents the results of the verification of the wavelet transform method, with the use of the PGWave tool, on MC simulated data between 1 and 10 GeV. The content of the last section (Section 3.4) is taken from the proceeding Principe & Malyshev (2017) presented at the *Gamma 16* conference[1].

[1]Gamma 2016 - 6th Heidelberg International Symposium on High-Energy Gamma-Ray Astronomy, Heidelberg, 11-15 July 2016

3.1 The likelihood analysis

During its lifetime the LAT has collected hundreds of millions of photons (counts) but, considering only a specific region or source, a subset of only a few thousand events are used. The numbers of photons per pixel are too small in many cases to allow the use of χ^2 as test statistic. Therefore a Poisson likelihood optimization is needed to estimate the model parameters of the GeV sky.

The application of the likelihood method to photon-counting experiments is done in the analysis of *Fermi*-LAT data, because it is difficult to isolate a γ-ray source from the diffuse emission. This is mainly due to the limited statistics, the dependence of angular resolution on energy, as well as the strong and structured diffuse emission of the Galactic and isotropic components, which are not known well enough.

The technique requires to develop a model for the signal detected by the telescope. The input model is the distribution of the γ-ray sources in the sky, including their intensity and spectra. The likelihood is used to estimate to what extent observed data are consistent with a statistical hypothesis and to find the best fit model parameters. These parameters are, e.g. the description of the source's spectrum and its position.

The likelihood $\mathcal{L}$ represents the probability to obtain the data given a model. Assuming that the model has m free parameters $\alpha_{k=1\ldots m}$, the expected observed distribution of count hits is given by:

$$M(E,\hat{p},\{\alpha_k\}) = \int dt dE' d\hat{p}' R(E,\hat{p} \mid E',\hat{p}',t) S(E',\hat{p}',t,\{\alpha_k\}) \,, \tag{3.1}$$

where S is the differential flux of the model $S = d\phi/dE' = dN/(dtdE'dA)$, A is the effective area, and therefore $M = dN/dt$.

The counts expected in a given energy range (E_1, E_2), solid angle Ω and time interval (t_1, t_2) are obtained as the integral of the differential count rate in the detector:

$$\Lambda(\{\alpha_k\}) = \int_{t_1}^{t_2} dt \int_{\Omega} d\hat{p} \int_{E_1}^{E_2} dE dM(E,\hat{p},\{\alpha_k\}) \,. \tag{3.2}$$

In the best case, which however requires powerful computing facilities, it is possible to bin events in energy E, direction $\hat{p}$ and arrival time t in such a way that each bin contains only one single photon (unbinned analysis). If the time binning width is Δt, in each bin the expected number of photons can be calculated by:

$$N_{exp}(E,\hat{p},t,\{\alpha_k\}) = M(E,\hat{p},t,\{\alpha_k\}) \cdot \Delta t \,. \tag{3.3}$$

Indicating with P the set of bins containing one photon and Q the set of bins containing no photons, it is assumed that the probability of observing a photon follows the Poisson distribution:

$$f(n,\nu) = \frac{\nu^n}{n!} e^{-\nu} \tag{3.4}$$

therefore the likelihood function associated with the parameters set $\{\alpha_k\}$ is defined as

$$\begin{aligned} \mathcal{L}(\{\alpha_k\}) = \prod_P N_{exp}(\{\alpha_k\}) e^{-N_{\rm exp}(\{\alpha_k\})} \prod_Q e^{-N_{\rm exp}(\{\alpha_k\})} = \\ \prod_P N_{\rm exp}(\{\alpha_k\}) \prod_{P\cup Q} e^{-N_{\rm exp}(\{\alpha_k\})} \,. \end{aligned} \tag{3.5}$$

The likelihood is defined as the product for each pixel of the probability densities of observing $N_{\rm obs}$ counts given the expectation $N_{\rm exp}$. Given that the probabilities are represented by extremely small numbers, it is convenient to use the logarithm of the likelihood. In addition, the logarithm changes products to sums, easing the computation:

$$\begin{aligned} \ln \mathcal{L}(\{\alpha_k\}) &= \sum_P \ln N_{\rm exp}(\{\alpha_k\}) - \sum_{P\cap Q} N_{\rm exp}(\{\alpha_k\}) \\ &= \sum_P \ln M(\{\alpha_k\}) + \ln \Delta t^{N_{\rm obs}} - N_{\rm tot}(\{\alpha_k\}) \,, \end{aligned} \tag{3.6}$$

where $N_{\rm obs}$ is the number of observed photons and $N_{tot}(\{\alpha_k\})$ is the total number of photons expected from the model $S(\{\alpha_k\})$. To find the set of parameters that maximizes the likelihood $\mathcal{L}$, or $\ln \mathcal{L}$, it is possible to omit the constant term $ln\Delta t^{N_{\rm tobs}}$.

The maximum of the likelihood $\mathcal{L}$ corresponds to the minimum of -ln $\mathcal{L}$. The most probable set of parameters $\{\alpha_k\}$ are obtained by minimizing -ln $\mathcal{L}$.

In the case of limited statistics, an *unbinned likelihood* method can be used. Assuming a grid fine enough that in each pixel the number of observed counts is either 0 or 1. The logarithm of the likelihood is therefore simply:

$$\ln \mathcal{L}(\{\alpha_k\}) = \sum_{i\in P} \ln \Lambda_i(\{\alpha_k\}) - \Lambda_{\rm tot}(\{\alpha_k\}) \,. \tag{3.7}$$

In a small enough pixel $\Lambda_i(\{\alpha_k\}) = M(E_i, \hat{p}_i; \{\alpha_k\})\Delta t \Delta\hat{p} \Delta E$ so Eq. 3.1 yields:

$$\begin{aligned} \ln \mathcal{L}(\{\alpha_k\}) &= \sum_{i\in P} [\ln M(E_i, \hat{p}_i; \{\alpha_k\}) + \ln \Delta t + \ln \Delta\hat{p} + \ln \Delta E] - \Lambda_{\rm tot}(\{\alpha_k\}) \\ &= \sum_{i\in P} [\ln M(E_i, \hat{p}_i; \{\alpha_k\}) + \ln \Delta t^{N_{obs}} + \ln \Delta\hat{p}^{N_{obs}} + \ln \Delta E^{N_{obs}}] - \Lambda_{\rm tot}(\{\alpha_k\}) \,, \end{aligned} \tag{3.8}$$

where N_{obs} is the total number of observed photons. Since the mid terms are independent from the model, they can be neglected for the likelihood maximization and Eq. 3.1 becomes:

$$\ln \mathcal{L}(\{\alpha_k\}) = \sum_{i \in P} [\ln M(E_i, \hat{p}_i; \{\alpha_k\}) - \Lambda_{\rm tot}(\{\alpha_k\}) \,, \tag{3.9}$$

where the first summation can be practically computed looping over the energies and directions of the observed photons.

The likelihood method can also be used to compare two different models. In fact, the hypothesis $\mathcal{H}$ of having a model $\mathcal{M}$ with m free parameters, described by $\mathcal{L}$, and the hypothesis $\mathcal{H}_0$ of having a model $\mathcal{M}_0$ with $h < m$ free parameters, described by $\mathcal{L}_0$, can be compared using the *Test Statistic* (TS) defined as

$$TS = 2 \ln \left(\frac{\mathcal{L}_{max}}{\mathcal{L}_{0,max}} \right) \,. \tag{3.10}$$

In the limit of a great number of counts, if the models are *nested*[2], according with the Wilks' theorem, the TS is distributed as a χ^2 with $(m - h)$ degrees of freedom.

In particular, the TS is the key to measure a significance of a source. If $\mathcal{L}$ is the likelihood of a model that includes the presence of a particular source and $\mathcal{L}_0$ is the likelihood of the model without this object, the TS is distributed as a χ^2 with n degrees of freedom, where n is the number of free parameters that characterizes the source.

In Chapter 6, the maximum likelihood method is used in the analysis of the PWN HESS J1825-137.

3.2 Development and caveats of the LAT diffuse emission model

As presented in the previous section, the maximum likelihood method needs a model of the background diffuse emission in order to extract from the data the source best-fit parameters. This section presents the procedure to develop a model for the diffuse emission as well as the difficulties encountered in such a procedure. The latest model of the diffuse emission created by the LAT collaboration is also described here as an example of the construction of a diffuse model.

The model for interstellar γ-ray emission is based on a linear combination of templates for interstellar gas column density and for the inverse Compton emission. The interactions of energetic cosmic rays (CRs) with gas and photons produce the high-energy γ-ray emission. In particular, the main contributors to the Galactic diffuse emission are the decay of secondary particles produced in hadron collisions, the inverse Compton scattering of the electron in the interstellar radiation field (ISRF) and their bremsstrahlung radiation emission in the interstellar medium (ISM).

[2]With this notation, $\mathcal{M}_0$ can be obtained by fixing $(m - h)$ parameters of $\mathcal{M}$

The diffuse γ-ray intensity, at any energy, is modeled as a convolution of gas and CR with the gamma-ray production cross-section. The convolution is made using templates of hydrogen column-density (I_H) and a predicted inverse Compton (IC_p) intensity map (I_{IC_p}) calculated by GALPROP[3] (Orlando et al. 2017). Hydrogen is the main component of the ISM (70%) and since it exists in atomic, molecular, and ionized forms, the H_1 could be traced by its radio 21-cm line radiation. The H_2 component could be traced by other molecules, especially by the 2.6-mm (J=1→0) line of carbon 12 monoxide (CO). Since the CO is not a perfect tracer of H_2, it leads to large underestimates of the quantities of gas called dark neutral medium (DNM) in our Galaxy (Grenier I.A. 2005). Whereas different gas column-density maps provide templates for photons originating mainly from π_0 decay and Bremsstrahlung emission, a direct observational template for the IC emission does not exist. Predictions from GALPROP, or other simulation tools for the γ-ray diffuse emission, are usually used.

In addition to the interstellar emission, the LAT detects γ rays from other sources, which need to be taken into account in the analysis (see Figure 3.1). This is done by adding dedicated components to account for:

- a residual intensity of the Earth limb (I_{limb}): CR protons and electrons interacting with the Earth limb make the Earth a γ-ray source in the sky (Abdo A. A. 2009);
- point and extended γ-ray sources (I_{ext}): a template for interstellar diffuse emission as well as templates for the extended sources and point sources are included in the model;
- emission from the Sun and the Moon ($I_{sun-moon}$);
- uniform intensity template (I_{iso}) to account for unresolved γ-ray sources and CR contamination in the data.

Excesses coming from Loop I or the *Fermi* bubbles are observed when the *Fermi*-LAT observations are compared to a preliminary template model derived by the π_0 decay, Bremsstrahlung emission and IC emission. For the γ-ray emission from those large structures there are no templates from other observation. Only the Loop I could be roughly modeled by using radio observation. If Loop I and *Fermi* bubble are not included in the template, then there are large residuals. The template for the Fermi bubbles is directly obtained from the γ-ray data itself. Figure 3.2 shows the positive residuals after the subtraction to *Fermi*-LAT counts map of the model template, which contains point and extended sources, the limb and isotropic emission, and a conventional interstellar model based on a fitted gas emissivities and scaled IC_p.

A particular difficult region to model is the inner Galactic region. In this region the gas column densities are affected by optical depth correction, self-absorption of H_1 and

[3]http://galprop.stanford.edu

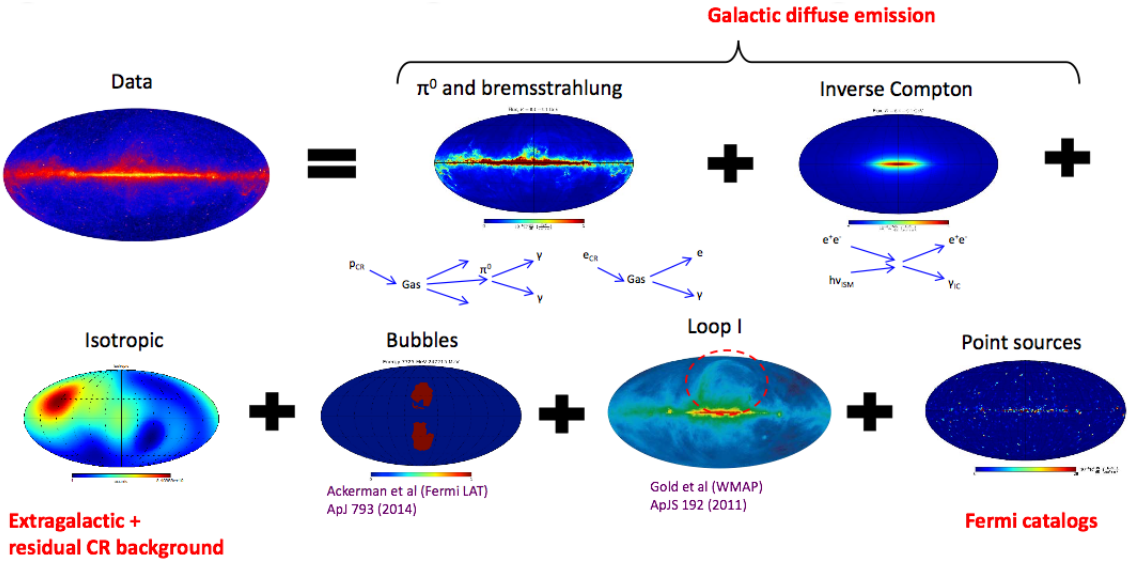

Figure 3.1: *Description of the Fermi-LAT data with the separated components that contribute to the γ-ray sky.*

limited kinematic distance resolution at low longitudes. Additionally there are also numerous unresolved γ-ray point and extended sources as well as large uncertainty in the IC morphology.

3.3 The wavelet transform method

The wavelet transform (WT) method is a background independent method for the source search and analysis. It does not require any diffuse-emission model, as the likelihood method does. Difficulties and uncertainties in the creation of interstellar diffuse-emission model, can be avoided if one uses a background independent method in order to not be strongly affected by the lack of knowledge of the diffuse emission.

The WT is in general a multiscale transform providing a representation of the data that allows an easy extraction of the source features in an image. This is a method well suited to detect sources in astronomical images. In particular it was developed for photon-counting detectors, such as X-ray and γ-ray images, where the information for most sources need to be extracted from a handful of photons, and the photon statistics per image pixel is significantly different from a Gaussian. For an introduction to WTs see Daubechies (1992).

Various kinds of WTs exist, depending on what data properties are being investigated. The WT are represented as a convolution with a wavelet kernel. The kernel is characterized, e.g., by the center position and scale - in case of the Mexican hat kernel. The WT of a

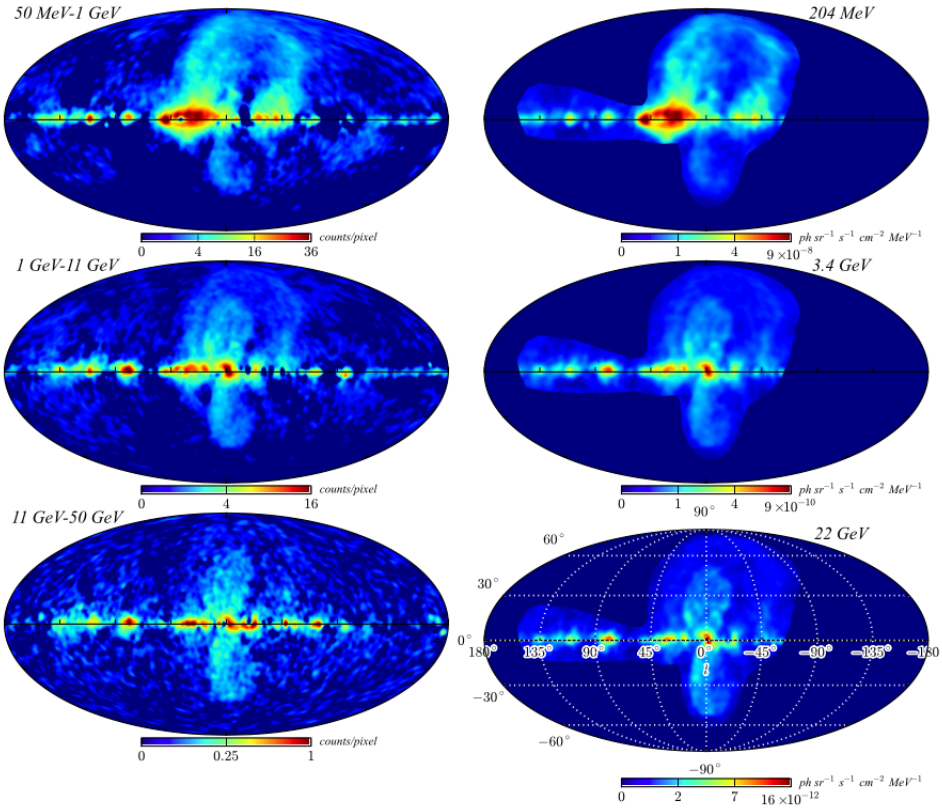

Figure 3.2: *Left column: Mollweide projection in Galactic coordinates of the Fermi-LAT counts map after subtracting point and extended sources, the limb and isotropic emission, a conventional interstellar model based on fitted gas emissivities and scaled IC_p only. The residual map is shown for three energy bands: 50 MeV– 360 GeV (top), 1–11 GeV (middle), 11–50 GeV (bottom). Right: intensity of the modeled large scale emission structures at energies: 204 MeV (top), 3.4 GeV (middle), 22 GeV (bottom). All the maps are displayed with a square root scaling and a pixel size of 0.25°. The plots are taken from Acero et al. (2016).*

2-dim image $f(x, y)$ is defined as:

$$w(x, y, a) = \iint g\left(\frac{x - x'}{a}, \frac{y - y'}{a}\right) f(x', y')dx'dy' \ , \tag{3.11}$$

where $g(x/a, y/a)$ is the generating wavelet, x and y are the pixel coordinates, and a is the scale parameter. In the method presented in Damiani et al. (1997), as well in the PGWave tool, used in this work, the 2-dim "Mexican Hat" wavelet is used (Figure 3.3):

$$g\left(\frac{x}{a}, \frac{y}{a}\right) = g\left(\frac{r}{a}\right) = \left(2 - \frac{r^2}{a^2}\right) e^{-r^2/2a^2} \ (r^2 = x^2 + y^2) \ . \tag{3.12}$$

The kernel g ensures that the WT of a function $f(x, y) = c_1 + c_2x + c_3y$ (a tilted plane) is zero. Therefore, the WT will be zero for both a constant or uniform gradient local

background. While the WT is not sensitive to gradients in the data with this choice of g, it is sensitive to second derivatives of $f(x, y)$, e.g. local maximum or minimum, making it suitable for detecting sources in an image.

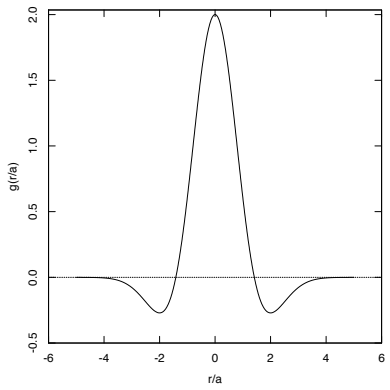

Figure 3.3: *Mexican hat generating wavelet $g(r/a)$.*

The peak of the WT for a source with Gaussian shape (N_{src} total counts and width σ_{src}) is (Damiani et al. 1997):

$$w_{peak}(a) = \frac{2N_{src}}{(1 + \sigma_{src}^2/a^2)^2} \ . \tag{3.13}$$

Such relation implies a linear correlation between the WT peak and the total number of photons from a source.

3.3.1 Source detection and localization

After selecting the scale parameter a, one performes a WT transform and searches for the local maxima in the WT map as positions of possible PS (PS seeds). A peak is retained as a positive detection if its amplitude is significant with respect to the expected fluctuations of the local background, at a given confidence level $n\sigma$. The value of n is chosen to minimize the number of spurious detections while retaining good detection efficiency for real sources, and it has to be tuned using extensive simulations for the particular detector under consideration.

For the localization of the source, the position of the PS can be approximated by the center of the pixel corresponding to the WT maximum. In several applications, the WT is then recomputed in a small neighborhood of each source over a final grid of spatial positions, to derive the source position more accurately. Alternatively, a parabolic fit among the neighborhood pixel of each source could also improve the localization of the source.

3.3.2 Source count rate

In order to determine the count rate and size of a Gaussian source, it is possible to make use of the function $y(a) = w(a)/a$ introduced in Section 3.3, which is equal to

$$y(a) = \frac{1}{a} \frac{2I_{src}}{[1 + (\sigma_{src}^2/a^2)]^2} \ . \tag{3.14}$$

where the $y(a)$ is proportional to the source intensity (count rate) I_{src} and σ_{src}. In Section 3.4.2, a method used for the determination of the source flux using the peak of the WT is described.

3.3.3 PGWave: a Wavelet Transform Method

PGWave is a tool, based on WTs that can be used to find PS without the need of a background model. Figure 3.4 shows an example of the use of the WT on a counts map containing point sources, Galactic and extragalactic diffuse emission. PGWave directly eliminates all the flat and gradient backgrounds returning the peaks in the map. The wavelet transformed map shows that PGWave is able to eliminate the diffuse emission and to return all the peaks present in the input map.

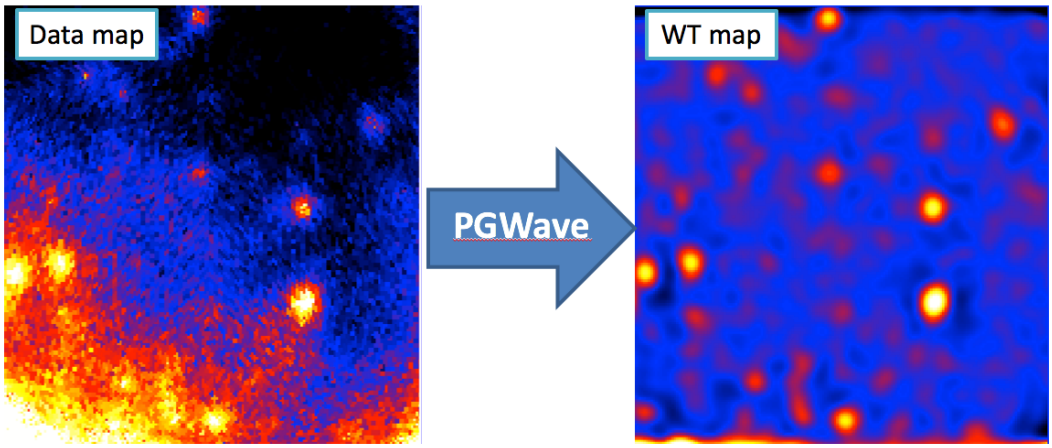

Figure 3.4: *An example of the application of the PGWave tool. Left: simulated data containing point sources and Galactic and extragalactic diffuse emission. Right: Wavelet transformed map. The WT method eliminates all the flat and gradient backgrounds and returns the peaks due to the point sources.*

3.4 PGwave test on simulated *Fermi*-LAT data between 1 and 10 GeV

A study of PGWave on simulated *Fermi*-LAT data has been recently published in Principe et al. (2018b) and therefore this section follows it closely and in large parts in verbatim.

3.4.1 Monte Carlo data

The data used to study PGWave were created using MC simulation of the sky in the energy range from 1 GeV to 10 GeV. The MC simulations were performed with *gtobssim*, a Fermi tool used to simulate point sources and diffuse emission for Fermi observations, with a specific spectral shape, for a selected region of the sky.

The simulation includes:

- galactic diffuse emission,
- isotropic background,
- PS.

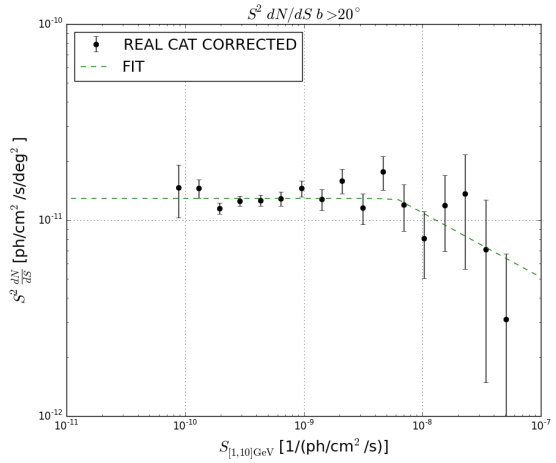

Figure 3.5: *dN/dS distribution of 3FGL PS. The green dashed line is the input PS distribution in the Monte Carlo simulation. The plot is taken from Principe & Malyshev (2017)*

The fluxes of the simulated sources follow the $LogN - LogS$ function given by the green dashed line in Figure 3.5, which was derived from the 3FGL catalog (Acero et al. 2015). The spectral energy distribution of the sources is a Power law with spectral index randomly chosen from Gaussian distribution with $\mu = 2.30$ and $\sigma = 0.40$ motivated by the distribution of extra-galactic sources in the 3FGL catalog.

Energy range	1 GeV - 10 GeV
Interval of time	92 months
IRF	P8R2_SOURCE_V6

Table 3.1: *Parameters used to create the MC data.*

The main parameters used to create the MC data are summarized in Table 3.1.

Figure 3.6 shows the counts map of the MC data obtained with the selection described above.

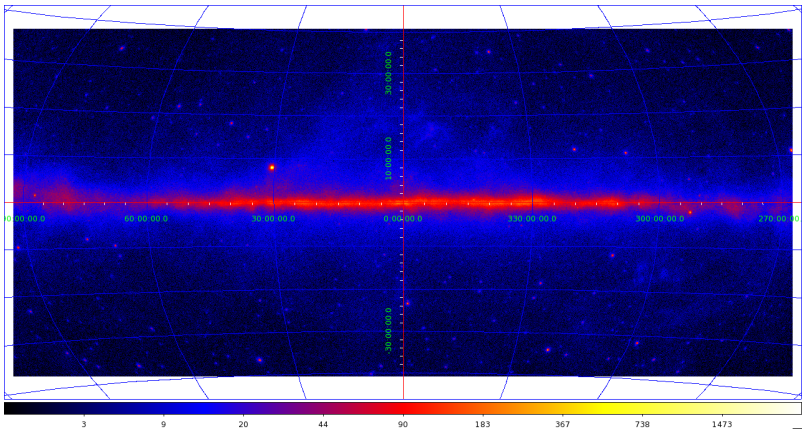

Figure 3.6: *Counts map of the MC data in the region of the sky:* $-90° < LON < 90°$, $-40° < LAT < 40°$. *The plot is taken from Principe & Malyshev (2017)*

3.4.2 PGWave: Analysis

PGWave, as described before, is a WT method that works on count maps. The MC data were passed as input to PGWave, which then returns a list of PS candidates that contains, in particular, position, significance and WT peak values.

For the analysis with PGWave some selections to the data were applied:

1. the analysis was restricted to the area: $-90° < LON < 90°$, $-40° < LAT < 40°$,
2. the Galactic Plane ($-5° < LAT < 5°$) was masked,
3. only MC sources with a Flux $> 10^{-10}$ph cm^{-2}s^{-1} were selected.

The parameters used for PGWave analysis are summarized in Table 3.2.

Pixel dimension	0.1°
MH Wavelet Transform scale	0.3°
Statistical confidence	3 σ
Minimum number of connected pixels	5

Table 3.2: *Parameters used in the PGWave analysis.*

PGWave: Point Source Detection

The PGWave results were compared to the input MC data using a method that associates the PGWave seeds with the input sources. The algorithm for the association is based on a positional coincidence, with a tolerance radius of 0.56° (similar to the PSF at 2 GeV), and on a flux ordering. The flux ordering algorithm associates seeds with a large WT peak value with bright MC input sources, this allows a better association in particular in the cases where inside the tolerance radius more than one source are present.

In the MC data there are 1230 sources, with a flux above $> 10^{-10}$ph cm^{-2}s^{-1}. PGWave found 808 seeds, of which 720 are associated with MC sources using a tolerance radius of 0.56°. Figure 3.7 shows the counts of the MC data containing both the simulated sources and the PGWave seeds for a comparison.

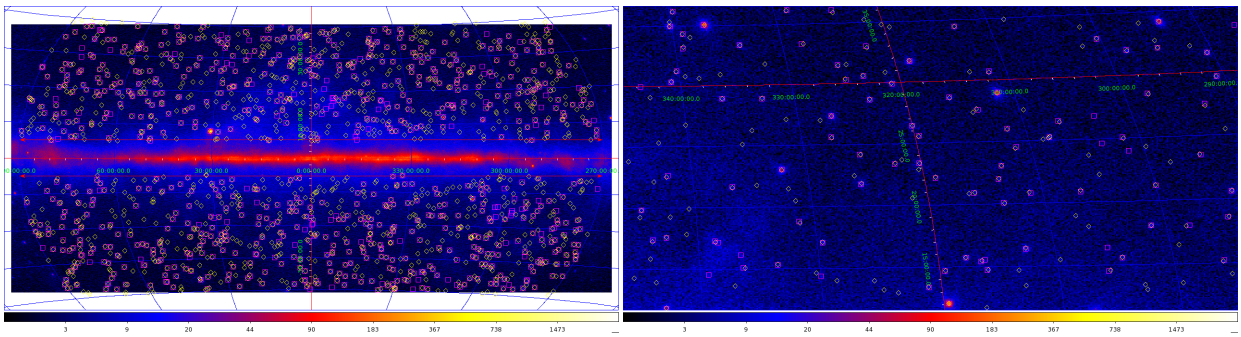

Figure 3.7: *Counts maps of the MC data with simulated sources, represented here with yellow diamonds, and PGWave seeds, represented with magenta diamonds. Left: counts map of all the region. Right: zoom in the region of the dimensions of* 40×60 *degrees centered in the position of LAT*$= 25°$ *and LON*$= 320°$*. The plots are taken from Principe & Malyshev (2017).*

PGWave: Flux Determination

The WT peak value was used for the estimation of the flux of the associated PS, because a linear correlation between them is expected (Equation 3.14). Figure 3.8 (left) shows the plot of the MC input flux vs the WT peak value of the associated PS. A linear correlations is observed. This allows the possibility to derive the flux of the sources using a fit and the WT peak values provided by PGWave. To determine the best fit, the associated PS with MC Counts >100 were selected.

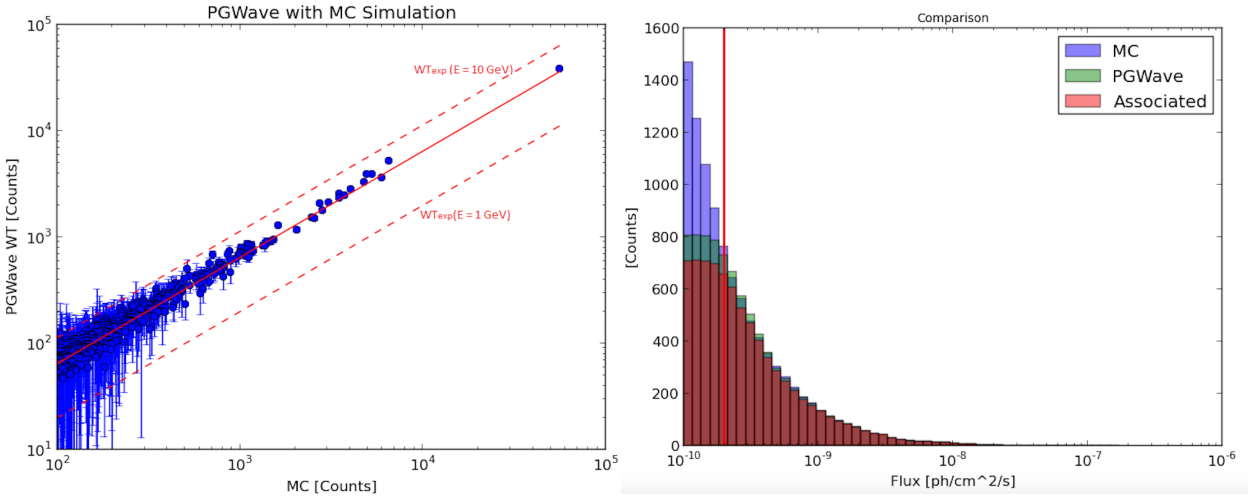

Figure 3.8: *Left: plot of the associated PS. X-axis: MC input counts, y-axis: the WT peak value from PGWave. The red line represents the best fit. The two dashed lines are the expected values of the WT peak for the energy of 1 GeV and 10 GeV. Right: inverse cumulative distribution of the associated PS with the estimated flux. The red line represents the cut applied for the best fit. The plots are taken from Principe & Malyshev (2017)*

The statistical uncertainty on the WT peak value was estimated by the total number of photons inside the circle with wavelet scale radius. The bracketing values were derived using the PSF at 1 GeV and at 10 GeV for the P8R2_SOURCE_V6 data in the WT peak (Equation 3.14). All reconstructed PS fluxes fall within the bracketing values.

One can see from Figure 4.3.7 (right) that PGWave finds more than 85% of the MC sources above 2×10^{-10}ph cm^{-2}s^{-1}.

3.4.3 Conclusion on the PGWave test on MC data

In this work the PGWave tool was applied to MC simulated data, in the presence of diffuse emission background.

1. It was confirmed that PS detection works well at $\mid LAT \mid > 5°$.
2. There is a very good correlation between the WT peak and the input MC flux which makes the WT a very promising method to find a background independent estimate of the PS flux.

In the future, PGWave could be useful for detecting PS and estimating their flux without the need of a background model.

CHAPTER 4

Motivation and analysis description of the 1FLE catalog

All the previous point source analysis have been performed either below 30 MeV or above 100 MeV. Since *Fermi*-LAT observations starts at 20 MeV, it is possible to create, for the first time, a catalog of γ-ray sources in the energy range between 30 and 100 MeV (the 1FLE catalog).

This chapter illustrates the motivation for having a new *Fermi*-LAT catalog below 100 MeV and the description of the point source analysis performed in this work. Section 4.1 presents a motivation for the catalog, the reason for the absence of a catalog in this energy range, and a short description of the analysis performed in this work. The Monte Carlo simulations used to optimize the point source analysis are described in Section 4.2. Section 4.3 contains the description of the point source analysis and its optimization. Particular attention was given to the selection of the event type for the input data and to the optimization of the PGWave analysis' parameters. The last section describes also the methods used for the source localization and flux determination as well as the estimation of their uncertainty.

Parts of this work were published in proceedings, Principe et al. (2018c) and Principe et al. (2018a), and in an article (Principe et al. 2018b). Therefore the next sections are following them closely and in large parts in verbatim.

4.1 Motivation for the 1FLE catalog

The Large Area Telescope (LAT, Atwood et al. 2009) on board the *Fermi Gamma-ray Space Telescope* has revolutionized our understanding of the high-energy sky. The LAT detects γ-rays in the energy range from 20 MeV to more than 300 GeV, measuring their arrival times, energies, and directions.

Although the LAT observations start at 20 MeV, all previous catalogs released by the *Fermi*-LAT Collaboration were produced using optimized analysis focused on energies larger than 100 MeV. In particular, the third *Fermi*-LAT catalog (3FGL, Acero et al. 2015) characterizes 3033 sources in the energy range between 100 MeV and 300 GeV from the first four years of LAT data.

The EGRET telescope (Hartman et al. 1992), which is a preceding γ-ray experiment, measured γ-rays from 20 MeV to 30 GeV. However, the catalogs released by the EGRET collaboration only used data above 100 MeV (e.g., Hartman et al. 1999). At lower energies, COMPTEL analyzed the γ-ray sky between 0.75 and 30 MeV (Schönfelder et al. 2000). Figure 4.1 shows the number of sources, energy range and number of years used for the analysis of the previous catalogs of γ-ray sources: the first COMPTEL catalog, between 0.75 and 30 MeV, the third EGRET catalog between 100 MeV and 10 GeV and the FGL (1FGL, 2FGL, and 3FGL) catalogs between 100 MeV and 100 or 300 GeV.

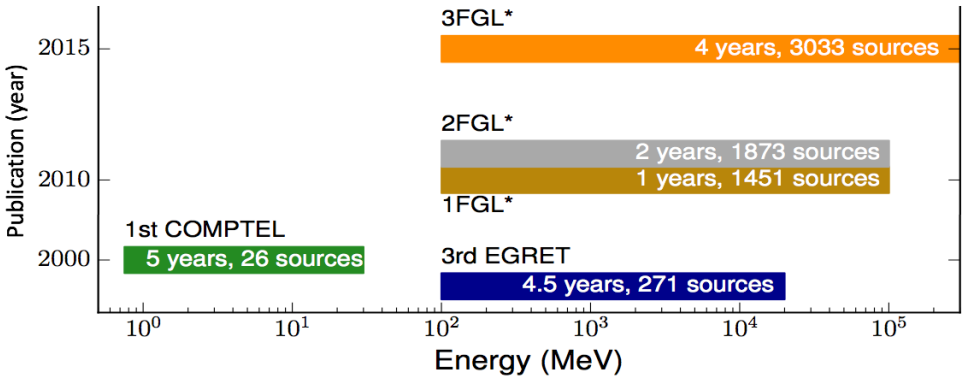

Figure 4.1: *The plot show the energy range used, the number of sources found and the number of years of data used for the analysis of the previous γ-rays catalogs.*

Therefore, the energy range from 30 MeV to 100 MeV was not covered yet by any of the previous γ-ray point source (PS) analyses.

4.1.1 Missing MeV sources

The *Fermi* LAT has discovered over 200 γ-ray pulsars in the nearly ten years since its launch (Acero et al. 2015). This population of Galactic objects includes both young and very energetic pulsars, middle-aged pulsars and old, recycled millisecond pulsars. Most of them have the spectral energy distributions (SEDs) which peak at several GeV.

There exists another group of very energetic, young rotation-powered pulsars with non-thermal hard X-ray emission peaking in the MeV band, but without detected emission by *Fermi* LAT above 100 MeV (Harding & Kalapotharakos 2017).

Kuiper & Hermsen (2015) reported a list of very young energetic pulsars, which are mostly not detected by *Fermi* LAT because they reach their maximum luminosity in the

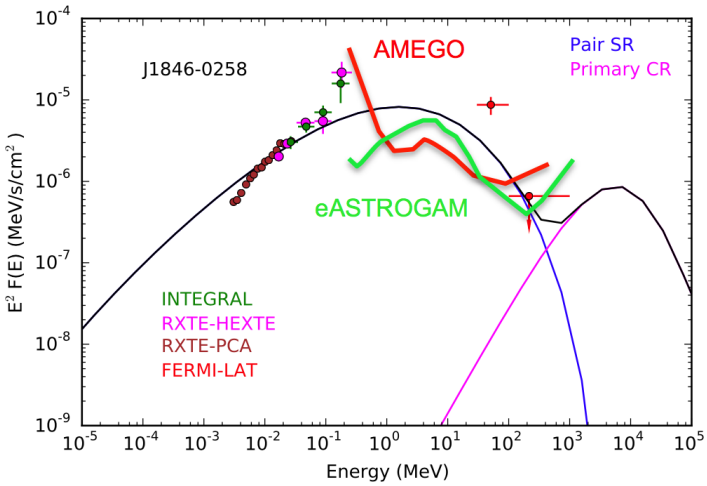

Figure 4.2: *Spectral energy distribution for PSR J1846-0258 and data from X-ray instruments (Kuiper & Hermsen 2015), compared to the one-year sensitivity of AMEGO (McEnery 2017) and e-ASTROGAM (De Angelis et al. 2017b). This pulsar is a promising candidate to be detected in the 30–100 MeV band with Fermi LAT. The plot is taken from Harding & Kalapotharakos (2017).*

MeV band and become too weak for detection above 100 MeV. All high-energy emission models propose contributions to the non-thermal pulsar spectrum of synchrotron radiation produced deep in the magnetosphere, reaching its maximum luminosity at MeV energies, and of higher-energy curvature radiation and inverse Compton radiation produced higher-up in the magnetosphere, closer to the light cylinder. These curvature and inverse Compton components appear to be too weak for detection by *Fermi* LAT above 100 MeV.

Figure 4.2 shows the extrapolated spectra of a soft source: the PSR J1846-0258. It is a young 0.72 kyr old pulsar with soft γ-ray spectrum and X-ray photon index E^{γ} equal to -1.72 (Kuiper & Hermsen 2015). This pulsar is a promising candidate to be detected in the 30–100 MeV band with *Fermi* LAT.

4.1.2 Reason for the absence of catalogs in the 30-100 MeV band

The energy range between 30 and 100 MeV is a very challenging range to perform a point source analysis for the following three reasons:

1. *The angular resolution is much worse at low energies relative to high energies.*. The resolution of the photon direction depends strongly on the energy of the incoming photons. The LAT makes use of the pair production effect to reconstruct the direction, in the tracker. The energy is reconstructed in the calorimeter from the shower of the secondary particles of the electro-magnetic shower. The problem is that the e^+ and e^-, due to their small energy, are more affected by interactions with the nuclei in the tracker (the so-called multiple scattering), which affects the determination of

the direction. Figure 4.3 shows the LAT containment angle (angular resolution) as a function of the energy, in particular below 100 MeV the PSF is larger than 5°.

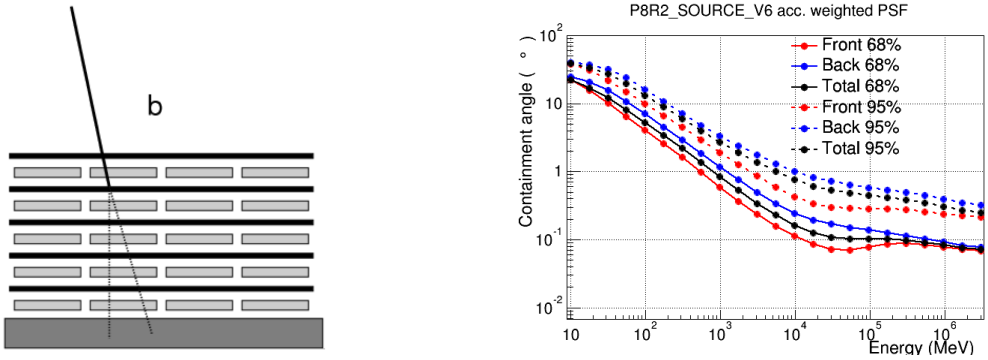

Figure 4.3: *Left: schematic representation of a photon detection in the LAT instrument. It shows the photon that interacts with the layers in the tracker and the calorimeter. Right: LAT 68% and 95% containment angles of the acceptance weighted (acc. weighted) PSF for both the front/back event types. The plot on the left is taken from the nuclear-physics lectures given in spring 2017 at the University of Minnesota https://sites.google.com/a/umn.edu/mxp/student-projects/2017_spring/s17_pairproduction, instead the plot on the right is taken from http://www.slac.stanford.edu/exp/glast/groups/canda/lat_Performance.*

2. *The effective area gets smaller.* Since, at low energy, a not negligible amount of γ rays interact with the matter through compton effect, part of the incoming photons are then missed by the LAT. Furthermore the LAT was developed and optimized to observe photons at higher energies. The maximum of the effective area is therefore obtained in the energy range between 1 GeV and several hundred GeV. Figure 4.4 shows the LAT effective area as a function of the energy of the incoming photons. A plot of the attenuation of the compton and pair production effects is also shown in order to better compare at which energy the pair production mechanism starts to dominate.

3. *The difficulty in creating an accurate model for the diffuse emission.* As it was described in Section 3.2, the creation of an accurate model for the diffuse emission is a very challenging task. In particular at low energy the Galactic diffuse emission is very bright and it is extended to high latitude ($\mid b \mid \sim 40°$). In addition no diffuse models have been created below 50 MeV yet, due to the difficulty in correctly describing the components of the γ-ray sky.

4.1.3 Innovation and advantages of this new PS analysis

At energies below 100 MeV, the analysis of point sources is complicated due to large uncertainties in the arrival directions of the γ rays, which leads to confusion among point

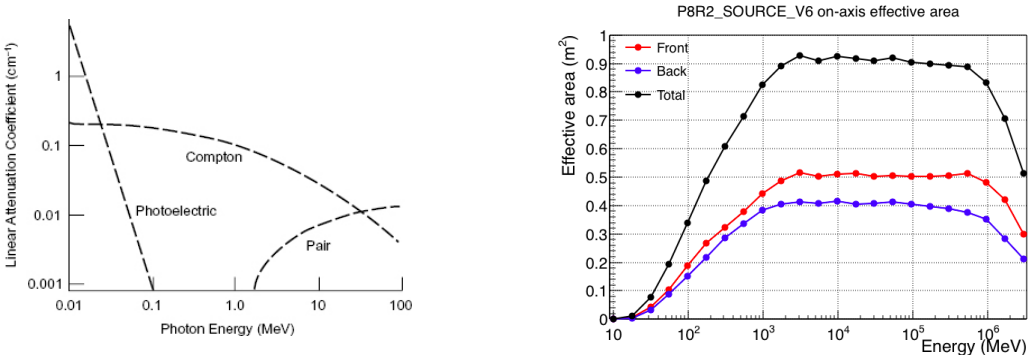

Figure 4.4: *Left: Attenuation of the photoelectric, compton and pair production effect varying the energy of the incoming photon. Right: LAT effective area as a function of the energy in case of normal incidence photons ($\theta = 0°$). The plots are taken from http://www.slac.stanford.edu/exp/glast/groups/canda/lat_ Performance.html.*

sources, difficulties in separating point sources from diffuse emission, and high contamination from the Earth limb. In order to reduce the dependence on unknown components, this work makes use of a background-independent analysis of point sources based on a wavelet transform of the γ-ray data, which filters out the large-scale diffuse emission and the Earth limb contamination. In particular, the wavelet transform method implemented in the PGWave tool (Damiani et al. 1997) is used. PGWave is already used in the *Fermi*-LAT catalog pipeline as one of the methods to find PS candidates (so-called seeds). In the standard catalog pipeline (e.g., for the 3FGL), the PS candidates are further evaluated with a likelihood analysis to refine the positions of the sources and to determine the fluxes. In contrast, in this work, the wavelet transform is used both to detect the sources and to estimate their fluxes (see, e.g., Principe & Malyshev 2016, for a discussion of the flux determination with the wavelet transformation).

Furthermore the analysis takes full advantage of the improvements provided by the Pass 8 data selection and event-level analysis (Atwood et al. 2013), especially the large increase of acceptance at low energy (>70% below 100 MeV) and the point-spread-function (PSF) event type classification[1]. Special attention is given also to the different PSF event type selections, in particular to the data cuts used to maximize the detection rate in the point-source analysis.

4.2 Description of Monte Carlo simulation

The large PSF below 100 MeV implies that the number of independent positions in the sky, namely the positions that are possible to spatially distinguish with the given resolution, is not very large. Therefore, it is necessary to perform an accurate study on the choice of

[1] A measure of the quality of the direction reconstruction is used to assign events to four quartiles

the event selection (PSF event types) and on the parameters of the point-source analysis (PGWave parameter) in order to optimize the detection and minimize the number of false positives. Monte Carlo (MC) simulations were used to test and optimize the parameters of the analysis.

The simulations have two steps: choice of the diffuse model and choice of the positions and fluxes of point sources. For the diffuse model, the γ-ray data were fitted with a combination of templates that trace different components of emission, such as hadronic interactions of cosmic rays with interstellar gas, inverse Compton (IC) scattering, *Fermi* bubbles etc. The construction of the diffuse model follows the same steps as the Sample model in Ackermann et al. (2017a). In particular, the diffuse model has the following templates: π^0 + bremsstrahlung in 5 Galactocentric rings, 3 IC components corresponding to IR, starlight and CMB radiation fields, *Fermi* bubbles at $|b| > 10^{\circ}$, geometric Loop I template, Sun and Moon templates, and the isotropic template. Point sources were fit to the data as a single template derived with the fluxes from the 3FGL catalog. The only differences from the Sample model of Ackermann et al. (2017a) and this simulation are: a PS mask was not used and the isotropic emission is forced to have a power-law spectrum (the index of the spectrum is fitted to the data). The data were fitted between 31.2 MeV and 312 MeV in 6 logarithmic bins. In order to derive the diffuse emission in two large energy bins 31.2 MeV – 100 MeV and 100 MeV – 312 MeV, the count rates of the diffuse components (all templates except the PS template) were summed in the 3 bins below 100 MeV and in the 3 bins above 100 MeV. For simplicity, the notations 30 – 100 MeV and 100 – 300 MeV are used in the following part to refer to the energy bins.

Parameter	Value
IRFs	P8R2_SOURCE_v6
Energy range	30-100 MeV/ 100-300 MeV
Pixel dimension	$0^{\circ}.458$
Interval of time	8.7 years
Number of sources	369
Flux	$10^{-8} - 10^{-4.5}$ cm^{-2}s^{-1}

Table 4.1: *Parameters used for the generation of MC maps.*

Two different setups were used for the generation of point sources. Both setups contain a population of 369 PS with a flux between 30 and 100 MeV randomly chosen from a flat distribution on the logarithmic scale between 10^{-8} cm^{-2}s^{-1} (which is close to the threshold of the detection) and $10^{-4.5}$ cm^{-2}s^{-1}. The parametric representation of the PS flux was obtained by taking the parametric representation of a random source in the 3FGL catalog and rescaling it so that the integrated flux between 30 and 100 MeV was equal to the randomly chosen flux from the flat distribution. In the first setup the PS were positioned in the sky in a grid with a separation of 10° (Figure 4.5), while in the second one they were randomly positioned in the sky (Figure 4.6). Figure 4.5 and all the following figures

refer to the energy bin 30–100 MeV. Table 4.1 contains the main parameters that were used in the simulation. The flux sampling from a flat distribution in the log space is useful for obtaining a good statistic of flux and position reconstruction at high fluxes (see, e.g., Figure 4.14). However, the corresponding source count distribution $dN/d\log S \propto const.$ is not realistic and may give detection and false positive rates which are not adequate for the expected populations of PS.

It was verified, for this reason, the detection rate and the false positive rate expectations by including all 3FGL sources in the simulations, where a random position in the sky for each source was used. The fluxes were obtained by integrating the parametric representations in 3FGL.

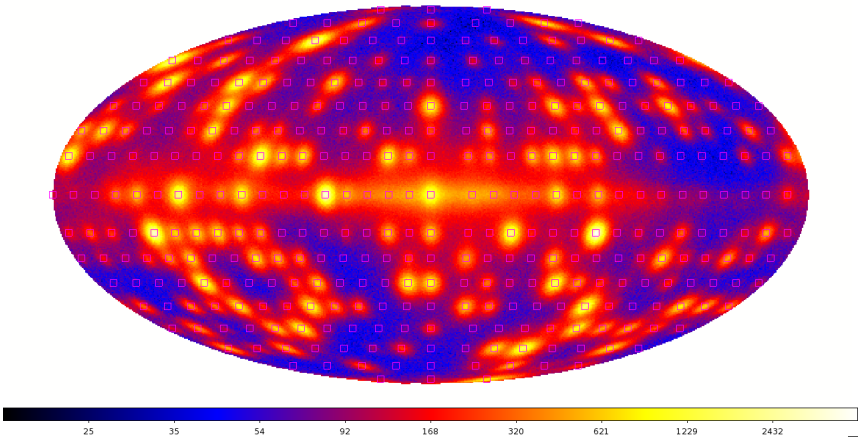

Figure 4.5: *Count map of the first setup (flat SdN/dS, positions on a grid) which contain 369 PS in a grid with 10° separation.*

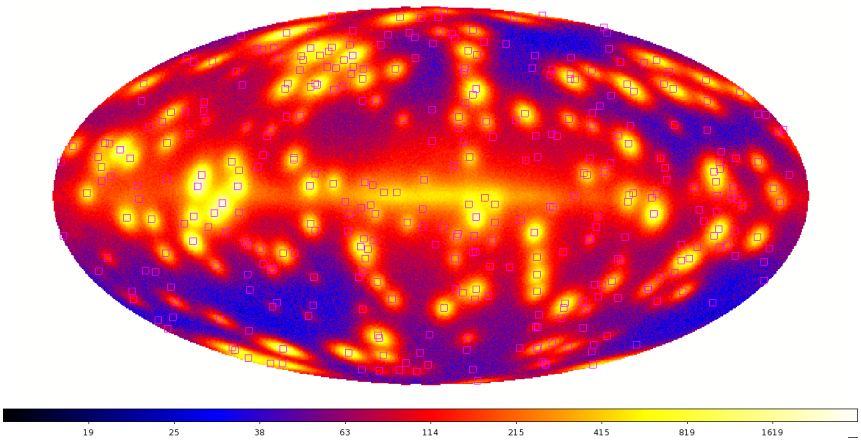

Figure 4.6: *Count map of the second setup (flat SdN/dS, random positions) which contains 369 PS randomly positioned in the sky.*

4.3 Point source analysis

The simulated γ-ray maps, presented in the previous section, are used here to optimize the parameters in our PS detection algorithm and to determine the localization and flux reconstruction uncertainties.

4.3.1 Source detection

A common problem for the analysis of point sources in the *Fermi*-LAT data is to determine an accurate Galactic diffuse emission model. If the diffuse model does not correctly reproduce the background of the sky, it can introduce large systematic errors in the PS detection and in the flux determination. In order to be less sensitive to the choice of the background model, this work makes use of a background-independent analysis method based on the wavelet transform implemented in the PGWave tool (for more information see Section 3.3.3). The threshold for detection was set to 3σ statistical significance. MC simulations were used to optimize parameters, such as the wavelet transform scale and the minimum distance between two sources, in order to maximize the detection efficiency and minimize the false positive rate, which are the ratio between the number of detected sources and the input sources and the ratio between the PGWave seeds that do not have an association and the total number of seeds.

Analysis procedure

All data, diffuse background, and MC maps were generated using HEALPix[2] (Górski et al. 2005) pixellation with $n_{side} = 128$ (pixel size$= \sqrt{\frac{4\pi}{N_{pixel}}} \approx 0.^{\circ}458$, with $N_{pixel} = 12n_{side}^2$). For the analysis, the HEALPix maps were projected to 12 regions of interest (ROIs) of size 180° in longitude and 90°in latitudeusing Mollweide (MOL) projection (Calabretta & Greisen 2002). The pixel size near the center of the ROIs is chosen to be $0.^{\circ}458$, so the HEALPix data are mapped as closely as possible to the MOL projection. The centers of ROIs are at $b = 0^{\circ}, \pm 60^{\circ}$and $\ell = 0^{\circ}, 90^{\circ}, 180^{\circ}, 270^{\circ}$. The centers of the ROIs are chosen in order to cover the entire sky, to have an overlap between nearby regions and to have a maximum distance between a considered point in the ROI and the local equator, namely the local x-axis in the center of the ROI, less than 30°. During the analysis, the dependency of the detection efficiency varying the distance from the local equator is studied. It was determined that the detection rate does not depend on the distance to the equator.

For each ROI, the wavelet transform was performed with the PGWave tool and the seeds that are closer to the border than 10°were eliminated in order to avoid edge effects. In the overlapping regions between different ROIs, the seeds were merged eliminating duplicates

[2] http://sourceforge.net/projects/healpix/

within 2° and giving a preference to the projection in which the source is closest to the equator.

In order to avoid contamination due to the diffuse emission, the previous steps of the analysis were repeated also for simulated maps of the Galactic and extra-galactic diffuse emission only. In the list, the seeds that match those in the purely diffuse maps were eliminated. Thus, a diffuse emission model (see Section 4.2) enters in the analysis indirectly: point-like features in the diffuse emission were eliminated from the list of the PS seeds. A comparison with the official diffuse emission model, provided by the *Fermi*-LAT collaboration (Acero et al. 2016), indicates that the two models are compatible and their difference results, on average, in one additional false positive point source.

Finally, the flux of the sources was estimated using the maxima in the wavelet transform (WT) map (referred to as WT peak values in the following for conciseness). Diffuse emission can also affect the determination of the flux by introducing fluctuations of the wavelet transform map on top of the Poisson noise from the sources. This effect was evaluated using MC simulations by comparing the input and the reconstructed fluxes (see Section 4.3.7).

4.3.2 Selection of data event type

At low energies, *Fermi* LAT has a PSF that increases from $\sim 5°$ at 100 MeV to $\sim 12°$ at 30 MeV (see also Figure 4.7). It is possible to improve the resolution by selecting events with a better angular resolution (e.g., PSF3 event type), but this subselection of events leads to a decrease of statistics.

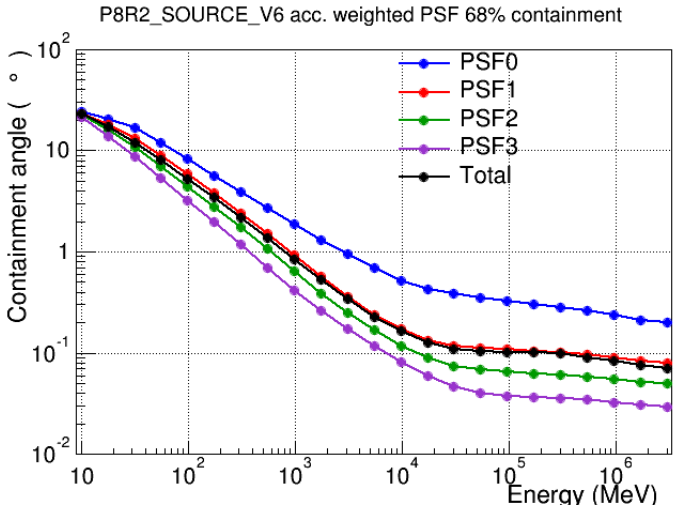

Figure 4.7: *LAT 68% containment angles of the acceptance weighted PSF for all the PSF event types. The plot is taken from http://www.slac.stanford.edu/exp/glast/groups/canda/lat_Performance.html.*

In order to find the optimal combination of PSF event types, the detection and false positive rates were compared for the following selections:

- all PSF event types combined together;
- PSF1, PSF2, and PSF3 event types;
- PSF2 and PSF3 event types;
- only PSF3 event type.

It was used here the same analysis pipeline that is described in Section 4.3.1. One of the most important parameters is the wavelet transform scale.

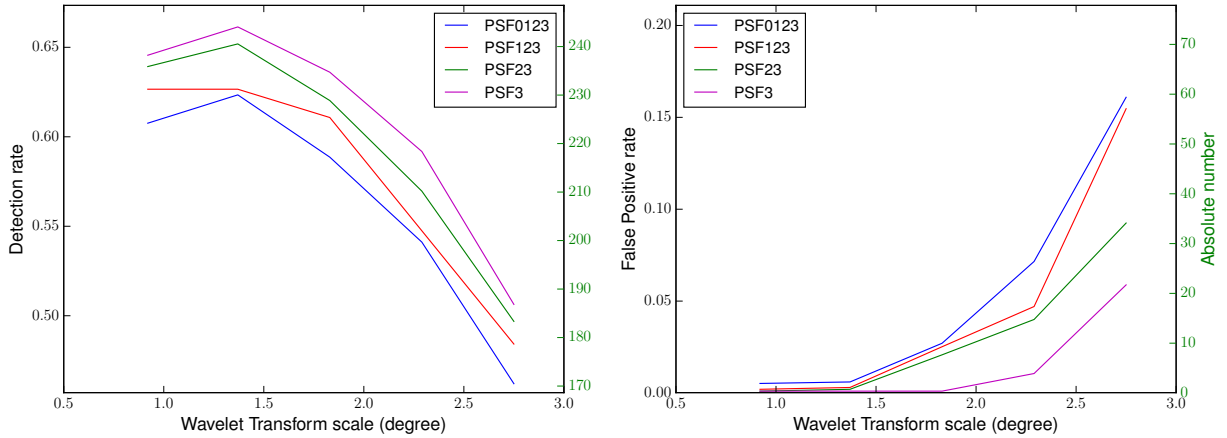

Figure 4.8: *Detection rate (left plot) and false positive rate (right plot) varying the dimension of the wavelet transform scale (setup containing 369 PS with flat SdN/dS and random positions). The plot refers to the 30 – 100 MeV band.*

Figure 4.8 contains the results of the detection and false positive rates for different combinations of PSF event types, where the WT scale was varied. The plots show that for the PSF3 event type the detection rate is the largest while the false positive rate is the smallest. A similar behavior was observed in the analysis using the grid setup. Both the grid and the random positions setups show that the PSF3 event type, even if it has smaller statistics, gives the best detection and false positive rates.

4.3.3 Selection of PGWave parameters

The main parameters of this analysis were optimized in order to maximize the detection rate and minimize the false positive rate. This analysis made use of simulated maps with 369 PS with flat SdN/dS and random positions in the sky (see Section 4.2). The

parameters that were optimized are reported in Table 4.2. The threshold was set at 3σ. The analysis was performed separately for both energy bins: 30 – 100 MeV and 100 – 300 MeV.

In this part, the detection and false positive rates were studied by varying the wavelet transform scale, the minimum number of connected pixels to define a peak and the minimum distance between the sources. In addition, the merging radius, which is the tolerance radius for merging the seeds from different ROIs (see analysis description), was also varied.

PGWave parameter	Values	Step
MH wavelet transform scale	0.9 - 3.6	0.46
Min number of connected pixels	2 – 8	1
Min distance between sources	1.8 - 2.7	0.46

Table 4.2: *List of PGWave parameters which were optimized in this analysis. Considering also the variation of the merging radius, more than 170 different combinations of the analysis parameters were tried.*

Figure 4.9 (left) shows an example of behavior of detection and false positive rates due to the variation of the minimum number of connected pixels, while Figure 4.9 (right) shows the rates as a function of the wavelet transform scale.

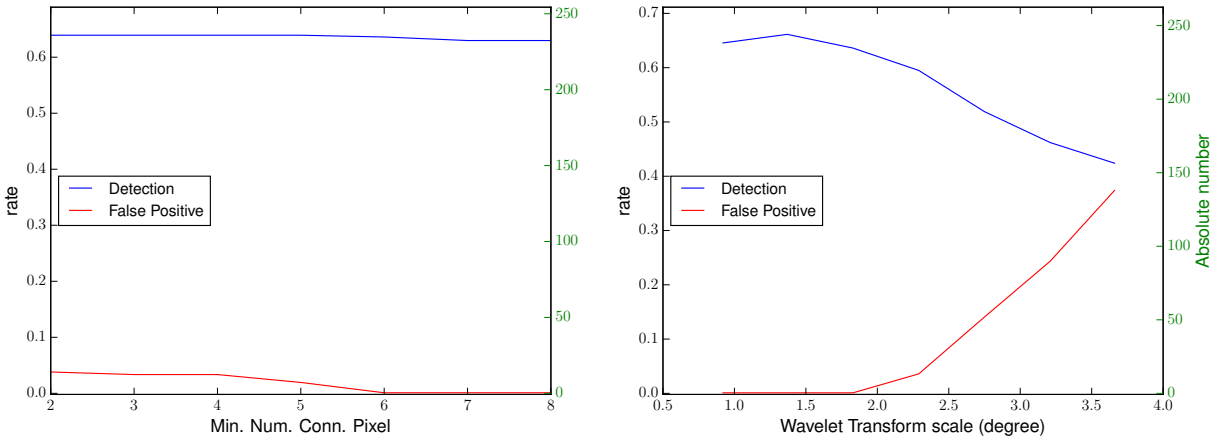

Figure 4.9: *Detection (blue line) and false positive (red line) rates as a function of the minimum number of connected pixels (left plot) and of the wavelet transform scale (right plot), for the setup containing 369 PS with flat SdN/dS and random positions. The plot refers to the 30 – 100 MeV band.*

For the analysis of the data, the PGWave parameters that maximize the detection rate keeping the false positive rate smaller than 3% were selected (similar to the 3FGL false positive rate). The optimal values of the parameters are reported in Table 4.3. The same parameters were observed to be optimal also for simulated maps with sources with

a flux extrapolated from the 3FGL and randomly positioned in the sky. For the analysis of the data, two different wavelet scales were chosen: 1.°4 (important to resolve source confusion, especially in the Galactic plane) and 1.°8 (important to detect faint sources at high latitudes). The expected number of spurious sources is equal to 5 in the energy bin 30 – 100 MeV (17 in the energy bin 100 – 300 MeV), so the total false positive rate is lower than 2% (6%). Figure 4.10 shows the difference in detection rate between the analysis combining two different wavelet scales and the same for the 1.°8 wavelet scale only and 1.°4 wavelet scale only.

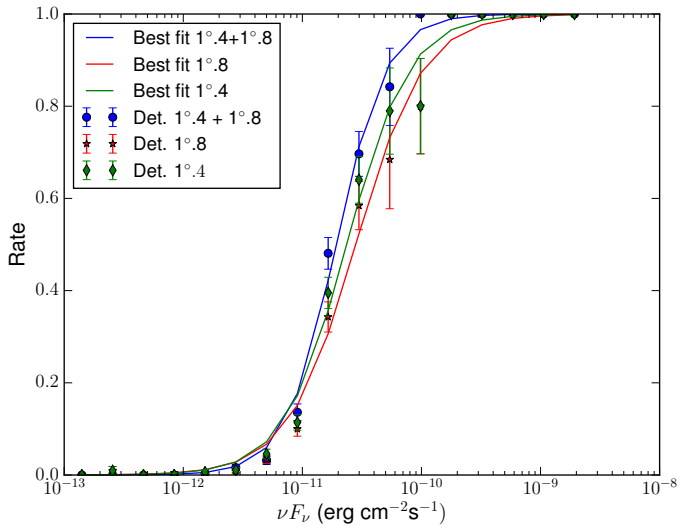

Figure 4.10: *Detection rate as a function of the input flux of the simulated PS with random position in the sky (setup containing extrapolated 3FGL sources with randomized position) for high latitude sources, namely* $|b| > 10°$. *Each point represents the ratio of detected sources using PGWave with respect to the number of input sources with a flux value inside the flux-bin. Blue: the detection rate of the combined analysis (wavelet scales of 1.°4 and 1.°8), red: the analysis with a wavelet scale of 1.°8 only, green: wavelet scale of 1.°4 only.*

PGWave parameter	Chosen value
MH wavelet transform scale	1.°8 (1.°4)
Min number of connected pixels	6 (5)
Min distance between sources	2.°7 (2.°3)

Table 4.3: *List of PGWave parameters resulting from the optimization. These values have been then used for the analysis of the data. The PGWave values of the second choices for the combined analysis are shown in parenthesis.*

4.3.4 Combined radii analysis

The MC simulations were also used to find the optimal wavelet transform radii, which give a high detection efficiency while keeping the false positive rate at a few per cent level at high latitudes (see previous section 4.3.3). The results of wavelet transforms with two radii (1.°4 and 1.°8) were combined together for the search of PS in the data. For radii smaller than 1.°4, the 68% containment radius at 100 MeV is much larger than the wavelet transform scale; as a result, the efficiency of detection of faint sources becomes smaller. For radii larger than 1.°8, the sensitivity becomes worse due to source confusion. In this analysis, the wavelet transform with the 1.°8 scale is important to detect faint sources at high latitudes, while the transform with the 1.°4 radius helps to improve source confusion, especially close to the Galactic plane. The results of analysis with 1.°4 and 1.°8 wavelet scales were therefore combined together. The preference was given to the results of the 1.°8 wavelet scale analysis: if a source is found in both the analyses, the position and the WT peak of the 1.°8 wavelet scale analysis were selected since this analysis is more sensitive to faint sources.

4.3.5 Detection efficiency

MC maps were used for the determination of the detection efficiency. They include diffuse emission and 3033 PS (obtained by extrapolating the 3FGL sources) with random positions in the sky (details on simulated maps can be found in Section 4.2). The analysis was applied to the simulated maps and the resulting sources were compared with the list of input sources in order to estimate the detection efficiency and the false positive rate.

Figure 4.11 shows the ratio of detected sources to the input MC sources in each of the flux bins for high latitude sources, namely $\mid b \mid > 10^{\circ}$, and Galactic sources. The detection efficiency was modeled by a hyperbolic tangent function $(1 + \tanh \lambda(f - f_0))/2$, where parameters λ and f_0 were determined by fitting the function to the detection efficiency points. Using this model at $\mid b \mid > 10^{\circ}$, and the obtained values of $\lambda = 1.079$ and $f_0 = 1.876 \times 10^{-11}$ erg cm^{-2}s^{-1} ($\chi^2 = 0.24$), it was found that PGWave has a detection rate larger than 95% for PS with νF_ν = Energy Flux/ $\ln(E_{max}/E_{min}) > 6.5 \times 10^{-11}$ erg cm^{-2}s^{-1} at 56 MeV.

4.3.6 Localization

The position of each source was first determined with PGWave, as the position of the WT maximum. Since PGWave returns the positions of the center of the pixel in which the WT has a maximum, the reconstruction of the position was optimized using a parabolic fit in a 5×5 pixel grid around the maximum. In the following, the estimation of the systematic and statistical uncertainty for the localization are reported.

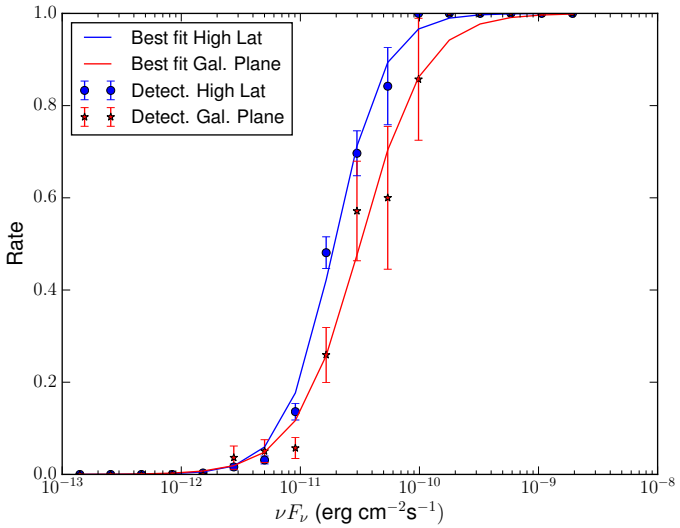

Figure 4.11: *Detection rate as a function of the input flux of the simulated PS with random position in the sky (setup containing extrapolated 3FGL sources with randomized position, see Section 4.2). Each point represents the ratio of detected sources using PGWave with respect to the number of input sources with a flux value inside the flux bin. The error bars corresponds to the statistical uncertainty derived with the binomial distribution.*

Optimized Localization

The PGWave tool determines the position of the sources as the center of the pixel where the WT has a maximum. This reconstruction is limited by the dimension of the pixel (0.°458). The source localization was optimized by fitting a two-dimensional parabolic function to the wavelet-transformed map in a 5×5 pixel grid around the maximum. The PGWave position was corrected only for the cases where the fit converges inside the 5×5 pixel grid, for the other cases the position directly determined by PGWave was returned. This optimization allows improving the localization and reducing the systematic uncertainty. Figure 4.12 shows the distance between input and reconstructed position given by PGWave or the reconstructed position where the parabolic function was fitted to the wavelet transformed map. 98% of the sources have a reconstructed position that is localized at less than 1.°5 from the input position. This value was then used for the tolerance radius in the association algorithm (see Section 4.3.9).

Systematic and statistical uncertainty for the localization

Ten realizations of simulated maps were made to determine the statistical and systematic uncertainties of the localization. Each simulated map contains 369 PS randomly positioned in the sky (see Section 4.2).

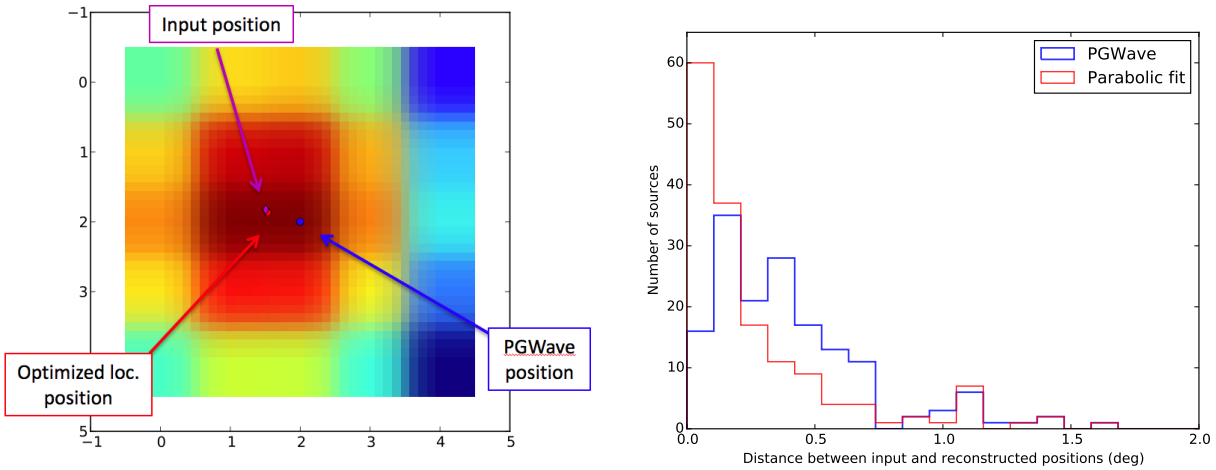

Figure 4.12: *Left: example of the localization optimization with the parabolic fit. It shows the wavelet transformed map with the input position of the simulated source (magenta point), the position of the seeds returned by PGWave (blue point) and the optimized position obtained using the parabolic fit (red point). Right: histogram of the distance between the input position and the reconstructed position determined by PGWave, or by the parabolic function fit. The plot was obtained with the simulated map with "random" setup.*

In order to determine the statistical uncertainty, for each PS (k) the 1D dispersion of the reconstructed PS positions relative to the average position (in 2D) of the source in the MC realizations was estimated:

$$\sigma_k = \sqrt{\frac{\Sigma_n (X_{PGW_i} - X_{PGW_{mean}})^2}{2(n-1)}}, \tag{4.1}$$

where $n = 10$ is the number of MC realizations, X_{PGW_i} and $X_{PGW_{mean}}$ are the coordinates of the reconstructed position in the i-realization and of the average reconstructed position over all the realizations. Then, the dispersion was averaged among all the detected sources in five flux bins:

$$\sigma_{stat} = \sqrt{\frac{\Sigma_k \sigma_k^2}{N}}, \tag{4.2}$$

where N is the number of sources in a flux bin.

For the systematic uncertainty, the deviation between the averaged position of ten realizations and the input position of the PS was measured:

$$\sigma_{syst} = \sqrt{\frac{\Sigma_k (X_{PGW_{mean}} - X_{in})^2}{2N}}, \tag{4.3}$$

where X_{in} is the input position of the reconstructed source. Figure 4.13 shows the statistical and systematic uncertainty in the localization. The total error in the localization is dominated by the systematic uncertainty. The value of the systematic uncertainty is smaller than 0.°3 in the energy range 30 – 100 MeV and smaller than 0.°2 in the energy range 100 – 300 MeV.

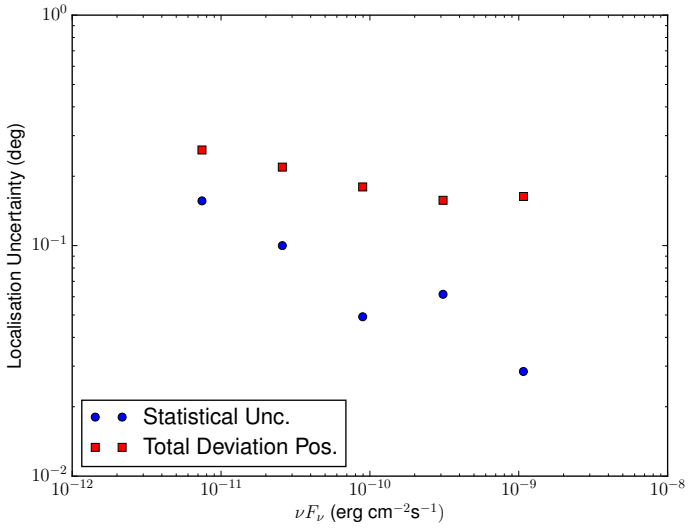

Figure 4.13: *Statistical (blue circles) and systematic (red squares) uncertainty of the PGWave localization for the energy bin 30 – 100 MeV. The uncertainties are reported as the 68% containment radius.*

4.3.7 Flux determination

The WT peak value was used for the estimation of the flux of sources detected by PGWave. because a linear correlation is expected between the flux and the WT peak value (Principe & Malyshev 2016). In order to compare the results with the 3FGL catalog, the maps in the energy bin 100 – 300 MeV were also analyzed using the same procedure as in the 30 – 100 MeV bin. Figure 4.14 (left) shows the correlation between the input MC flux and the WT peak values. The red line in the plot represents the best fit with a power-law function $f = kx^{\alpha}$, where $\alpha = 1$, which is expected by the definition of the WT (Section 3.3.3). A model, with the fixed power law index $\alpha = 1$, was compared to a model with α fitted to the data (best-fit value $\alpha = 1.02$). The difference between the two models in the reconstructed flux is less than 5%, which is much smaller than the obtained systematic uncertainties (see below). As a result, the simpler model with $\alpha = 1$ was used. The power law factor f is equal to 3.54×10^{13}, for the energy range between 30 and 100 MeV, and 7.18×10^{13}, for the energy range between 100 and 300 MeV. The results of the best fit were then used for estimating the flux from the WT peak values.

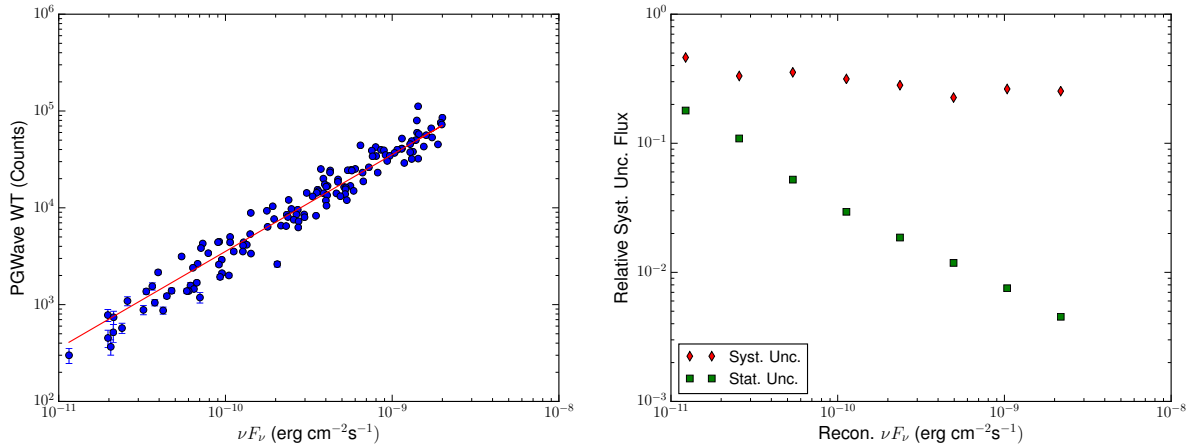

Figure 4.14: *Left: PGWave seeds associated with the input PS in the energy bin 30 – 100 MeV. X-axis: MC input flux, y-axis: the WT peak value from PGWave. The red line represents the best fit. The relation is plotted for the wavelet transform with radius 1°.8. Right: Statistical (green points) and systematic (red points) uncertainty of flux reconstruction using PGWave in the energy range 30 – 100 MeV.*

All the sources were divided in bins of WT peak values in order to derive the systematic uncertainty of flux reconstruction. Inside each bin the standard deviation of the difference between the input MC flux and the PGWave best fit was calculated. The statistical uncertainty is directly calculated by PGWave. Figure 4.14 (right) shows the systematic and statistical uncertainties in the flux reconstruction. The uncertainty is dominated by the systematic one. In the energy range 30 – 100 MeV, the error decreases as a function of flux from a relative value of $\sim$ 40%, for faint sources, to a value of $\sim$ 20%, for bright sources. Similarly the error in the energy range 100 – 300 MeV decreases as a function of the flux from a relative value of 35%, for faint sources, to a value of 10%, for bright sources.

4.3.8 PGWave significance

For the determination of the PS significance, MC maps were used. They include diffuse emission and PS with random positions in the sky (details on simulated maps can be found in Section 4.2). The spectra of the input PS were determined from extrapolation of the spectra of PS randomly selected from the 3FGL catalog. The analysis was applied to the simulated maps and the resulting sources were compared with the list of input sources in order to estimate the correlation between the PS significance and the input MC flux for each PS.

Figure 4.15 shows, for each seed detected with PGWave, the correlation between the input MC flux and the significance estimated by the wavelets tool. Using a power-law

function ($f = kx^{\alpha}$) to fit the data and the obtained fit parameters ($k = 2.6 \times 10^{10}$ and $\alpha = 0.9$), it was found that PGWave has a significance greater than 5σ for PS with a energy flux $\nu F_{\nu} > 1.3 \times 10^{-11}$ erg cm^{-2} s^{-1}. This value was used as an estimate of the statistical sensitivity of the method in Figure 5.9.

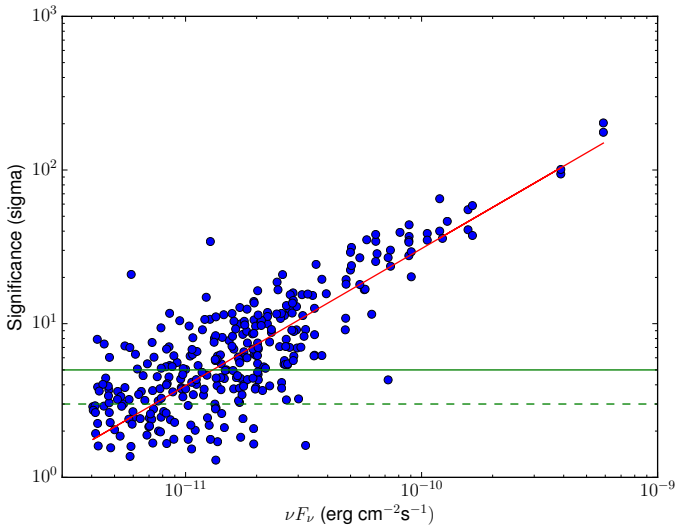

Figure 4.15: *PGWave significance vs input MC flux (setup containing extrapolated 3FGL sources with randomized position). The red line represents the best fit with a power-law function ($f = kx^{\alpha}$). Green continues line: the 5 sigma significance used for estimating the statistical sensitivity, green dashed line: the 3 sigma significance threshold applied for the point source detection.*

4.3.9 Association of point sources

The algorithm of PS association is based on positional coincidence with a tolerance radius of 1.°5, which is smaller than the angular resolution of PSF3 event type at 100 MeV (3°), and on a flux ordering. The tolerance radius was chosen as the distance at which 98% of the reconstructed sources find the correctly associated input sources (see Section 4.3.6). The flux ordering algorithm associates seeds with a large WT peak value to bright MC input sources (or bright PS in a catalog when compared, e.g., to the 3FGL *Fermi*-LAT catalog or the catalog of COMPTEL sources below), this allows a better association in cases where more than one source is present inside the tolerance radius.

CHAPTER 5

Results on the first catalog of *Fermi*-LAT sources below 100 MeV

This chapter presents the results of the first *Fermi* Large Area Telescope (LAT) low energy (1FLE) catalog of sources detected in the energy range 30 – 100 MeV. The imaging Compton telescope (COMPTEL) onboard NASA's *Compton Gamma-Ray Observatory* detected sources below 30 MeV, while catalogs of point sources released by the *Fermi*-LAT and EGRET collaborations use energies above 100 MeV. Because the *Fermi* LAT detects γ rays with energies as low as 20 MeV, a catalog of sources detected in the energy range between 30 and 100 MeV was made in this work. The 1FLE catalog closes a gap of point source analysis between the COMPTEL catalog and the *Fermi*-LAT catalogs. One of the main challenges in the analysis of point sources is the construction of the background diffuse emission model. In this analysis, a background-independent method was used to search for point-like sources based on a wavelet transform implemented in the PGWave tool.

In Section 5.1 the general results of the 1FLE catalog are presented. The results are then compared, in Section 5.2, to the the 3FGL catalog derived above 100 MeV (Acero et al. 2015), and in Section 5.3 to the the COMPTEL catalog of sources at energies between 1 and 30 MeV (Schönfelder et al. 2000). Particular attention is given, in this work, to the 1FLE blazars. Section 5.4 presents a list of 1FLE AGNs, which were flaring either during the 3FGL observation time or after the 3FGL observation time. Finally, Section 5.5 contains a discussion about the sensitivity of the point source analysis performed for the 1FLE catalog.

These results are published in Principe et al. (2018b) and therefore the next sections follows it closely and in large parts in verbatim.

5.1 General characteristic of 1FLE sources

LAT data used

The 1FLE catalog was made with eight years and nine months of the *Fermi*-LAT Pass 8 Source class events, with the P8R2_SOURCE_v6 instrument response functions (IRFs), between August 4, 2008 and May 3, 2017 (*Fermi* Mission Elapsed Time 239557418 s–515548139 s). The data were divided in logarithmic energy bins with two bins per decade: 31.6 – 100 MeV and 100 – 316 MeV. The second energy bin, 100 – 316 MeV, is used for a crosscheck with the 3FGL. For simplicity, the notation 30 – 100 MeV and 100 – 300 MeV is in the following part used to refer to the energy bins. Events with an angle $\theta < 90°$with respect to the local zenith were selected, in order to reduce contamination from cosmic-ray interactions in the Earth atmosphere.

In Section 4.3.2 it is shown that using only PSF3 event type gives the highest detection efficiency and the smallest false positive rate. Consequently, only the PSF3 event type was used in this work. Figure 5.1 shows the counts map for the first eight years and nine months of the *Fermi*-LAT data between 30 and 100 MeV with PSF3 event type.

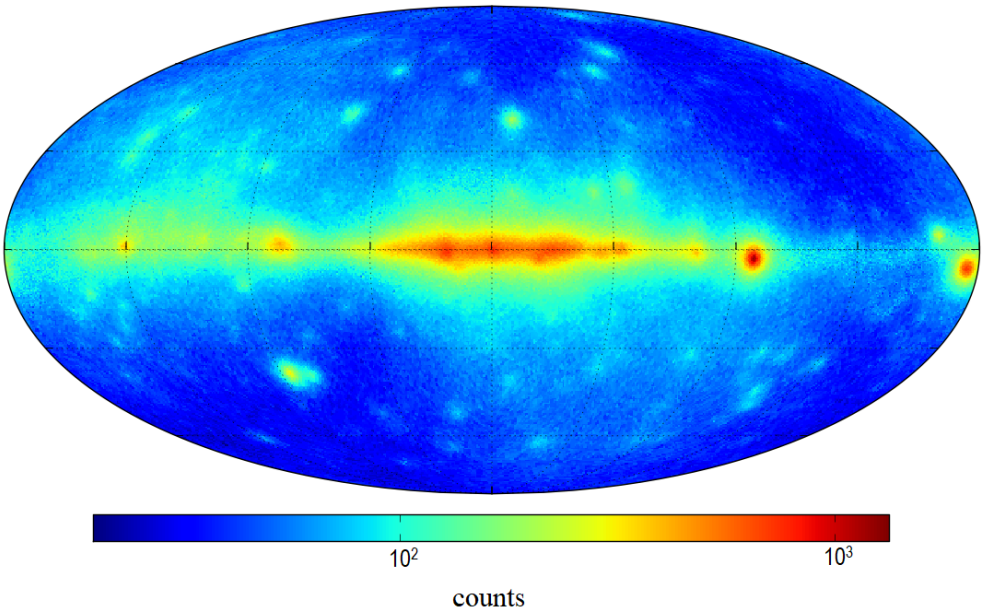

Figure 5.1: *Fermi-LAT count map, for the first eight years and nine months of observation, in the 30 – 100 MeV band represented in Galactic coordinates and Mollweide projection. The color scale is logarithmic and the units are counts per pixel (pixel size equal to 0.°458).*

1FLE results

The 1FLE catalog includes 198 sources detected over the whole sky that are not associated with significant seeds in the PGWave transform of the purely diffuse model map. A statistical confidence of more than 3σ is required for a source detection. With the optimized parameters for the analysis (see Section 4.3.3) the expected number of spurious sources is about five.

Figure 5.2 shows the distribution of the flux between 30 and 100 MeV of the sources contained in the 1FLE.

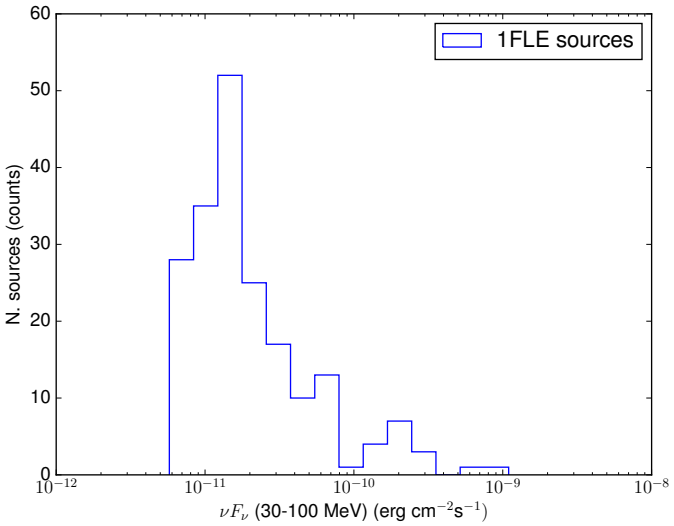

Figure 5.2: *Histogram of the flux between 30 and 100 MeV of the sources in 1FLE.*

The 1FLE sources have fluxes (νF_ν) between 30 and 100 MeV in the range from 7×10^{-12} erg cm^{-2} s^{-1} to 10^{-9} erg cm^{-2} s^{-1}. The two brightest sources are the Vela pulsar and Crab pulsar and pulsar wind nebula. In this work, the pulsed emission from the Crab pulsar was not analysed, therefore it is not possible to separate the flux from the pulsar itself and the pulsar wind nebula. In the following, for the flux of the Crab pulsar, the combined emission from the pulsar and from the pulsar wind nebula is reported.

Figure 5.3 shows the locations of the 1FLE sources in the sky. Most of the 1FLE sources (157) are at high latitude ($\mid b \mid > 10^\circ$); only 41 are at low latitude.

The method used in this work is less sensitive to sources in the Galactic plane than likelihood methods, because the rejection of the seeds that match those from the purely diffuse emission map (see Section 4.3.1). This results in the exclusion of about 6% of pixels within $|b| < 10^\circ$due to masking of $1.^\circ5$ circles around 60 seeds found in the purely diffuse model.

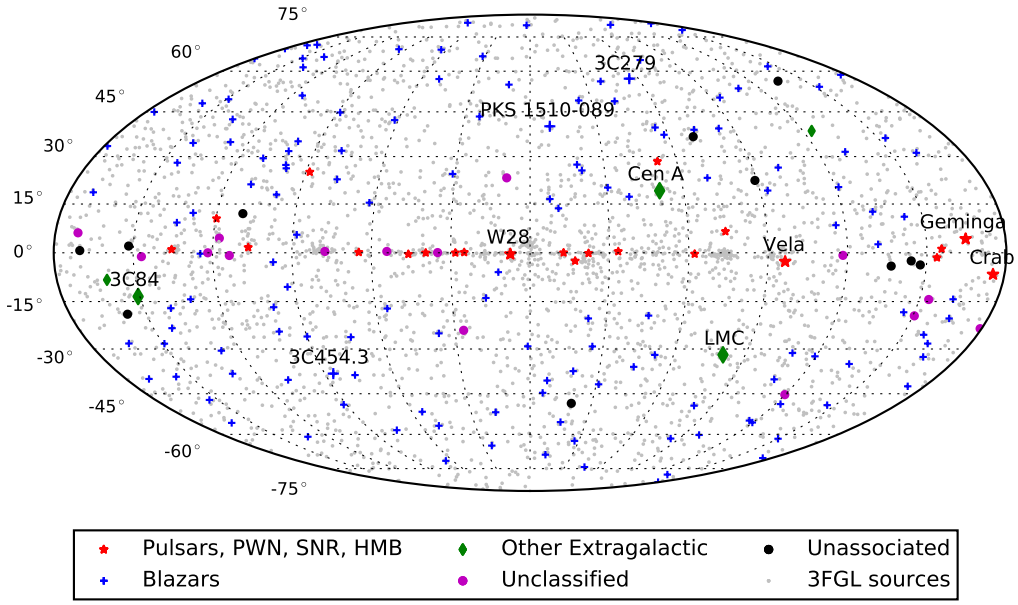

Figure 5.3: *Sky map, in Galactic coordinates and Mollweide projection, showing the sources in the 1FLE catalog classified by their most likely association, using the 3FGL association. All the 3FGL sources are also plotted, with gray points, for a comparison.*

5.2 Comparison with 3FGL

In this section, the 1FLE sources are compared to the 3FGL catalog (Acero et al. 2015). The 3FGL is based on the first four years of the *Fermi*-LAT data between 100 MeV and 300 GeV using the Pass7 reprocessed event reconstruction. It contains 3033 sources: 33% have no high-confidence counterparts at other wavelength and more than 1100 of the identified or associated sources are active galaxies of the blazar class. The 1FLE contains 198 sources and 187 of them have associations in the *Fermi*-LAT 3FGL catalog. Analysis with 1.°8 wavelet transform gives 174 sources: 144 sources are at high latitudes (four have no counterpart in 1.°4 analysis) and 30 sources are at low latitudes (four have no counterpart in 1.°4 analysis). Analysis with 1.°4 wavelet transform gives 168 sources: 132 sources are at high latitudes (five have no counterpart in 1.°8 analysis) and 36 sources are at low latitudes (three have no counterpart in 1.°8 analysis). Combining the results of analysis

Description	Associated designator	Number
Pulsar	psr	12
Pulsar wind nebula	pwn	2
Supernova remnant	snr	2
Supernova remnant / pulsar wind nebula	spp	5
High mass binary	hmb	1
BL Lac type of blazar	bll	31
Flat spectrum radio quasar type of blazar	fsrq	98
Narrow-line seyfert 1	nlsy1	1
Radio galaxy	rdg	3
Steep spectrum radio quasar	ssrq	1
Normal galaxy (or part)	gal	1
Blazar candidate of uncertain type	bcu	13
Unclassified	”	17
Unassociated	-	11
Total in the 1FLE		198

Table 5.1: *Source classes of the 1FLE sources determined using the 3FGL associations.*

with 1.°4 and 1.°8 wavelet scale, there are five sources at low latitudes and six sources at high latitudes without associations in the 3FGL catalog. Among the associated sources, 148 are extragalactic, 22 are Galactic, and 17 are unclassified in the 3FGL. More details about the 1FLE sources can be found in Table 5.1.

About 94% of the sources contained in the 1FLE have found an association in the 3FGL catalog using the algorithm for the association with a tolerance radius of 1.°5 (see Section 4.3.9). The much smaller number of sources in 1FLE compared to, for example, the 3FGL catalog is due to several factors: the effective area of the instrument between 30 – 100 MeV (<0.35 m^2) is much smaller than above 1 GeV (>0.9 m^2); the angular resolution, even for the PSF3 event type, is larger than 3° for energies below 100 MeV, while the angular resolution above 1 GeV is better than 0.°5; in the analysis it is used a wavelet filtering method rather than the maximum likelihood, which takes into account the precise shape of the point-spread function.

In spite of the different energy range and the longer time interval of 1FLE relative to 3FGL, all significant 1FLE sources have associations with 3FGL sources. One of the main reasons for that is the lower sensitivity of the *Fermi* LAT at low energies due to smaller effective area and worse angular resolution compared to higher energies (the *Fermi*-LAT PS sensitivity is the best around a few GeV, see Figure 5.9). In this work, the 1FLE was also compared to the preliminary *Fermi*-LAT eight year list of sources (FL8Y)[1]. The FL8Y has a similar time interval as this analysis. There are several sources in FL8Y which have a flux extrapolated below 100 MeV above the statistical sensitivity threshold of 1FLE. Most of these sources are in the Galactic plane, where the wavelet transform has difficulty

[1]https://fermi.gsfc.nasa.gov/ssc/data/access/lat/fl8y/

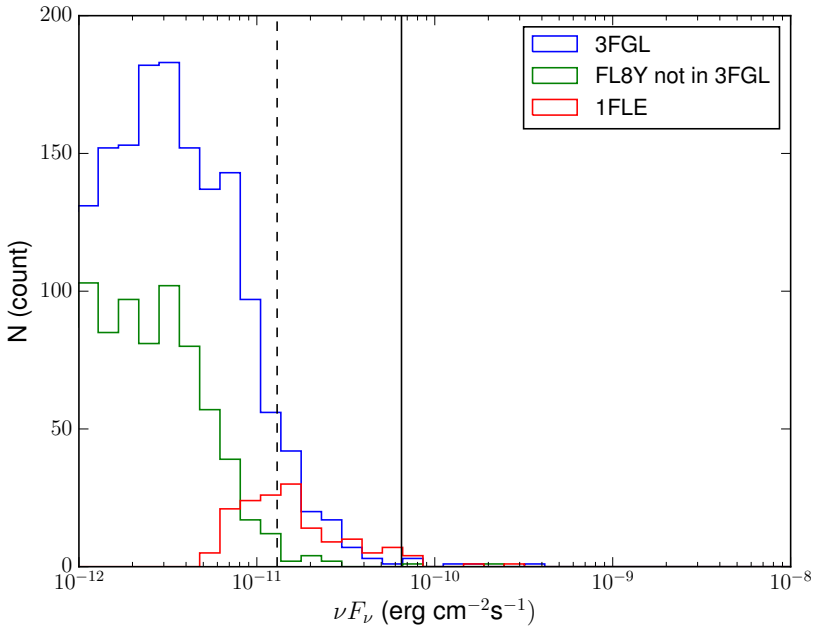

Figure 5.4: *Comparison, outside the Galactic plane, of the extrapolated flux distribution of the 3FGL and the FL8Y sources, not already included in the 3FGL, with respect to the flux distribution of the 1FLE sources. The x-axis corresponds to the νF_ν value in the 30–100 MeV band. The dashed and normal black lines corresponds to the statistical and total sensitivity of the 1FLE catalog. The plot shows that there are not sufficiently bright flaring sources after 3FGL time interval, contained in the FL8Y list, which were not already detected by 3FGL.*

in separating the PS from the diffuse background. The sources above a galactic latitude of $|b| = 10°$ are either relatively close to to the plane (within $|b| = 15°$) or close to other bright sources so that they fall in the negative tail of the wavelet transform of the bright source. There are two consequences of the non-observation of new sources in 1FLE:

- there were no sufficiently bright flaring sources after the 3FGL time interval, which were not already detected by 3FGL (see Figure 5.4),
- there are no bright sources with a very soft spectrum, for example, a cutoff around 100 MeV: sources of this type would not be detected in either the 3FGL catalog or the FL8Y list.

5.2.1 1FLE Blazars

The 1FLE contains 148 extragalactic sources that have associations in the 3FGL catalog. The 3LAC catalog (Ackermann et al. 2015) contains the 3FGL AGNs, located at high

Galactic latitudes ($| b | > 10^{\circ}$), that have been detected in the energy range 100 MeV – 300 GeV, between August 4, 2008 and July 31, 2012. The 3LAC includes 1591 objects with 467 (29%) FSRQs, 632 (40%) BL Lacs, 460 (29%) BCUs and 32 (2%) non-blazar AGNs.

The ratios of PS associated with FSRQ and with BL Lacs are different in 1FLE and in 3LAC catalogs. Among the 148 extragalactic sources contained in the 1FLE, 98 (66%) are associated to FSRQ, 31 (21%) to BL Lacs, 13 (9%) to BCUs and 6(4%) to non-blazar AGNs. The much larger fraction of FSRQs is to be expected, since the sources at lower energies than 3LAC are studied in this work. Consequently, this method is more sensitive to soft spectrum PS, which is typical for FSRQs compared to BL Lacs.

Figure 5.5 shows the fraction of FSRQs with respect to the sum of FSRQs and BL Lacs varying the energy range used for the point source analysis in the following γ-ray catalogs: 1FLE, 3LAC, 3FHL (Ajello et al. 2017) and TeVCat[2]. The ratio of BL Lac (FSRQ) blazars

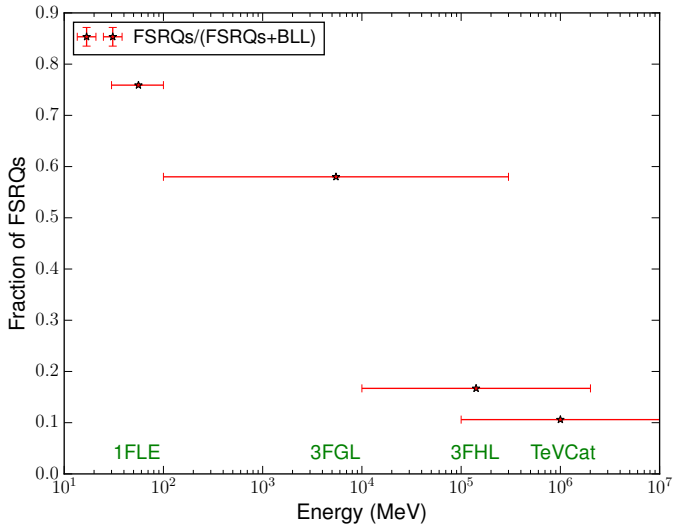

Figure 5.5: *Fraction of FSRQs with respect to the sum of FSRQs and BL Lacs contained in each γ-ray catalog versus the corresponding energy range used for the point source analysis.*

increases (decreases) with the observed energy. Table 5.2 shows the mean values of the redshift for each class of blazars.

In this work, the Kolmogorov-Smirnov (KS) test was used to compare the distributions of redshifts for each type of blazar in 3LAC compared to the subset of blazars of this type that is also found in 1FLE. Considering the redshift distribution of all blazars, the two distributions (1FLE and 3LAC) have different averaged redshift ($z_{1FLE} = 1.06 \pm 0.06$ and $z_{3LAC} = 0.84 \pm 0.02$) and they are not consistent with each other according to the KS test, which has the p-value of 8.1×10^{-6}. The distributions of the FSRQ are consistent between the two catalogs (p-value of the KS test is 0.964), while the BL Lac distributions

[2]http://tevcat.uchicago.edu/

Blazar class	1FLE z_{av}	3LAC z_{av}	KS test p-value
All blazars	1.06 ± 0.06	0.84 ± 0.02	8.1×10^{-6}
FSRQ	1.22 ± 0.06	1.21 ±0.03	0.964
BL Lac	0.59 ± 0.09	0.41 ± 0.02	0.018
Other blazars	0.55 ± 0.17	0.33 ±0.04	0.124

Table 5.2: *1FLE Blazar classes and corresponding average redshift determined using the 3LAC association. The label 'KS test' refers to the value of the Kolmogorov-Smirnov test for the redshift distributions of the 1FLE and 3LAC sources of the considered class of blazars.*

are not fully consistent: p-value of the KS test is 0.018 (see also Figure 5.6). The redshift distribution of FSQR in the 1FLE is consistent with the FSRQ redshift distributions in the other catalogs (apart from TeVCat, due to the small number of FSRQs in the catalog). The 1FLE BL Lacs have an average redshift ($z_{1FLE} = 0.59 \pm 0.09$), which is larger than the average redshift of all BL Lacs in the 3LAC ($z_{3LAC} = 0.41 \pm 0.02$). This is in agreement with the larger number of low-synchrotron peaked blazar type in the 1FLE (18 out of 31), which have softer spectra and higher redshifts than BL Lacs on average, with respect to the same one in the 3LAC (162 out of 632). The average redshift for the BL Lacs (Figure 5.6-right) is larger than the average redshift for these sources in the other catalogs.

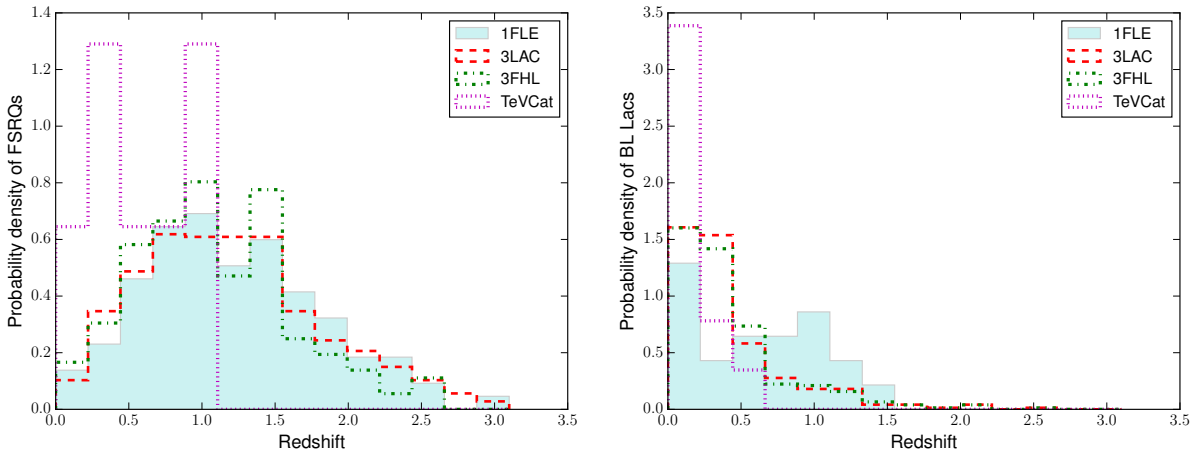

Figure 5.6: *Distributions of known redshifts for FSRQs (left plot) and for BL Lacs (right plot).*

5.2.2 1FLE sources not associated to the 3FGL

Table 5.3 reports the information about the 11 1FLE sources that have no association in the 3FGL catalog. Among those sources, five (1FLE J0422+5243, 1FLE J0647-0345, 1FLE J0655-1106, 1FLE J0522+3734 and 1FLE J0637-0110) are inside the Galactic plane ($| b |<$

10°) where the diffuse model has various structures that could influence the background elimination in the PGWave tool and six of them are outside the Galactic plane.

The 1FLE J2206+7040 source is inside a particular region where the diffuse emission has some bright features; however there are no evident peaks of WT of the diffuse map in that position. The 1FLE J0330+3304 and 1FLE J1203-2504 sources are surrounded by 3FGL sources. Although they do not have an association in the 3FGL, they are probably connected to the 3FGL sources: due to the large PSF in the energy range 30 – 100 MeV, if there are two or more sources close to each other, they could form a single structure in the counts map and PGWave does not distinguish the different sources but returns a seed in the middle. There are no 3FGL sources in the local region around 1FLE J1033+1601, 1FLE J2158-5424 and 1FLE J1030-3133. They are therefore good candidates for new sources in the gamma energy band, although the significance is less than 4σ.

Source name	GLON (deg)	GLAT (deg)	Err_pos (deg)	Signif. (σ)	νF_ν(30-100 MeV) 10^{-12} erg cm^{-2} s^{-1}	νF_ν (100-300 MeV) 10^{-12} erg cm^{-2} s^{-1}	Comment
1FLE J2206+7040	110.02	12.06	0.25	4.38	23.75 ± 7.16	0.0 ± 0.0	Diffuse
1FLE J0330+3304	157.42	-18.94	0.25	9.87	23.56 ± 7.10	0.0 ± 0.0	3FGL sources
1FLE J0422+5243	151.75	2.07	0.25	7.00	22.73 ± 6.85	0.0 ± 0.0	Gal. plane
1FLE J0647-0345	215.89	-2.48	0.25	7.75	17.71 ± 5.34	0.0 ± 0.0	Gal. plane
1FLE J0655-1106	223.33	-4.08	0.25	4.01	14.93 ± 4.94	4.07 ± 1.63	Gal. plane
1FLE J0522+3734	170.17	0.68	0.25	5.00	13.66 ± 4.52	0.0 ± 0.0	Gal. plane
1FLE J0637-0110	212.35	-3.72	0.25	4.80	10.88 ± 3.6	0.0 ± 0.0	Gal. plane
1FLE J1033+1601	224.87	56.14	0.25	3.65	10.30 ± 3.41	0.0 ± 0.0	$\sigma < 4$
1FLE J2158-5424	339.89	-48.37	0.25	3.99	8.51 ± 2.82	0.0 ± 0.0	$\sigma < 4$
1FLE J1203-2504	289.40	36.53	0.25	4.07	8.39 ± 2.77	0.0 ± 0.0	3FGL sources
1FLE J1030-3133	270.81	22.38	0.25	3.43	7.11 ± 2.35	0.0 ± 0.0	$\sigma < 4$

Table 5.3: *1FLE sources that do not have an association in the 3FGL catalog. For a more detailed description, see Section 5.2.2.*

5.3 Comparison with 1st COMPTEL Catalog

COMPTEL provided the first complete all-sky survey in the energy range 0.75 – 30 MeV. The first COMPTEL catalog Schönfelder et al. (2000) contains 26 steady sources: nine pulsars, four other Galactic sources, ten AGNs and three unidentified high-latitude sources. Eight out of the ten COMPTEL AGNs are associated to the 1FLE sources.

Regarding the two COMPTEL AGNs without association in the 1FLE, one (PKS 0528+134) is close to the Galactic plane in a region of significant structures in the diffuse emission and the other one (GRO J0516-609) is a flaring source observed by COMPTEL only between 1–10 MeV, it has no association also in the 3FGL. The 1FLE contains five pulsars detected also by COMPTEL: Crab, Geminga, Vela, PSR B1055-52 and GRO J2227+61. Most of the COMPTEL sources without an association in the 1FLE are in the Galactic plane, so they could be masked, in this analysis, by peaks of the diffuse emission. Among the other Galactic sources contained in the COMPTEL catalog, Nova Per 1992,

which is a transient X-ray binary, and Cygnus X-1, which is a persistent X-ray binary, have no associations also in the 3FGL catalog. All the COMPTEL unidentified sources have association neither in the 3FGL nor in any other *Fermi* source catalog.

Figure 5.7 show examples of the spectral energy distributions for some of the γ-ray sources detected in 1FLE. The fluxes from the COMPTEL and the 3FGL catalogs are also reported for a comparison.

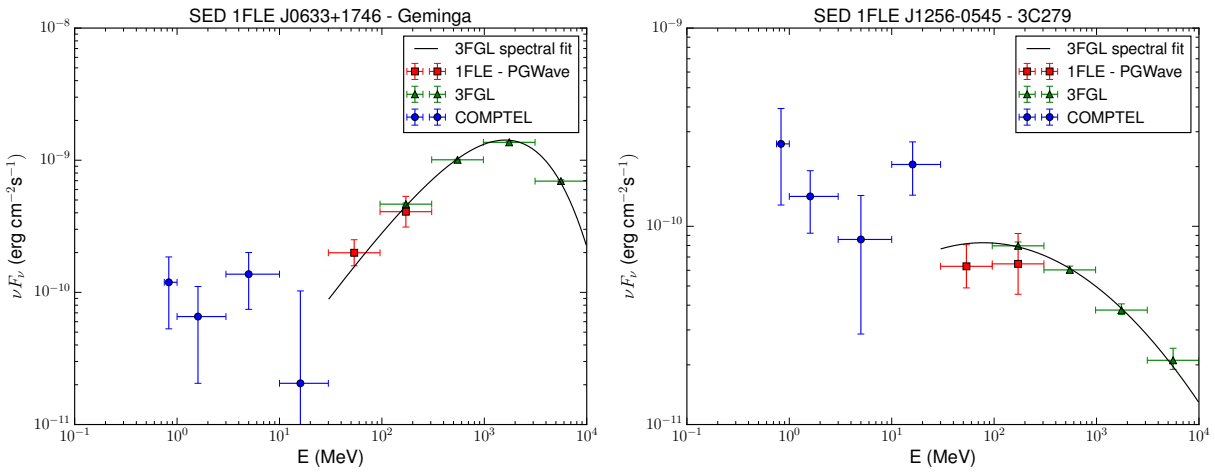

Figure 5.7: *Spectral energy distribution of Geminga (on the left) and of 3C279 (on the right). Red squares: flux derived with the PGWave analysis (interval time 2008 - 2017), blue circles: COMPTEL flux values (interval time 1991 - 2000), green triangles: flux from the 3FGL catalog (interval time 2008 - 2012), black line: 3FGL spectral fit.*

5.4 Comparison of 1FLE fluxes with 3FGL

There are several sources in the 1FLE catalog whose fluxes in the 30 - 100 MeV and 100 - 300 MeV bands differ significantly from the fluxes of the associated 3FGL sources. Several of these sources are associated with AGNs, which had flares either during the 3FGL observation time or after the 3FGL observation time (see Table 5.4). For these sources, the flux estimates obtained in this work are closer to the fluxes given in FL8Y.

Figure 5.8 shows the SED of 1FLE J1503+1033, which had a flare during the 3FGL observation time, therefore the 1FLE flux averaged over 8.7 years is smaller than the 3FGL one, and the SED of CTA 102, which had a flare after the 3FGL observation time, therefore the 1FLE flux is higher than the 3FGL one.

For other sources the difference can be attributed either to the presence of several 3FGL sources close to each other and unresolved by the wavelet transform (i.e., 1FLE J0329-3724, 1FLE J1047+7131 and 1FLE J1838+6812) or by the presence of a bright source within 7

Source Name	GLON (deg)	GLAT (deg)	1FLE νF_ν(100-100 MeV) 10^{-12} erg cm^{-2} s^{-1}	3FGL νF_ν (100-300 MeV) 10^{-12} erg cm^{-2} s^{-1}	Flare comment
1FLE J0424-0042	194.8	-32.6	5.49 ± 2.19	18.79 ± 1.17	flare in 3FGL
1FLE J0443-0024	197.5	-28.2	6.26 ± 2.50	19.72 ± 0.86	flare in 3FGL
1FLE J1224+2118	255.5	81.6	49.77 ± 14.79	83.52 ± 1.12	flare in 3FGL
1FLE J1227+0218	289.1	64.6	37.46 ± 10.63	87.53 ± 1.41	flare in 3FGL
1FLE J1332-0518	321.6	56.0	11.93 ± 3.39	26.22 ± 1.93	flare in 3FGL
1FLE J1503+1033	11.3	54.8	3.60 ± 1.02	6.73 ± 1.19	flare in 3FGL
1FLE J2231+1132	77.1	-38.6	74.32 ± 22.09	29.34 ± 1.03	flare after 3FGL

Table 5.4: *1FLE sources with a flare during the 3FGL observation time (flare in 3FGL) or after the 3FGL observation time (flare after 3FGL).*

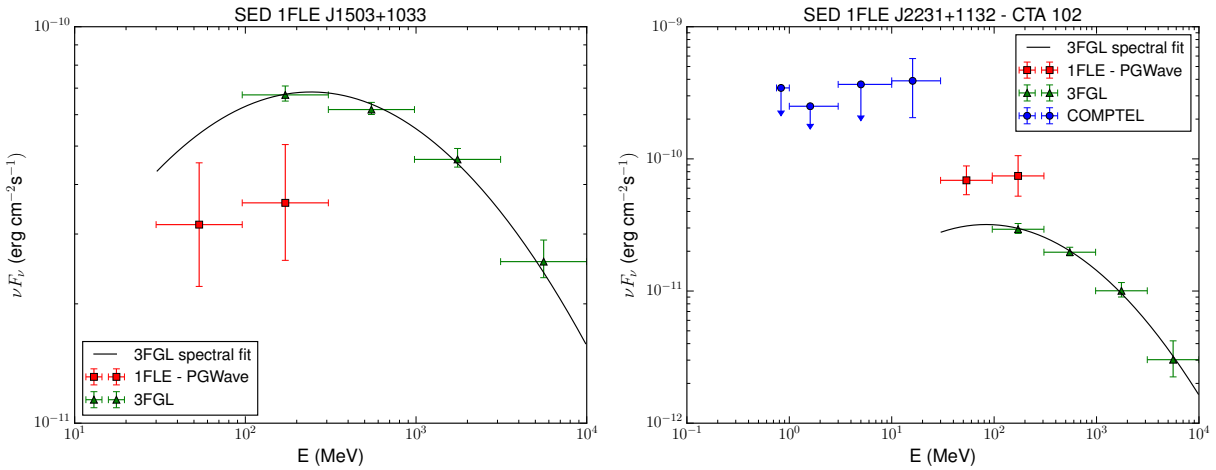

Figure 5.8: *Left: SED of the 1FLE J1503+1033 which had a flare during the 3FGL observation time. Right: SED of 1FLE J2231+1132, also called CTA 102, which had a flare after the 3FGL observation time. In both the cases the 1FLE flux points are consistent with the estimated flux in the FL8Y list. The labels are the same as in Figure 5.7.*

- 15 degrees. The negative tail of the wavelet kernel from the bright source reduces the value of the WT peaks for the nearby sources, which leads to an underestimate of the corresponding fluxes. This is the case of 1FLE J0531+0707, which is in the vicinity of the Crab pulsar, and 1FLE J2254+1617, which has a bright source 1FLE J2231+1132 within 8°.

5.5 Conclusion on 1FLE catalog

In this work, the first 8.7 years of *Fermi*-LAT Pass 8 data were analyzed and, for the first time, a catalog of sources in the energy range 30 – 100 MeV was derived. The 1FLE catalog, described in this thesis, contains 198 sources detected using PGWave, a background-independent wavelet-based method. This catalog closes the gap between the

previous γ-ray catalogs: the COMPTEL observations at energies lower than 30 MeV and the *Fermi*-LAT catalogs at energies higher than 100 MeV. About 94% of the 1FLE sources have associations in the 3FGL *Fermi*-LAT catalog. Among the 11 sources without associations in the 3FGL, five are within $|b| < 10°$where the Galactic diffuse emission has several structures. Among the six sources at high latitude: one source is in a region with a large Galactic emission, two sources are surrounded by 3FGL sources (which are likely to merge in a single source due to large PSF at low energies), and three sources have a significance between 3.5 and 4 σ. The ratio of FSRQs to BL LACs varies from approximately three to one in the 1FLE, to 1 to 1 in the 3FGL and one to six in the 3FHL. The redshift distribution of the BL Lacs in the 1FLE is peaked toward higher redshift relative to the redshift of the 3FGL BL Lacs. This is correlated to the large ratio of low-synchrotron peaked BL Lacs in the 1FLE (58%) relative to the 3LAC (26%). They have softer spectra and higher redshifts than BL Lacs in 3FGL.

Despite the different energy ranges and the more than two times longer time interval of 1FLE relative to 3FGL, all significant 1FLE sources have associations with 3FGL sources and no significant new source have been discovered. This means that there are no sufficiently bright sources with a very soft spectrum, e.g., with a cutoff around 100 MeV: sources of this type would not be detected in the 3FGL.

An instrument with better angular resolution, such as AMEGO (McEnery 2017) or e-ASTROGAM (De Angelis et al. 2017a,c), will improve the sensitivity at energies below 100 MeV and increase the number of sources detected at MeV energies compared to previous γ-ray experiments. In Figure 5.9, the sensitivity of the 1FLE catalog is compared to the PS sensitivities of various γ-ray experiments. At energies below 100 MeV, both AMEGO and e-ASTROGAM are expected to have a sensitivity which is more than two times better than that of *Fermi*-LAT. These new instruments are able to widely extend our knowledge of the MeV sky.

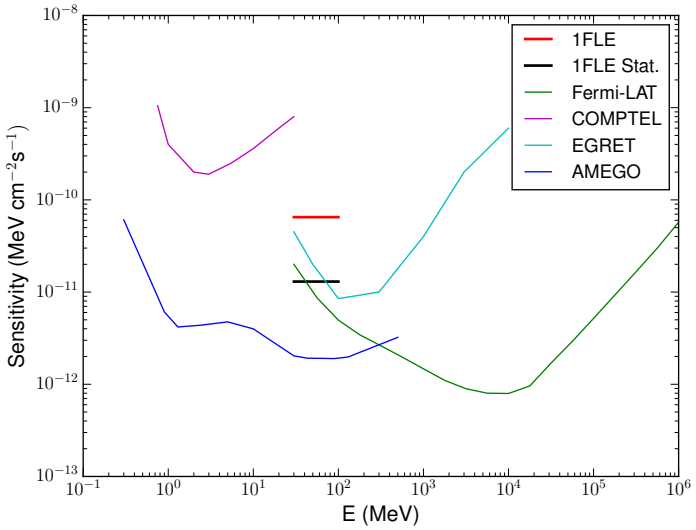

Figure 5.9: *Comparison of the PS sensitivity of the 1FLE catalog and the differential sensitivities of several γ-ray instruments. The COMPTEL (magenta line) and EGRET (cyan line) sensitivities are given for the typical observation time accumulated during the nine years of the CGRO mission. The Fermi-LAT sensitivity (green line) is for a high Galactic latitude source in ten years of observation in survey mode. The blue line represents the simulated continuum sensitivity (3σ, 3 years) for AMEGO. Red line: the 1FLE total sensitivity (see also Figure 4.11), black line: the 1FLE statistical sensitivity determined as the flux corresponding to the 5σ significance of PGWave wavelet transform peak value (Figure 4.15).*

CHAPTER 6

The evolution of the PWN HESS J1825-137 observed with *Fermi*-LAT

This chapter presents the first results of energy-dependent morphology of the Pulsar Wind Nebula (PWN) HESS J1825-137 in the GeV band, obtained using 10 years of data collected by the *Fermi* LAT in the energy range between 1 GeV and 1 TeV. PWNe develop when the particle wind collides with its surroundings, especially the slowly-expanding ejecta of the progenitor supernova, and form a termination shock. Despite the deep observations and studies of several PWNe many open questions still remain; in particular, the mechanism by which the particles are accelerated at the termination shock is not yet understood. The PWN HESS J1825-137 is an archetypal system where it is possible to test and study candidate models for the particle acceleration mechanisms.

This chapter is structured as follows: Section 6.1 contains an introduction about PWN HESS J1825-137 and the previous γ-ray analysis. Section 6.2 describes the *Fermi*-LAT data, the models used for the source and the analysis performed. The spectra and extension results for the PWN HESS J1825-137 are presented in Section 6.3. In Section 6.4, possible particle acceleration mechanisms, which could be constrained from the spectral and extension results, are discussed.

6.1 Introduction on PWN HESS J1825-137

In the last decade the LAT has revolutionized our knowledge of the high-energy sky. Thanks to the discovery and study of several thousands of Galactic and extragalactic sources (Acero et al. 2015), the LAT has contributed to the understanding of particle acceleration in the γ-ray sources. Among them PWN, which can under certain circumstances be resolvable both spatially and spectrally in γ-rays, are very interesting objects to investigate.

The energy of the pulsar is dissipated via magnetized particle winds (consisting of electron/positron pairs). PWNe are developed when the particle wind collides with its

surroundings, especially the slowly expanding supernova ejecta, and form a termination shock. Thanks to their characteristics PWNe could be used to test the hypothesized model of particle acceleration.

Among such objects, HESS J1825-137 is a PWN which surrounds a young and energetic pulsar. The pulsar PSR J1826-1334 (also known as PSR B1823-13) was discovered in 1992 by Clifton et al. (1992). The pulsar has characteristics very similar to the Vela pulsar: it has a spin period of 101.48 ms, a characteristic age of 21 kyr and spin-down period of 2.8 $\times 10^{38}$ erg s^{-1}. Cordes & Lazio (2002) derived from the dispersion measure that the distance of the pulsar is 3.9±0.4 kpc. The first detection of the nebula was done by Finley et al. (1996) using X-ray observations with ROSAT, which observed a compact nebula of ∼20" radius around the pulsar.

The discovery of the energy-dependent morphology of the PWN HESS J1825-137 at TeV energies (Aharonian et al. 2006) provided an important proof that the emission is dominated by 'relic' electrons from the earlier epochs of the nebula in which the pulsar was spinning down more rapidly, therefore releasing more energy into the system. Figure 6.1 shows the H.E.S.S. excess map of the region around HESS J1825-137.

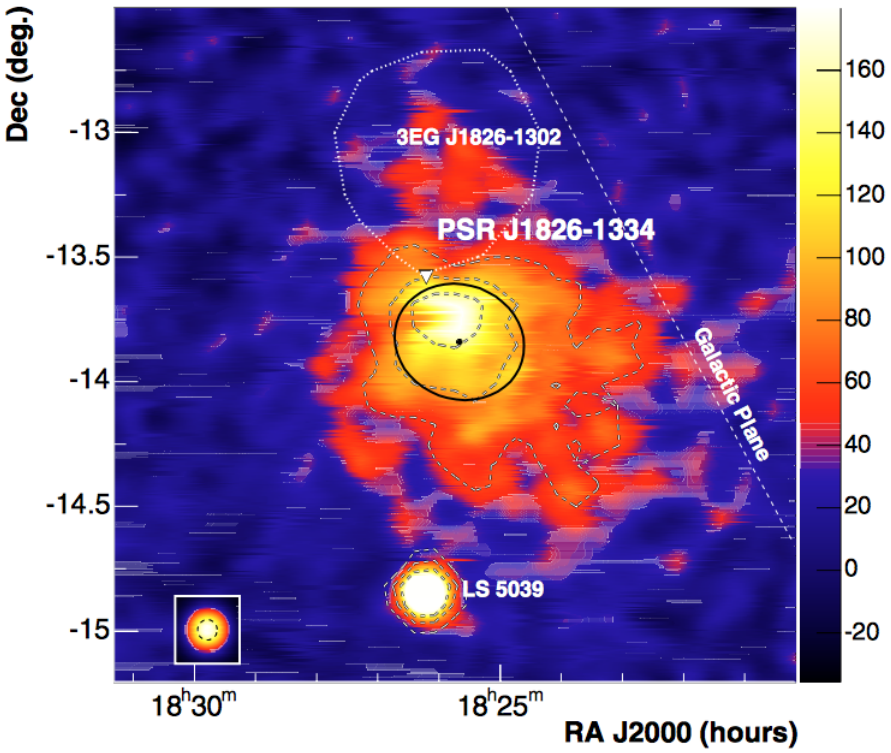

Figure 6.1: *Excess map (smoothing radius 2.5') of the 2.7× 2.7 field of view surrounding HESS J1825-137. The linear color scale is in units of integrated excess counts within the smoothing radius of 2.5'. The excess map is taken from Aharonian et al. (2006).*

In the GeV regime, previous LAT analyses of the pulsar wind nebula HESS J1825-137

has been performed using 20 months of data in the 1 – 100 GeV energy band (Grondin et al. 2011) and, subsequently, 6 years of data in the 10 GeV – 1 TeV energy band (Ackermann et al. 2017b). Taking advantage of the large amount of available *Fermi*-LAT data, an analysis of the energy-dependent morphology and of the spectral parameters of the source is performed in this work using 10 years of LAT data in the energy range between 1 GeV and 1 TeV.

6.2 *Fermi* data analysis

The LAT analysis of HESS J1825-137 is performed using 10 years of Pass 8 Source class events (Atwood et al. 2013) collected between August 4, 2008, and August 3, 2018 (*Fermi* Mission Elapsed Time 239557417 s – 555090221 s) in the energy range between 1 GeV and 1 TeV. The data are taken in a region of interest (ROI) of radius 15°and centered on the PWN position given in (Ackermann et al. 2017b). The maps are created with a pixel size of 0.°1. Gamma-rays with zenith angle larger than 105°are excluded in order to eliminate most of the contamination from secondary gamma rays from the Earth's limb (Abdo et al. 2009b). The P8_Source_V6 instrument response functions (IRFs) are used.

The analysis is performed with Fermipy[1] (Wood et al. 2017), a python package that facilitates analysis of data from the LAT with the *Fermi* Science Tools, of which the version 11-07-00 is used.

In this work, the general characteristics of the source (localization, averaged extension and spectra) are first estimated using the complete energy range between 1 GeV and 1 TeV. The photons have been divided in 18 energy bins (6 per decade) logarithmically distributed. The model used to describe the sky in this ROI includes all point-like and extended LAT sources listed in the FL8Y[2] list, as well as the Galactic diffuse (Ackermann et al. 2017a) and isotropic emission. In the first part the diffuse background, as well all the sources less than 2° away from the center of the source, are left free to vary in the fit. The parameters of all the other sources contained in the ROI are fixed in the fit. In order to correctly estimate the spectra of the PWN, the spectral analysis is estimated twice:

- the parameters of the sources contained included in the model are optimized;
- the spectral analysis is performed for the first time;
- localization and extension analysis are then executed in order to optimize the spatial parameters of HESS J1825-137,
- finally the spectral analysis is performed a second time using the template for the PWN morphology obtained from the localization and extension analysis.

[1] http://fermipy.readthedocs.io/en/latest/
[2] https://fermi.gsfc.nasa.gov/ssc/data/access/lat/fl8y/gll_psc_8year_v5.fit

For the second part of the analysis, namely for the estimation of the energy-dependent extension, the number of bins have been reduced. The photons are grouped into four logarithmically distributed energy bins, in the 1 – 100 GeV energy range, and a single bin in the 100 GeV – 1 TeV energy range. For the analysis of the extension variation with energy, the spectra of HESS J1825-137, as well those of all the other nearby sources, are fixed using the resulting model from the analysis with 6 energy bins per decade. Only the normalization of the diffuse background is fitted again during the analysis energy dependent morphology.

In this work, the Galactic diffuse emissions is modeled using two different templates. For each of them the analysis is repeated in order to study the systematic uncertainty in the results due to the choice of the diffuse model. The first template is the Galactic plus isotropic diffuse emission model derived in Ackermann et al. (2017a). In the second case, for a crosscheck, the standard LAT diffuse emission ring-hybrid model gll_iem_v06.fits (Acero et al. 2016) was used. The residual background and extragalactic radiation are described by a single isotropic component with the spectral shape in the tabulated model iso_P8R2_SOURCE_V6_v06.txt. For the analysis, the first template for the diffuse model is mostly used, unless specified otherwise. In this work the source is modeled using a 2D-Gaussian model for the spatial template and a LogParabola spectral model ($\frac{dN}{dE} = N_0(\frac{E}{E_0})^{-[\alpha+\beta log(E/E_0)]}$).

6.3 The PWN HESS J1825-137

This section presents the results of the spectral and morphological analysis of the PWN HESS J1825-137 using 10 years of *Fermi*-LAT data between 1 GeV and 1 TeV. We also compare the spectral and extension results obtained in this work with those published in H. E. S. S. Collaboration et al. (2018).

6.3.1 Localization and averaged extension analysis

The localization and extension analysis are performed separately in each energy bin, using 2 bins per decade in the 1–100 GeV energy range and using a single bin in the 100 GeV – 1 TeV energy range. Figure 6.2 shows the counts map of the region around the PWN for the energy range between 3 GeV and 1 TeV, because below 3 GeV the source is not significantly detected. In the map the radius obtained for the PWN in this work is compared with the radius obtained in the previous analysis with *Fermi*-LAT data.

Table 6.1 reports the results of the localization and extension analysis performed in the energy range between 1 GeV and 1 TeV using a 2D-Gaussian model as spatial template for the sources. The extension result reported here corresponds to the 68% containment radius: the radius at which the integral of the normalized 2D-Gaussian is equal to 0.68.

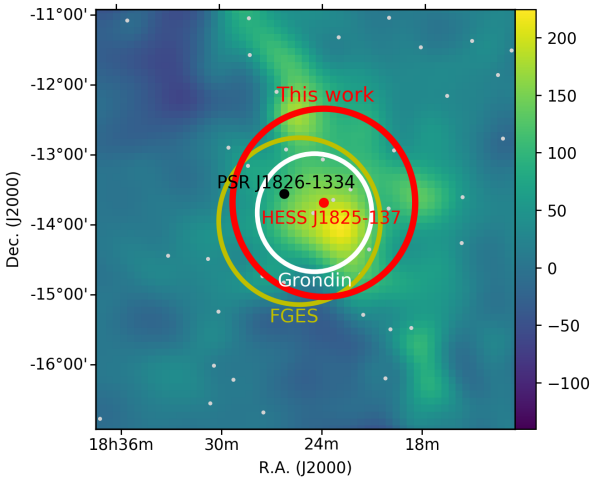

Figure 6.2: *Excess map, in celestial coordinates, of the region around the PWN HESS J1825-137 for the energy range between 3 GeV and 1 TeV. The red circle and point indicate the 2D-Gaussian extension and centroid fit obtained in this work. The green and white circles corresponds to the extension obtained respectively in the FGES catalog (Ackermann et al. 2017b) and in Grondin et al. (2011). The black point indicates the position of PSR J1826-1334, the pulsar which is believed to power the nebula. The FL8Y sources are represented with light grey points.*

The resulting center position of the PWN is shifted by about 0.°58 from PSR J1826-1334, the pulsar associated with the nebula.

Position	Value
RA	$275.°97 \pm 0.°03$
DEC	$-13.°71 \pm 0.°04$
Averaged extension $R_{68\%}$	$1.°35 \pm 0.°09$
Test Statistic (TS)	992

Table 6.1: *Localization and extension results. The results are obtained using 10 years of Fermi-LAT data in the energy range between 1 GeV and 1 TeV.*

6.3.2 Energy-dependent extension analysis with a 2D-Gaussian template

The spectra of HESS J1825-137 and of the nearby sources have been fixed during the analysis of the energy-dependent extension. The normalization of the isotropic plus diffuse components is instead fitted during this analysis.

Before performing the extension analysis, the localization is again optimized inside each energy bin. It is observed a variation of the PWN position between the different bins. Moving from the lowest energy bin, 1–3 GeV, to the highest energy one, 100 GeV – 1 TeV, the position of the PWN moves toward the position of the PSR. The extension analysis is performed by fitting a 2D-Gaussian template in each energy bin.

In the energy band between 1 and 3.16 GeV the source is not completely resolved since the value of the test statistic (TS) is less than 25, which is the threshold value required for a detection in the *Fermi*-LAT collaboration and it corresponds to somewhat more than 4 σ significance. Therefore, for the lowest energy bin, only an upper limit for the extension is reported. This is connected to the drop of the source flux at low energy, as well as the large influence of the diffuse emission in this energy range which does not allow the source to be distinguished from the background. Figure 6.3 presents the source excess maps for each energy bin used in the energy-dependent extension analysis.

Table 6.2 contains the results of the extension measurements performed with the 2D-Gaussian template in 2 bins per decade in the 1–100 GeV energy range and in a single bin for the 100 GeV – 1000 TeV energy range.

Energy range (GeV)	Extension (°)	TS_{ext}	Extension (°)	TS_{ext}	σ_{syst}
	Diff 1	Diff 1	Diff 2	Diff 2	
1 – 3	$< 0.31 \pm 0.05$	4	$< 0.28 \pm 0.09$	1	0.06
3 – 10	1.53 ± 0.11	219	1.68 ± 0.15	139	0.15
10 – 32	1.47 ± 0.11	234	1.45 ± 0.09	218	0.03
32 – 100	1.07 ± 0.07	207	1.06 ± 0.07	213	0.02
100 - 1000	0.75 ± 0.09	129	0.81 ± 0.08	139	0.06

Table 6.2: *Extension measurements as a function of the energy with statistical and systematic errors. The extension analysis is performed using two different diffuse model, respectively 'Diff1' which is the diffuse template optimized for the Galactic plane (Ackermann et al. 2017a) and 'Diff2' which is the LAT standard diffuse model (Acero et al. 2016). The extension is characterized by the 68% containment radius obtained from a 2D-Gaussian fit. In the first energy bin an upper limit is reported since the TS value is less than 25. The systematic error σ_{syst}, due to the diffuse model, has been calculated as* $\sigma_{syst} = \sqrt{(Extension_{diff1} - Extent_{diff2})^2 + (\sigma_{Extension_{diff1}} - \sigma_{Extension_{diff2}})^2}$.

6.3.3 Energy-dependent extension analysis with the radial profile method

For comparison, measurements of the nebula extension have been performed using the same approach as that adopted in H. E. S. S. Collaboration et al. (2018). The extension of the nebula as a function of energy was measured using the radial profile of the emission in

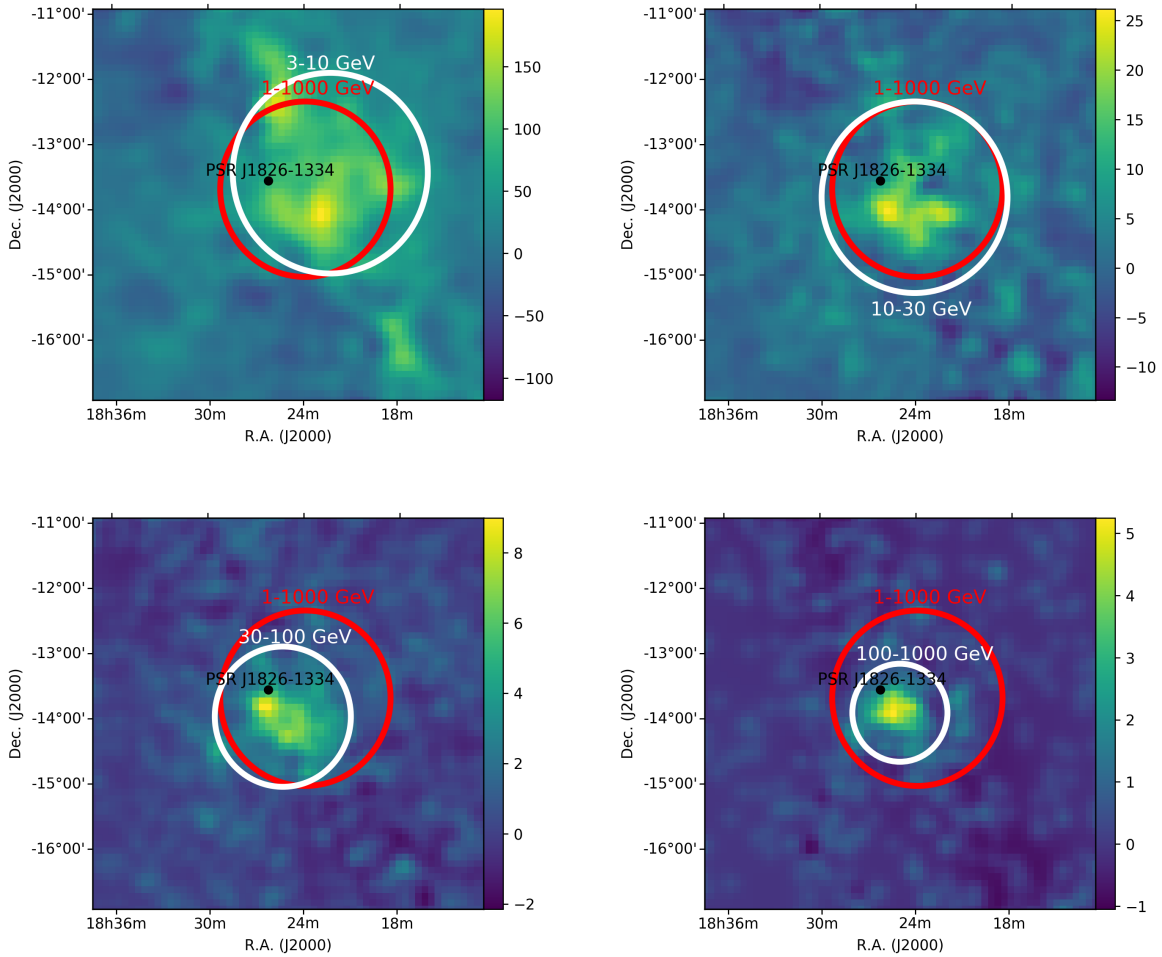

Figure 6.3: *Excess maps, in celestial coordinates, of the region around HESS J1825-137 for the energy ranges: 3–10 GeV (top left), 10-32 GeV (top right), 32–100 GeV (bottom left) and 100 GeV – 1 TeV (bottom right). The energy bin between 1 and 3 GeV is not reported because, in this energy range, the source is not completely resolved (TS<25). The excess maps are smoothed with a Gaussian of radius 0.2. The white solid line represents the extension determined in the single energy bin. For a comparison the resulting extension obtained for the entire energy range (1 GeV – 1 TeV) is plotted with a red line. All the extension corresponds to the 68% containment radius.*

the Southern half of the nebula, taking the position of the pulsar PSR J1826-1334 which powers the system as the central location.

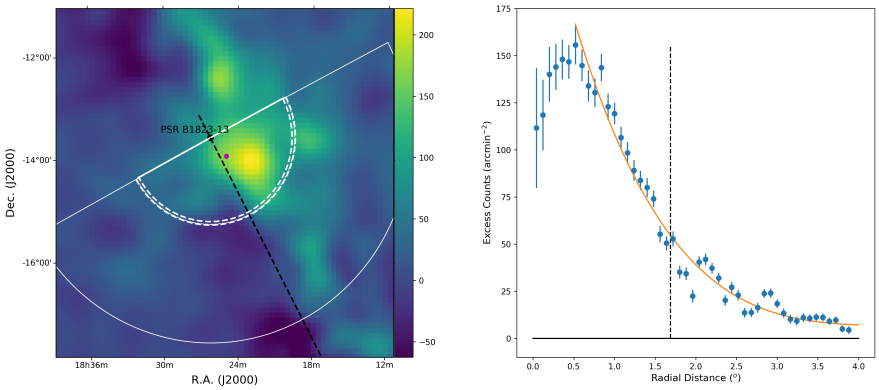

Figure 6.4: *Radial profile of the PWN HESS J1825-137 in the energy range 3-1000 GeV with Fermi-LAT, taken from the same region orientation as used by H.E.S.S. with the position of the pulsar and best-fit Fermi centre of a 2D Gaussian indicated. Because of the no detection of the source in the lowest energy bin, the energy threshold was raised to 3 GeV. The characteristic size of the nebula is indicated in both plots.*

The extension of the emission was estimated by fitting a polynomial to the radial profile, from a minimum radius out to 2.°4, using the formula:

$$y(x) = \begin{cases} a(r - r_0)^n + c & (x < r_0) \\ c & (x \geq r_0) \end{cases} \tag{6.1}$$

such that with increasing r the emission decreases out to a distance r_0 at which it approaches the constant value c. The minimum radius of the fit was chosen to be beyond the emission peak, the position of which, determined by a moving average approach, was found to vary with energy. The parameter a provides the overall normalization, while the fitted value r_0 defines the extension. Since the distance r_0 was found to be highly sensitive to the order of the polynomial n, to mitigate this effect the extension was taken at the radius at which the fitted function dropped to a fixed fraction $(1/e)$ of the peak value (referred as $R_{1/e}$). Additionally, the results of the fit were cross-checked by fitting an exponential function to the radial profiles, and obtaining results compatible with the previous ones.

6.3.4 Comparison of the 2D-Gaussian and radial profile extension estimation

The extension of the PWN in the LAT energy range obtained by Fermipy is given as the 68% containment radius. This is the radius at which the integral of the normalized

2D-Gaussian is equal to 0.68. The 2D-Gaussian is defined, under the assumption to be centered in the origin, as:

$$f(x,y) = \frac{1}{2\pi\sigma^2} e^{-\frac{x^2+y^2}{2\sigma^2}} \ . \tag{6.2}$$

The containment radius corresponds to the radius R^{α}, where the integral of the function from 0 to the radius is equal to α. Consequently, the radius R_{α} can be the defined as

$$R_{\alpha} = \sigma\sqrt{-2log(1-\alpha)}, \tag{6.3}$$

where α in this case equals to 0.68.

In order to compare the two methods it is possible to approximate the polynomial function used for the radial profile analysis as a simple Gaussian without introducing a large bias. In this case, for a single Gaussian, the radius at which the function drops to the ratio $1/e$ of the peak value corresponds to $R_{1/e} = \sqrt{2}\sigma$. Consequently, using the Gaussian approximation for the radial profile, it is possible to compare the *Fermi*-LAT and H.E.S.S. results:

$$R_{1/e} = \sqrt{2}\frac{R_{68\%}}{\sqrt{-2log(1-0.68)}} = 0.9368 R_{68\%} \ . \tag{6.4}$$

The extension results with the radial profile method are estimated from the position of PSR J1826-1334, the energetic pulsar which seems to power the entire system, instead the extension obtained with the 2D-Gaussian template is estimated from the center of PWN. Therefore, for a comparison between the two results, in the following part the energy-dependent extension results from the 2D-Gaussian template are corrected by the offset between the center of the PWN and the position of PSR J1826-1334, which lies approximately along the same line as the axis of the radial profile.

Table 6.3 presents the extension results obtained with the two different methods: 2D-Gaussian template and radial profile analysis. At the 2D-Gaussian extension (Table 6.2) a value corresponding to the offset between the center position of the PWN in each energy bin and the PSR was added.

Energy (GeV)	2D-Gauss Ext. (°)	Radial Prof. Ext. (°)
3 – 10	1.40 ± 0.23	$1.67^{+0.02}_{-0.08}$
10 – 32	1.56 ± 0.16	$1.45^{+0.02}_{-0.06}$
32 – 100	1.48 ± 0.13	$1.11^{+0.07}_{-0.14}$
100 – 1000	1.13 ± 0.14	$0.77^{+0.03}_{-0.06}$

Table 6.3: *Extension measurements as a function of the energy for the 2D-Gaussian template (corrected for corresponding distance along the major axis) and the radial profile method using a polynomial fit.*

6.3.5 *Fermi* - H.E.S.S. energy-dependent extension comparison

Figure 6.5 shows the comparison of the results of the energy-dependent extensions (in $R^{68\%}$) obtained in this work using both the 2D Gaussian fit and radial profile approaches with 10 years of *Fermi*-LAT data between 1 GeV and 1 TeV band and the H.E.S.S. results in the energy range between 100 GeV and 90 TeV (H. E. S. S. Collaboration et al. 2018). The H.E.S.S. results were estimated using the radial profile method described in Section 6.3.3.

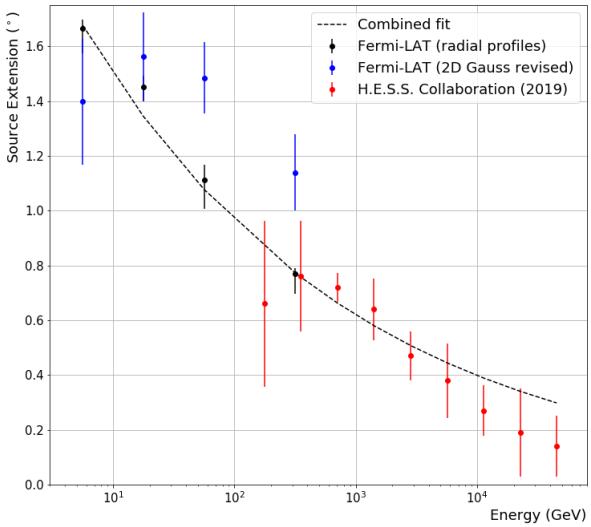

Figure 6.5: *Nebula extension as a function of energy showing results from HESS and this analysis. A combined fit is shown by the dashed line, from 10 GeV to 50 TeV, omitting the lowest energy H.E.S.S. point.*

The results from the 2D-Gaussian, including the offset of the centroid from the pulsar position, tend to be slightly larger than the results obtained from the radial profile fit (see Figure 6.5). A possible explanation is the different treatment of the extension as $R(1/e)$; in the case of the radial profiles, the peak value is obtained from the excess counts independent of the fitted function; however, for the 2D-Gaussian, $R^{68\%}$ relies on the normalization of the fit. If the normalization of the Gaussian underestimates the true peak value in the excess counts, likely due to the smoother curvature of the Gaussian function, then the distance $R(1/e)$ will be accordingly shifted out to larger radii. In any case the difference between the resulting extension obtained with the two different methods is smaller than 35%.

6.3.6 *Fermi*-LAT spectral energy distribution

The LAT data in the energy range between 1 GeV and 1 TeV are used for the analysis of the source spectrum. The photon events are divided in 18 logarithmically distributed energy bins. The diffuse background, as well all the sources less than 2° far away from the center position of the PWN, are also fitted during the spectral analysis.

The spectral analysis distribution (SED) has been fitted with a LogParabola model as well with a Broken Power Law (Broken PL) model in order to better estimate the point where the break appears. The function used for the Broken PL law is

$$\frac{dN}{dE} = N_0 \times \begin{cases} (\frac{E}{E_b})^{-\gamma_1} \; if \; E < E_b \\ (\frac{E}{E_b})^{-\gamma_2} \; otherwise \; . \end{cases} \tag{6.5}$$

The fit results for the LogParabola and Broken PL are reported in the "*Fermi*" column of Table 6.4.

The break is expected to be connected to the variation of the extension of the PWN and, more specifically, to the energy at which the cooling mechanism of the electron starts to dominate.

6.3.7 Combined *Fermi* - H.E.S.S. SED

Figure 6.6 shows the combined SED with the results obtained in this work, using 10 years of *Fermi*-LAT for the 1 GeV – 1 TeV energy band, and the H.E.S.S. results for the 100 GeV – 90 TeV energy band.

The "*Fermi* + H.E.S.S." column of the Table 6.4 contains the resulting spectral information for the PWN HESS J1825-137 using the energy flux derived in this work with *Fermi*-LAT and H.E.S.S. data.

6.4 Interpretation and conclusions

During this work, the dependence of the extension on energy was studied. There are two particle transport mechanisms which could possibly dominate this dependence.

1. *Diffusive processes* could be expected to dominate the particle transport when the pressure within the nebula reaches the pressure of the surrounding ISM. Therefore the particles are no longer strictly confined within the nebula and begin to diffuse into the surrounding medium. If energy-dependent diffusion is the dominating transport mechanism and no cooling losses occur (which could be assumed for young PWNe), then the nebula would be expected to increase in size with energy. This happens,

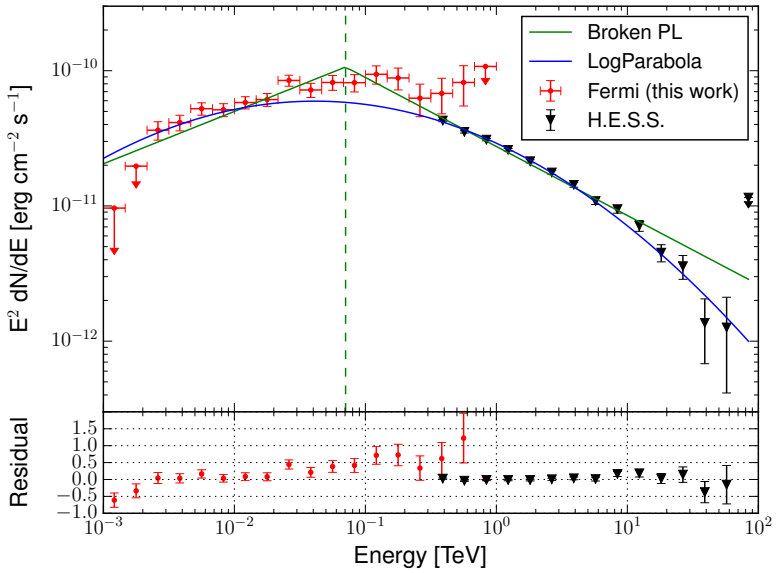

Figure 6.6: *Combined spectra of the PWN HESS J1825-137 with the spectral measurements obtained in this work (red points) using 10 years of Fermi-LAT data from 1 GeV to 1 TeV and the H.E.S.S. results for the 100 GeV – 90 TeV band (black points). The combined SED has been fitted with both a LogParabola (blue line) and a Broken PL (green line). The vertical line corresponds to the energy-break value E_b of the Broken PL. On the bottom the normalized residual between data and the LogParabola are shown.*

under the assumption that all particles were injected at a single instance in time, as a result of the energy dependence of the diffusion coefficient. In the cases where the cooling losses play a role, the nebula extension would decrease towards higher energies becoming more compact. It is expected that the maximum extension of the nebula occur in the γ-ray energy band which corresponds to the energy of the parent particle population at which the cooling time becomes equal to the age of the nebula (Atoyan et al. 1995).

Using the assumption of diffusion and cooling losses it is possible to directly estimate the diffusion index by fitting a power law to the energy extension variation (see Figure 6.5). Assuming that the radial extension R vary with the diffusion coefficient $D(E)$ and that the cooling timescale τ is negligible with respect to the age of the nebula:

$$R = \sqrt{2D(E)\tau} = \sqrt{2D_0 \left(\frac{E_e}{E_{e_0}}\right) \tau}\,, \tag{6.6}$$

where E_e is the electron energy. In case the cooling losses or synchrotron and IC scattering vary with energy as $\tau \propto 1/E_e$, this gives a dependency of the nebula radius on the electron energy as $R \propto E_e^{(\delta-1)/2}$. Considering that the energy of the photons,

LogParabola

Parameter	*Fermi*	*Fermi* + H.E.S.S.
α	2.01 ± 0.72	2.10 ± 0.21
β	0.10 ± 0.02	0.070 ± 0.002
E_0 (GeV)	81.1 ± 184	83.1 ± 150
N_0 ($\times 10^{-11}$ erg cm^{-2} s^{-1})	8.55 ± 2.65	5. ± 1.45
χ^2/ndf	24/14	93/28

Broken PL

Parameter	*Fermi*	*Fermi* + H.E.S.S.
γ_1	1.50 ± 0.06	1.61 ± 0.03
γ_2	2.04 ± 0.05	2.51 ± 0.01
E_b (GeV)	23.7 ± 4.7	70.6 ± 5.7
N_0 ($\times 10^{-11}$ erg cm^{-2} s^{-1})	8.26 ± 0.57	10.65 ± 0.43
χ^2/ndf	33/14	110/28

Table 6.4: *Fit parameters for the SED of HESS J1825-137 with a LogParabola function and with a Broken PL function. The "Fermi" and "Fermi + H.E.S.S." columns contain the fit results obtained with only the Fermi-LAT flux and with both Fermi-LAT and H.E.S.S. fluxes respectively.*

E_γ, produced via IC scattering depends on the electron energy as $E_\gamma \propto E_e^2$ in the Thomson regime, the relation between R and E_γ applicable to energy dependence of the extension is:

$$R = R_0 \left(\frac{E_\gamma}{E_{\gamma_0}} \right)^{(\delta-1)/4}, \tag{6.7}$$

where R_0 is the normalisation radius at $E_0 = 1$ TeV. Therefore the diffusion index could be determined as $\delta = 4\alpha + 1$, where α is the fitted index of the slope of the curve in Figure 6.5 ($R \propto E^\alpha$).

The diffusion index δ is a parameter which varies between 0, energy independent diffusion, and 1, Bohm diffusion. The parameters derived from the fit are given in Table 6.5. The diffusion index δ is compatible with the variation of the spatial extension with photon energy being due to a diffusion dominated particle transport scenario.

Parameter	Value
α	-0.192 ± 0.007
$R_0(^\circ)$	0.62 ± 0.02
δ	0.23 ± 0.03
β	1.61 ± 0.09

Table 6.5: *Derived diffusion and advection parameters under the assumption of Thomson scattering regime.*

2. Bulk particle flow (*advective transport*) could dominate the transport if the particle pressure within the nebula remains greater than the surrounding ISM pressure out to large distances, still with significant confinement. It is possible to find a relation between the nebula radius R and the γ-ray energy E_γ similar to Equation 6.7, if the advection is the dominant particle transport mechanism. Requiring that mass continuity is satisfied and assuming flow density ρ independent from the radius, therefore in case of spherical symmetry, the flow velocity is $v(r) \propto r^{-2}$. Since the flow velocity is expected to vary with the radius r due to the pressure on the nebula from the ISM, it is possible write the relation as:

$$v = v_0 \left(\frac{r}{r_0} \right)^{-\beta} \tag{6.8}$$

where r_0 and v_0 are the initial radius and velocity of the nebula respectively, and β describes the radial dependency needed in order to maintain a constant density profile. The value β can vary from 0, constant velocity expansion, to 2, constant density. Integrating the previous equation up to the cooling time and accounting for the above mentioned dependence of the γ-ray energy on the electron energy in the Thomson regime, the relation between radius and energy in for the advection is:

$$R = R_0 \left(\frac{E_\gamma}{E_{\gamma_0}} \right)^{-\frac{1}{2(1+\beta)}} , \tag{6.9}$$

where R_0 is the normalisation radius at $E_0 = 1$ TeV. Similarly to diffusion case, β can be derived from the power law fit to the energy dependency of the the nebula extension as $\beta = -\frac{1}{2\alpha} - 1$. The derived β, given in Table 6.5, is compatible with an expansion scenario closer to the constant density profile.

In Porth et al. (2016) it is shown that advective processes may dominate in the inner regions of pulsar wind nebulae, although both diffusion and advection are likely to contribute to the overall transport. This variation of extension with energy, shown in Figure 6.5, may be described by a simple power-law relation within the energy range over which the nebula extension is expected to be dominated by particle cooling. This provides an insight into the particle transport processes within the nebula.

The extension of the PWN HESS J1825-137, determined in this work, is larger than in the previous *Fermi* results (Ackermann et al. 2017b; Grondin et al. 2011). The spatial variation with energy observed in this work implies that multiple particle populations with different spectral properties contribute to the detected γ-ray emission. Future observations of HESS J1825-137 with the forthcoming Cherenkov Telescope Array (CTA) will provide a better insight of the source characteristic in order to better understand the particle transport mechanism inside the PWNe. More information about the interpretation and comments on the results can be found in the paper in preparation: Principe et al. (2019).

Part II

Verification of the PDP modules for the CTA-FlashCam camera

Preface

At γ-ray energies of $E_\gamma \geq 30$ MeV, the interactions of photons with normal matter are dominated by electron-positron pair production in the Coulomb field of an atomic nucleus. Therefore cosmic γ-rays can be measured in either gas-filled or solid state satellite detectors above the atmosphere collecting the tracks of the resulting $e^{\pm}$-pairs, or using the Earth's atmosphere itself as detector in observing secondary Cherenkov radiation with ground-based imaging air Cherenkov telescopes (IACT). Satellite detectors, e.g., *Fermi*-LAT, work from $\sim$30 MeV up to some hundreds of GeV, where they become statistics-limited as a result of the limited size of the detector itself. In the Very High Energy range (VHE; $E_\gamma > 100$ GeV) large optical telescopes, the IACTs, are used since they provide a large enough effective area to compensate for the steeply falling particle flux spectra. The IACT particle detection technique take advantage of the fact that cosmic rays and γ- rays induce air showers in the atmosphere, that can be detected by their emitted Cherenkov light. To observe these nanosecond light flashes the camera of an IACT needs a very low exposure time and a fast photodetector signal readout. The IACT camera works essentially as electronic device for photoelectron counting. Therefore the uncertainty assigned to the number of photoelectrons counted in each camera pixel is one of the key performance indicators of the camera. The s.c. "charge resolution" does quantify this performance. The value of the charge resolution is directly connected to the precision in the event energy reconstruction.

Part of the charge resolution of a Cherenkov camera is determined by the performance of the photodetectors and the preamplification of their signals. The development of a high-performance photon collection system is still a subject of study in particular for such photon counting detectors, which needs to work with very short events ($\ll \mu s$) . Future IACT arrays, such as the Cherenkov Telescope array (CTA), will consist of dozens of telescopes, each with several hundreds of pixels. In order to achieve the performance indicated by the CTA requirements, it is necessary to test and verify the all the single components of the telescopes. The photon detector plane (PDP), to be characterized and verified in this work, is a mount for the photomultiplier tubes (PMTs) which provides the control of their voltage as well some preliminary processing of the PMT signal. The PDP is then subdivide in several modules, each of one support 12 PMTs. The PDP modules modules are tested in this work with a specially-made experimental setup in order to verify their performances.

The PDP modules verification in this work is structured as following: the first chapter of this part contains an introduction to CTA, particular attention will be given to the medium-sized telescopes and camera and their requirements. In the second chapter the PDP modules, the ECAP experimental setup and the measurements performed are described. The third chapter contains the explanation of the analysis and the results of the PDP module verification. Finally the fourth chapter contains a summary of the analysis results of the first 86 PDP modules, the definition of the rejection criteria and a comparison of the results with the CTA requirements for the camera of the medium-size telescopes.

CHAPTER 1

The Cherenkov Telescope Array CTA

Very high energy (VHE) cosmic γ-rays, namely photons with energy larger than $\sim$20 GeV, are messengers from galactic and extragalactic objects like supernova remnants, active galactic nuclei, pulsar wind nebulae etc. The observation of such VHE γ-rays is possible either with space-borne satellites like *Fermi* (Atwood et al. 2009) or with ground-based observatories (see Section 1.4 in the first part for a description of the space- and ground-based observation techniques). The existing imaging atmospheric Cherenkov telescopes (IACTs) are MAGIC (Aleksić et al. 2016), H.E.S.S. (Pühlhofer & for the H. E. S. S. collaboration 2018), and VERITAS (Park & VERITAS Collaboration 2015).

The Cherenkov Telescope Array (CTA Actis et al. (2011)) will be the next generation ground-based Cherenkov observatory for VHE gamma rays. The project aims to improve on sensitivity by a factor of ten compared to current experiments and to extend the accessible energy coverage well below 100 GeV and above 100 TeV, current limits for the existing IACTs. The observatory will consist of two locations with several dozens of telescopes with different sizes, from 4 m up to 23 m diameter, and equipped with different types of cameras. Figure 1.1 shows a conceptual layout for the CTA's southern hemisphere site.

In Section 1.1 the mission and the science goals of the CTA project are presented. The main characteristics and the layout of CTA are introduced in Section 1.2, as well as the status of the construction. In order to have the possibility to achieve the science goals of CTA, the CTA observatory provided requirements on all the components of the array (telescope structure, camera, optical system). The requirements for the Cherenkov camera of the medium-sized telescopes, the 12 m diameter telescopes, will be discussed in Section 1.3. These requirements have to be met in the photon detector plane and influenced the selection of the criteria for the rejection of PDP modules that are studied in this work.

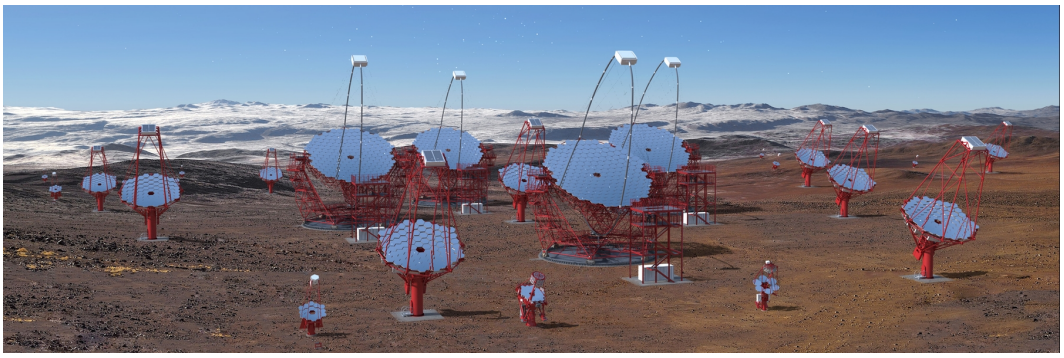

Figure 1.1: *Conceptual layout of a possible Cherenkov Telescope Array (not to scale). The plot is taken from Cherenkov Telescope Array Consortium et al. (2017).*

1.1 CTA mission and science goals

CTA, will be the major global observatory for very high energy γ-ray astronomy over the next decade and beyond. The scientific potential of CTA is extremely broad: from understanding the role of relativistic cosmic particles to the search for dark matter. The CTA collaboration, in a recent publication (Cherenkov Telescope Array Consortium et al. 2017) addressed some of the major questions that they are interested in investigate with the new facility:

- understanding the origin and role of relativistic cosmic particles: what are the sites and mechanisms for cosmic particle acceleration in the Universe? Which role do accelerated particles play in the star formation or galaxy evolution?
- probing extreme environments: what physical processes are at work close to neutron stars and black holes? What are the characteristics of relativistic jets, winds and explosions?
- exploring frontiers in physics: what is the nature of dark matter and how is it distributed? Are quantum gravitational effects on photon propagation?

In order to try to answer those major questions, the CTA is designed to cover a huge range in photon energy, from 20 GeV to 300 TeV, and to improve on all aspects of performance with respect to current instruments. The main motivation for this large energy range is that the lowest energies provide access to the whole universe (avoiding significant gamma-gamma absorption on the extragalactic background light); instead the highest energies are needed to study the extreme accelerators which are known to be present in our Galaxy from direct cosmic-ray measurements. The big improvement in the point-source sensitivity of CTA with respect to current instruments is a consequence of the combination of improved background rejection power, increased collection area and improved angular resolution. Figure 1.2 compares the sensitivity and angular resolution of the CTA arrays to

a selection of existing γ-ray detectors. To allow detailed imaging of a large number of γ-ray sources, the angular resolution of CTA will approach 1 arc-minute at high energies, the best resolution of any instrument operating above the X-ray band. Furthermore, the one to two order-of-magnitude collection area improvement will make CTA a powerful instrument for time-domain astrophysics, three orders of magnitude more sensitive on hour timescales than *Fermi-LAT* at 30 GeV (see Figure 1.2 for a comparison of the sensitivity between CTA and *Fermi*-LAT as a function of the observation time). The observatory will operate arrays on sites in both hemispheres to provide full sky coverage and will hence maximize the potential for the rarest discovery of the phenomena such as very nearby supernovae, gamma-ray bursts or gravitational wave transients.

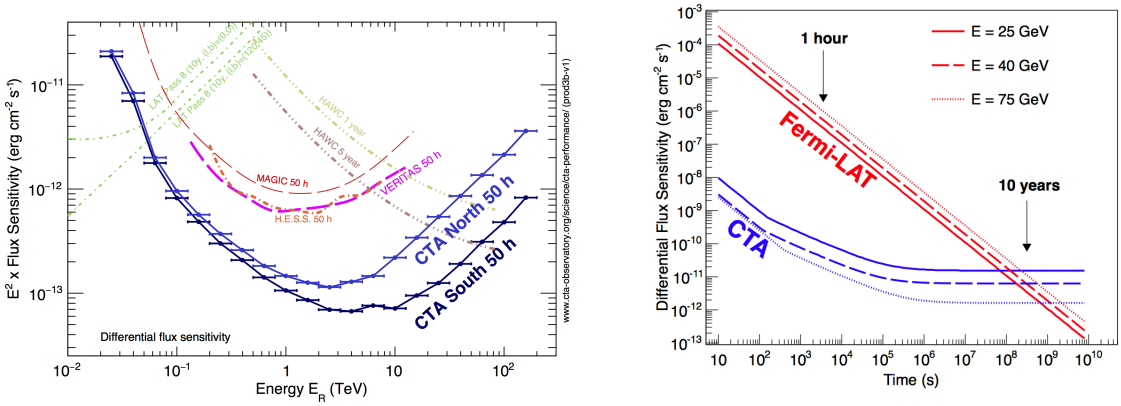

Figure 1.2: *Left: comparisons of the differential energy flux sensitivities for CTA (south and north) for five standard deviation detections in five independent logarithmic bins per decade in energy, with selected existing γ-ray instruments. Right: comparison of the sensitivities of the CTA and Fermi-LAT in the energy range of overlap versus observation timescale. The plots are taken from Cherenkov Telescope Array Consortium et al. (2017).*

1.2 Characteristics and layout of CTA

CTA will consist of the order of 100 telescopes of three sizes installed at two sites: one in the northern and one in the southern hemisphere. It is planned to cover a photon energy range of ∼20 GeV to above 100 TeV. The very wide energy range covered by the southern CTA array necessitates the use of at least three different telescope types referred to as Large, Medium and Small-Sized Telescopes (LSTs, MSTs and SSTs).

Large-sized telescopes (LSTs)

The aim of LSTs (Ambrosi et al. 2013) is to enhance the sensitivity below 200-300 GeV and to lower the effective threshold down to 20-30 GeV. They are designed to cover the energy

range between 20 and 300 GeV. Since Cherenkov showers generated by γ-rays below 300 GeV are frequent but do have small photon intensity, the dish size of this telescopes has to be large. The LSTs will have a standard parabolic 1-mirror reflector with a diameter of 23 m and a local length of 28 m. The ability to rapidly respond to external alerts, and to rapidly issue its own alerts, is built into the CTA design. In particular the LSTs, where the energy range covered provides access to essentially the whole Universe, are optimized for rapid movement, with a goal slewing time of 20 s (minimum requirement 50 s) to anywhere in the observable sky. The construction of the first LST, at the Roque de los Muchachos Observatory on La Palma, started at the end of 2017. It is expected to start preliminary observations during 2019.

Medium-sized telescopes (MSTs)

The MSTs (Pühlhofer 2017) will be the CTA's keystone, with sensitivity in the core energy range of CTA, from about 150 GeV to 5 TeV. The structure of the telescope is made of steel to ensure sufficient stiffness of the optical support structure under all elevation angles. The MST's optic is based on an improved Davies-Cotton design (Bretz & Ribordy 2013). The mirror will be tesselated and will consist of 86 hexagonally-shaped mirrors, with 1.2 m flat-to-flat diameter. The radius of curvature of the dish is equal to 19.2 m, while the focal length is 16 m. Figure 1.3 shows the structure for the MST telescope.

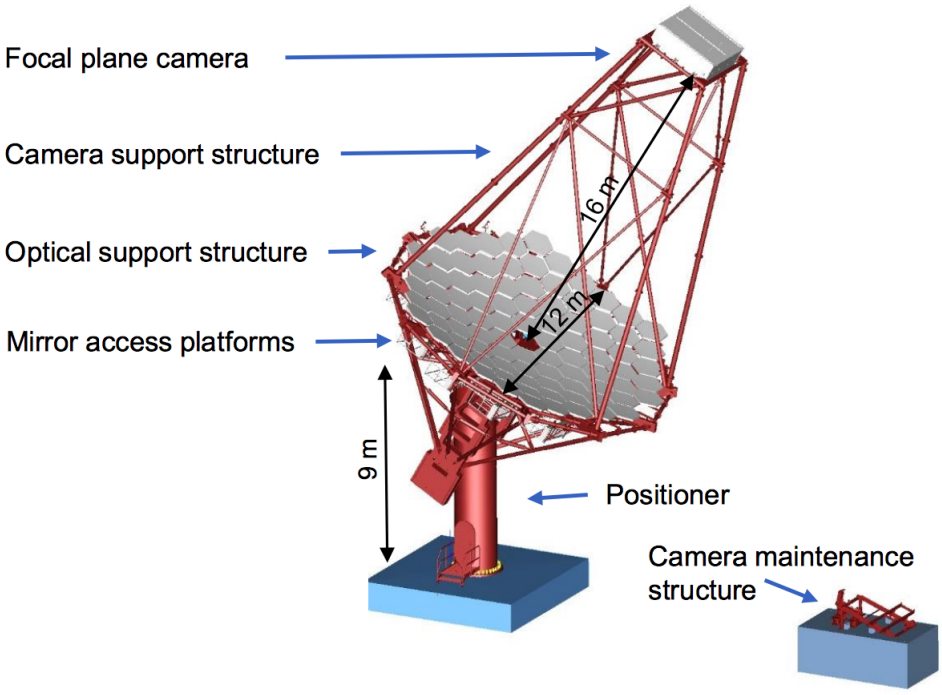

Figure 1.3: *Design of the MST structure. Figure taken from Werner et al. (2017).*

An MST prototype was built in Berlin/Zeuthen in 2012 and is currently undergoing

performance testing. The main purpose of the prototype is to test the design of the individual components and to define the assembly process of the product. The MST cameras will have a large field of view of about 8 degrees, which allow the observation of γ-ray sources that may be concentrated in one area of the sky or widely spread apart. Two different cameras are in development for the MST: the NectarCam and the Flashcam cameras.

NectarCAM The design of the NectarCAM (Glicenstein & Shayduk 2017) is centered on the Nectar analog pipeline readout chip. It is composed of 265 individual modules, each of them is composed of seven photo-detectors (photomultipliers, PMT) with their associated readout and local trigger electronics. The signal coming from the PMTs will be sampled at a speeds of 0.5 - 2 GHz. In case of an event trigger, sampling is stopped and the signal is digitized and sent by the front-end electronics to a camera server. The pixel signal is sampled with two channels, a low-gain and a high-gain channel, in order to provide the full dynamic range (0.5 – 2000 p.e.), as required from the CTA consortium. The dead-time will be <3% at 4.5 kHz event rate for a full MST camera.

FlashCAM It has been developed by the Universities of Heidelberg, Erlangen, Tübingen, Zürich and Innsbruck. The FlashCAM camera has a hexagonal structure with 50 mm pixel spacing and is composed of 147 PDP modules with 12 PMTs each. Figure 1.4 displays a photo of the assembled camera and an exploded view of its components. The design of the FlashCAM camera (Pühlhofer et al. 2012) is based on an horizontal architecture, with the photon detector plane (PDP), the readout electronics (ROS), and the data acquisition system (DAQ) as key building blocks (see Figure 2.3).

A PDP module controls 12 PMTs. An on-board high voltage (h.v.) generator provides h.v. for the PMTs. The h.v. can be adjusted for each PMT individually. This and other slow control functions are accessible via CAN bus. A PDP module contains pre-amplifiers. It makes use of a non-linear amplification scheme, in which signal amplitudes >250 photoelectrons (p.e.) saturate in a controlled way (with the integral growing logarithmically with input charge) in order to extend the dynamic range up to >3000 p.e. while keeping linearity and sub-p.e. resolution for small signals. The analogue signals are transmitted via cat. 6 shielded twisted-pair cables to the readout electronics. The readout electronics design is founded on a fully digital approach with continuous signal digitisation. The signals are sampled with 12-bit FADCs at a rate of 250 MS s^{-1}. A unique feature of the FlashCAM approach is the spatial separation of the PDP at the camera front from the signal digitization electronics (FADC boards), that for a standard PMT-based camera is kept at the rear side of the camera body. The Field Programmable Gate Arrays (FPGAs) buffer and process the sampled signal in a configurable way to derive a trigger decision which is typically develop for localised, short light pulses. Waveforms are read out via a camera-internal, high performance Ethernet network, using off-the-shelf switches and a standard commercial server. The location of the camera server is the central computing cluster and

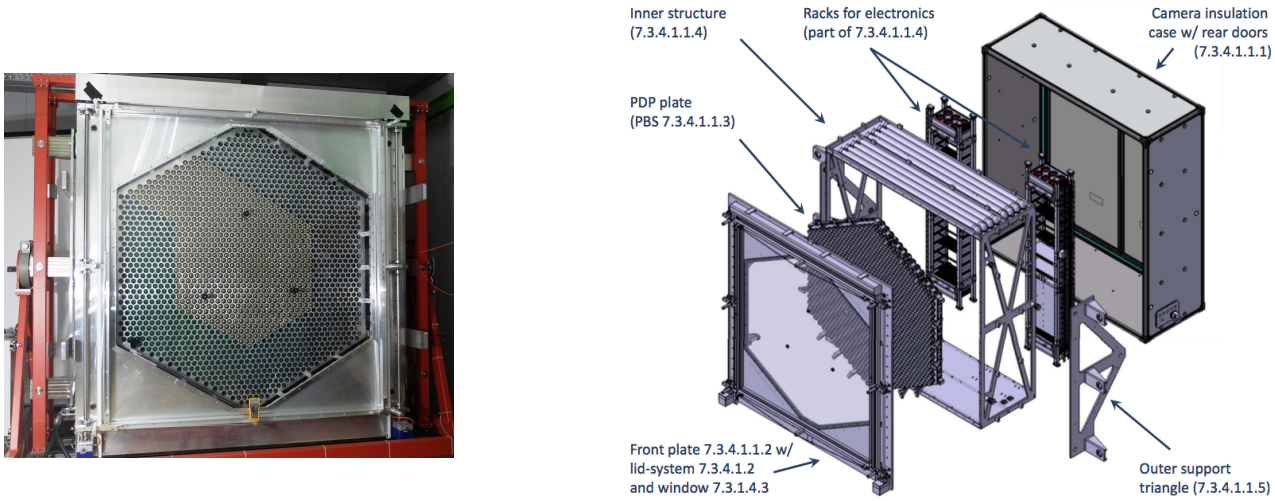

Figure 1.4: *Left: FlashCAM prototype camera for MST with opened shutter. Part of the hexagonal photon detector plane is equipped with PMTs, the rest with dummy heating modules. Right: exploded view of the FlashCAM camera. The plots are taken from Werner et al. (2017).*

it is connected directly to the camera via up to four 10 Gbit Ethernet fibres. Custom-developed software controls the high performance front-end to back-end data transfer as well as event building, optional zero-suppression, event selection, exchange of array trigger information, and data formatting for the array-wide data acquisition. Two additional Gbit Ethernet fibres to the camera are used for slow control and monitoring. Interfaces to the CTA-wide array control, data acquisition, and to the software-based array trigger are also provided by the camera server.

Small-sized telescopes (SSTs)

The highest energy range, above a few TeV, is the domain of the SSTs. Events with such energy are very rare due to steeply falling energy spectra of the sources, at the same time the amount of photons of one of these events is very high. Therefore the SSTs are designated to be numerous, but to have only a small collection area. There are different SST implementations but all of them will have a primary reflector diameter of ∼4m. The CTA consortium will decide before the end the year 2018 which of these concept will be used in the final CTA layout. In particular two concepts of SST, GCT (Brown et al. 2016) and ASTRI (Maccarone 2017) utilize a new dual-mirror design, the Schwarzschild-Couder (Meagher 2014). The third one will use an improved version of the conventional Davis-Cotton design (Bretz & Ribordy 2013).

CTA layout

Since the Cherenkov cascades are so rare (one γ-ray photon per m^2 per year from a bright source or one per m^2 per century from a faint source), the CTA observatory will consist of more than 100 telescopes spread between two array sites in the northern and southern hemispheres to improve the chance of capturing them. The final layout of the positioning of all the telescopes is not decided yet, one possible realization is presented in Figure 1.5. The southern hemisphere array will span the entire energy range of CTA, covering γ-ray energies from 20 GeV to 300 TeV, instead the northern hemisphere array will be more limited in size and will focus on CTA's low- and mid-energy ranges from 20 GeV to 20 TeV. The reason of this choice is connected to the different science goals of the arrays. The southern array will observe the central part of the Galaxy in order to investigate a possible PeV energy accelerators in the Galactic plane. The northern array will focus more to extragalactic sources, which photons are affected by γ-ray absorption on the extragalactic background light.

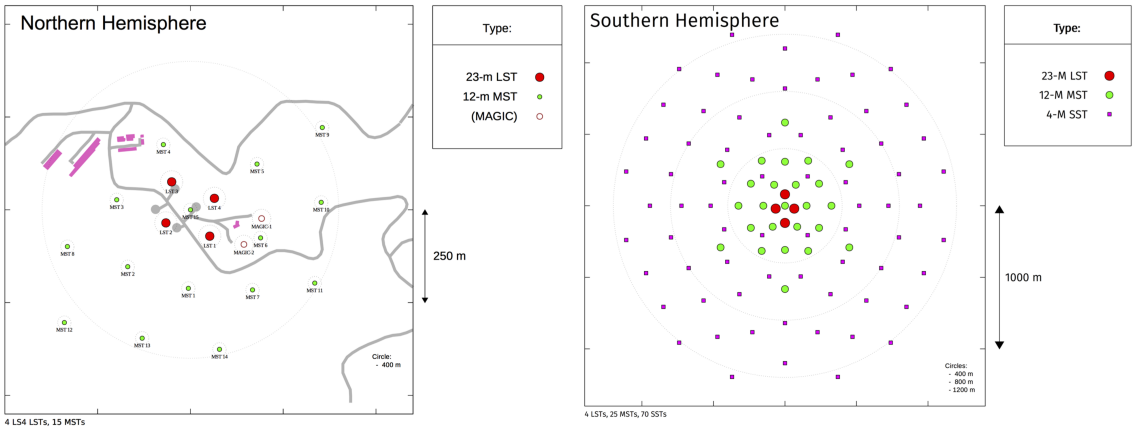

Figure 1.5: *Proposed layouts of the northern and southern hemisphere arrays for CTA. Plot taken from Cherenkov Telescope Array Consortium et al. (2017)*

1.3 Requirements for the MST camera and verification of the components

The Cherenkov cameras for MST telescopes, as well all the other components, will be given as in-kind contributions from the CTA consortium to the CTA observatory (CTAO). Therefore the task of the CTAO is to define performance requirements for the telescopes and their cameras. The requirements are formulated in such way that the science goals for CTA can be achieved. The requirements that are here discussed were defined by internnaly by the CTA collaboration (Collaboration 2013).

Focusing on the MST cameras, are presented the requirements, given by the CTAO, for the upper limit of the charge resolution. The charge resolution quantifies the charge reconstruction performance of a readout system and shall be analyzed for the full detector chain. The CTA requirement for the fractional charge resolution of a MST Cherenkov camera is shown in Figure 1.6.

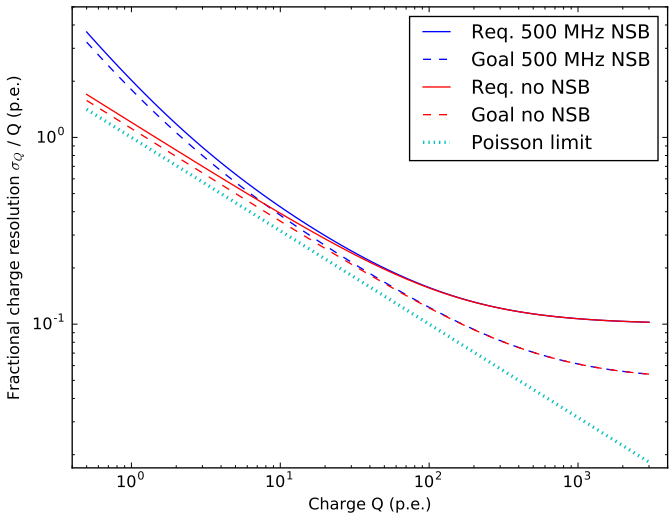

Figure 1.6: *Requirement and goal for the charge resolution of the PMTs in the CTA medium–sized telescope. The blue line is for the case of 5 MHz NSB light, instead the red one is derived for the ideal case of no NSB light. The dotted line represents the Poisson limit. The requirements are taken from Collaboration (2013)*

During the construction phase of CTA, it will be also important to test all the components to assure their correct functionality and to reduce possibly problematic features. All the components that will be used to build the telescopes will be tested separately, as well also in the assembled final stage, in order to verify that the designed characteristics and the CTA requirements are met. A big effort will be the test of all the components of the telescopes, because it will be not so easy (or even not possible) to repair and to re-calibrate all the defects or damages direct in site and this will bring to large costs for the shipping of the material. The implementation of an experimental setup for the verification of the PDP modules for the FlashCAM camera will be discussed in detail in the following chapters.

CHAPTER 2

The PDP modules and the ECAP experimental setup for their verification

One of the main building blocks for the event reconstruction with the FlashCAM camera is based on the Photon Detector Plane (PDP). The PDP is made of modules which are a stack of printed circuits boards on which the PMTs are soldered to.

The ECAP[1] is part of a group of Universities and institutes, spread among Germany, Switzerland and Austria, that contributes to develop and test the FlashCam camera (Puehlhofer et al. 2015). The task of this work is to verify the performance of the PDP modules with the goal of implementing an automated pipeline for the mass test of the modules during the construction phase of the CTA telescopes.

The main components connected to the PDP modules are photomultipliers tubes (PMTs). An introduction on the PMT functionality is given in Section 2.1. The electronics and functioning of the PDP module are described in Section 2.2. Section 2.3 presents the experimental setup used at ECAP for the verification of the PDP modules' performance. An overview of the measurements performed in this work is discussed in Section 2.4.

2.1 General information on photomultiplier tubes

The use of photomultiplier tubes (PMTs) is the traditional method to detect faint light even on a single photon level. Figure 2.1 shows the scheme of a PMT: it consists of an evacuated glass housing containing a photo cathode, several dynodes and an anode.

The PMT makes use of the photoelectric effect to convert the light in an electric signal. When an incident photon strikes the photo cathode, it releases an electron that is then accelerated via an electric field and multiplied exponentially by secondary emission at

[1] the Erlangen Center for Astroparticle Physics, Friedrich Alexander Universität Erlangen-Nürnberg

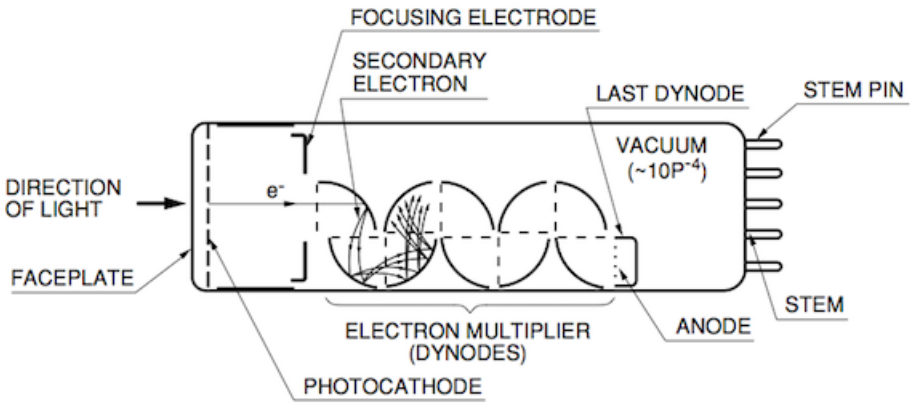

Figure 2.1: *Schematic of a photomultiplier tube. The figure is taken from the website https://labrigger.com/2011/10/17/photon-counting-addendum.*

the dynodes. When the electrons reach the anode, the cascade has thus amplified the initial photo-electron to a measurable current in the milliampere range (usual gain about $10^4 \div 10^6$).

An acceleration voltage of typically about 1000 V is applied to the tube in order to create an electric field for the electron multiplier chain. The voltage is then divided among the dynodes by a network of resistors. The probability of an incoming photon to release an electron via the photoelectric effect is called quantum efficiency, it depends mostly on the cathode material and is usually in the order of 30%. The geometry of the electric field as well as its intensity and the number of dynodes define the gain G of the PMT. The number of electrons at the anode N_A is given by the simple relation $N_A = N_{PE} \times G$ where the N_{PE} is the number of photoelectrons that reaches the first dynode.

2.1.1 The HAMAMATSU PMTs used in the FlashCam camera

The FlashCam group has decided to order the PMTs from the Hamamatsu Photonics K.K.[2] (HAMAMATSU). The requirements for the FlashCam camera brought to the selection of two candidate PMTs, which have been dedicated developed by HAMAMATSU (Toyama et al. 2013). In Mirzoyan et al. (2016) the two types of PMTs have been preliminary tested and it was proven that they both are suited for a scientific application in CTA cameras. The R12992-100-05 model has 7 amplifying stages and the R11920-100-05 one has 8 amplifying stages. For an easy identification, in the following they will be called as 7 dynode PMTs or 8 dynode PMTs.

Both PMT models have a diameter of 38mm (1.5 inch). They are head-on type and feature a concave-convex borosilicate window and a super-bialkali photocathode, which enhance the quantum efficiency (QE) to values of above 35%. The spectral sensitivity

[2]https://www.hamamatsu.com

ranges from 300 to 600 nm, the collection efficiency lies above 95%. They are designed in order to have a fast time response with transit times below 25 ns with variations in the range of 2 ns. The PMTs can be operated at ambient temperatures reaching from -30 to +50°C.

In this work a large sample of both types was examined in the PDP module measurements. The FlashCam group decided to build the first camera prototype using a mixture of both types to further evaluate their individual performances. An additional version of PDP was also designed for both PMT types with a voltage between the photocathode and the first dynode of 300 V, where the initial designed version had 350 V. During the measurements performed in this work, it was decided to use the PMTs of type R12992-100-05 with 7 dynodes for future FlashCam cameras. Chapter 4.1 presents the results of the measurements of the different PMT types.

2.2 PDP modules

A PDP module (see Figure 2.2) is an assemblage of two main printed circuit boards: a high-voltage generator board and a PMT interface board. For the PDP module, 12 pixel mounts were developed. The hexagonal shape of the PDP module naturally leads to three sectors, each sector with its corresponding readout electronics forms a kind of self-contained unit. The PMTs are soldered into the PMT interface board which contains a voltage divider and an AD8001 preamplifier for each PMT. The analogue signal from the preamplifiers is then sent to the digitizing electronics via one RJ45 connector.

The operations of the PDP module are divided into three parts (Puehlhofer et al. 2015), each being carried out by a separate board:

- the control part (Figure 2.2 right rear of the printed circuit board) hosts a microcontroller and the controller area network (CAN) bus interface for slow control;
- the analogue part (front PCB including the PMTs) comprises the high voltage (HV) regulation and distribution for the PMTs, preamplifiers, current and voltage measurement circuits;
- the HV generation realized on a small piggyback, hosts two custom developed Royer type HV generators for -500 V and -1.5 kV.

The interface to the readout electronics is realized with three RJ45 connectors for the differential transmission of the analogue signals of four pixels per connector. The output signals of the PDP-module preamplifiers are sent over differential transmission to the flash analog to digital converter (FADC) boards. Four channels are transmitted over one standard Ethernet Cat5 cable. All required voltages are generated on-board with high efficiency DC-DC converters supplied by 24 V. As a result the total power consumption of

a single PDP module is 2.3 W. The low power consumption allows a passive cooling of the modules by simple convection inside the camera housing (consumption of 147 modules for a 1764 pixel camera is about 450 W distributed over an area of about 4 m^2).

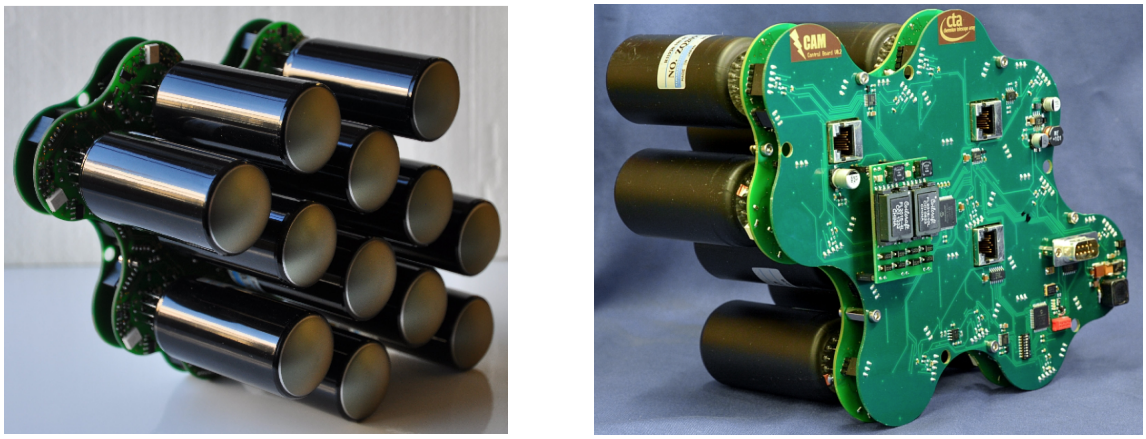

Figure 2.2: *Left: front view of the FlashCam 12-pixel PDP module. PMTs are from Hamamatsu (R11920, the current baseline option for CTA). Right: rear-side view of a PDP module. The Royer high voltage generators are implemented on the small piggyback of the printed circuit board. The three RJ45 connectors are used to transmit the analogue signals of the 12 pixels to the read-out electronics. Power and slow control (CAN-bus) is provided via the DSUB-9 connector. The plots are taken from Puehlhofer et al. (2015)*

The PDP modules are designed to cover a large amplitude range for the signals coming from the PMTs: from less than 1 photoelectron (p.e.) up to several 1000 p.e., with the latter being more rare. The preamplifier used on the PDP module, a current feedback operational amplifier (AD8001), operates in two different modes:

- the linear transfer regime to cover amplitudes up to several 100 p.e. (the threshold is adjustable over the gain and the supply voltage)
- the saturation regime for the higher amplitudes (during saturation of the amplifier, the PMT pulses are 'transformed' into square-like pulses with areas proportional to the input pulse amplitudes).

The estimation of the amplitude of the events in the saturation regime is permitted by integrating the resulting signals and unfolding them. Unfolding of the signal may be done inside the readout FPGAs or offline.

The readout system

The readout of the PDP modules consists of FPGA (Xilinx Spartan-6) motherboards selectively equipped with functional daughter boards (ADC-, trigger-, or master-trigger-

boards) and installed in mini-crates (half 19" crates). The signals of up to 192 pixels can be digitized by such a mini-crate, equipped with eight motherboards. Each ADC daughter board is equipped with twelve 250 MS/s 12 bit ADCs to work for a single PDP module. The signals are digitized continuously and sent to the motherboard FPGA (see Figure 2.3).

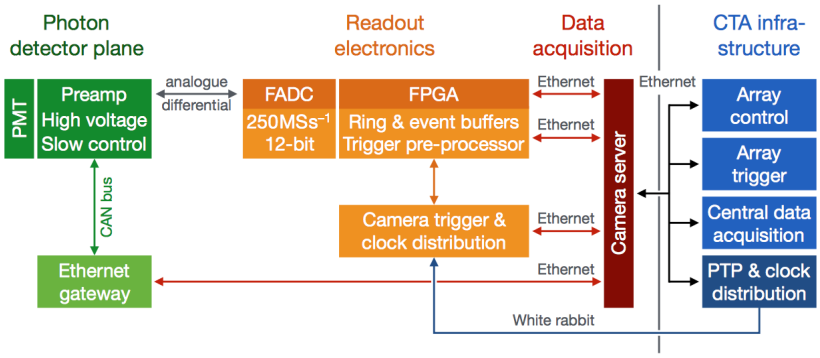

Figure 2.3: *Basic building blocks of the FlashCAM signal chain (left part) and interfaces to the central CTA infrastructure (right part). Figure taken from Werner et al. (2017).*

The data are there stored in ring buffers allowing to send pre and post trigger data to the camera server while new data are stored in parallel ring buffers. The currently implemented ring buffers have a depth of up to 8000 samples, which corresponds to 32μs per pixel. A high-performance raw Ethernet protocol is implemented to handle the large amount of data sent over commercial Ethernet switches from each motherboard to the distant camera server. The camera server can process more than 2 GByte/s with post-processing of the data event-building, which results in a maximum trigger rate of ∼30kHz.

2.3 Experimental setup for the PDP module

A major challenge for any type of possible CTA camera is the engineering-wise clean and solid implementation of the camera electronics. Consequently the FlashCAM team has decided to build and test the major building blocks (PDP modules and mini-crates), to demonstrate the concept on relevant the camera scales and to prepare for mass production, but also to understand in which areas improvement on the engineering level might be needed. The ECAP is responsible for the study and verification of all the PDP modules. The ECAP Flash-Cam team prepared a 36-pixel setup to verify the functionality of the system and interplay between the components, as well as to perform mass tests. In the following, the description of the experimental setup for the PDP-module study and verification is reported. The main components of the PDP-module experimental setup (see Figure 2.4) are:

- Dark box: having a dimension of 2×1×1 m^3 that could host a mount with a group of three PDP modules in order to protect them from the external light and to make

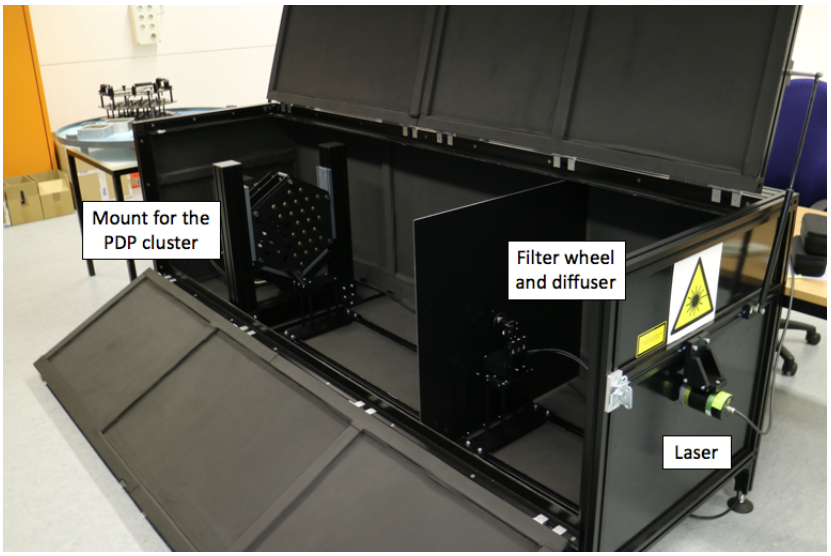

Figure 2.4: *ECAP PDP-module measurement setup. The dark box contains a rail to host the different components: mount for PDP-module cluster, filter wheel, diffuser. Mounted at the front face of the dark box opposite to the location of the PDP-module cluster there is the the Picosecond laser.*

laser-light measurements. The box hosts a rail in order to mount and easily move the different instruments inside the box. It has also doors to allow full access to all components. The box is divided with a panel in two parts in order to avoid illumination noise due to the reflection of the light coming from the laser in the filter wheel. The box has an entry for the laser light and one for the control and data cables. In the box there are contact sensors which check that the box is closed during the measurements.

- Mounts for PDP module and optical components. For the study and verification of the PMTs and PDP modules, a 36 pixel setup (PDP-module cluster) is used.

- Picosecond laser diode (PicoQuant PDL 800-B). It provides a laser pulse of the duration (FWHM) of 55 ns at a wavelength of 404 nm. The laser head is operated at a fixed intensity and frequency setting to ensure a stable intensity of the emitted light. It is mounted at the front face of the dark box opposite to the location of the PDP-module cluster.

- Filter wheel (FW) (Thorlabs NDC-50C-4): it allows the selection of the illumination intensity. It is a circular and reflective neutral density filter of a diameter of 50 mm. The FW has the possibility to automatically rotate and change the reflection ratio with more than 4000 steps with different reflection fraction. A fourth of the steps have no reflection therefore, during the measurements, the FW position was varied only between 1000 and 3450, corresponding respectively to more than 1000

p.e. and ∼0.5 p.e.. Each step corresponds an illumination that, in the case of this experimental setup, decreases when increasing the number of the FW step (high FW positions correspond to low illumination and viceversa). The optical density (OD, see equations below) increases linearly from the start of the coating:

$$OD = log_{10}(\frac{1}{T}), \tag{2.1}$$

where T is the transmission rate.

- Circular diffuser (Thorlabs diffuser ED1-C20-MD). It has a 20° divergence angle with 90% transmission in the range between 380 and 1100 nm.
- DC light LED: it is used to simulate the Night Sky background (NSB).
- Three channels power supply.
- Workstation pc.

2.4 Measurements

PDP modules with two different PMT variants under evaluation, Hamamatsu R12992-100 with 7 dynodes and Hamamatsu R11920-100 with 8 dynodes (Toyama et al. 2013) have been tested in this work. In addition to the two types of PMTs, also the performance of the PDP module with two different voltage values between the photocathode and the first dynode: +300 V and +350 V are evaluated. The readout electronics is connected to a workstation via a commercial Ethernet switch. A light source consisting of a pulsed 404 nm laser, a programmable filter wheel, and a DC UV LED have been used to evaluate the camera at pulsed intensities (0.3–3,000 p.e. per pixel) and DC illumination levels (0–12 GHz p.e. per pixel). In particular the LED is utilized for simulating the night sky background (NSB) illumination. The trigger signal in all the measurements is directly provided by the laser.

The measurements in this work are grouped in three different groups:

- **Without the DC illumination (NSB light)**. This set of measurements is made in order to study the response of the PDP modules in the hypothesis of no background illumination. For these measurements the DC UV LED is switched off and the FW position is varied ($1000 \leq \text{FW} \leq 3450$) in order to vary the illumination between ∼0.5 p.e. and more than 1000 p.e.
- **Fixing the DC illumination (NSB light)**. In this part the response of the PMTs in the hypothesis of fixed background illumination is analyzed. The NSB-current value is fixed to $14{\times}10^{-4}$ A (corresponding to a NSB frequency of 900 MHz) and, as in the case of no NSB light and the FW position is varied ($1000 \leq \text{FW} \leq 3450$, corresponding to an illumination between ∼0.5 p.e. and more than 1000 p.e.).

- **Varying the DC illumination (NSB light)**. The goal of this class of measurements is to study the background and the baseline for the different NSB-current value. The NSB-current value is set to 0 A (corresponding to a NSB-LED frequency of 0 MHz), 5×10^{-4} A (220 MHz), 10×10^{-4} A (590 MHz), 14×10^{-4} A (900 MHz) and 17×10^{-4} A (1200 MHz). The laser is switched off.

For the first two cases, in order to study the response of the pixels for a wide range of illumination, data at about 20 equidistant FW positions (logarithmic spaced illumination) have been taken with a separation of 200 FW steps each. At low illumination, the measurements are taken every 50 FW steps in order to better resolve the single photoelectron (SPE) spectra for a mean number of photons between 0.5 p.e. and 5 p.e. ($2800 \leq$ FW ≤ 3450). A different number of events have been recorded depending on the different illumination regime:

- 50000 events in the *very low illumination regime* ($3050 \leq$ FW ≤ 3450, corresponding to an illumination range between $\sim$0.5 p.e. and $\sim$ 2 p.e.). The reason for this large number is to have a large statistic of events in order to make a precise fit analysis of the SPE spectra.

- 15000 events in the *low illumination regime* ($2800 \leq$ FW ≤ 3000, corresponding to an illumination range between $\sim$2 p.e. and $\sim$ 5 p.e.).

- 10000 events in the *medium and high illumination regime* ($1000 \leq$ FW ≤ 2600, corresponding an illumination range between $\sim$5 p.e. and more than 1000 p.e.).

For each illumination the events have been recorded using a readout window of 128 ns in 4 ns samples. In each sample the signal height is digitized as a multiple of the last significant bit (LSB-value). The FADC continuously evaluates the baseline level, which is stored on a disk together with each trace. A total amount of data, equal to about 10 GByte, are stored at each measurement.

An automatic procedure, implemented in bash and C, has been used to take the data for different illuminations (FW positions) and NSB-current values. The program can automatically configure the FW at the correct position after each set of measurements. Similarly also the NSB-current value is changed for the measurement with NSB light. For each PDP-module cluster (mount for 3 PDP modules) all the measurements (without the NSB light, fixing the NSB light and varying the NSB light) are performed in about 15 minutes.

CHAPTER 3

Analysis description and results of PDP-module verification

The ultimate goal of this work was to develop an automatic pipeline to analyze and check the proper functionality of the PDP modules for measurements where the illumination and the NSB light is varied (see Section 2.4 for a description of the performed measurement).

An important role in the analysis is played by the fit of the single photon-electron (SPE) spectra in order to estimate the correct gain of each PMT. Section 3.1 describes the method used to derive the function for the fit of the SPE spectra. The description of the analysis of the events triggered by the picosecond laser diode is contained in Section 3.2. A summary of the results of the analysis performed in this work is presented in Section 3.3. Particular attention during the investigation of the PDP-module performances is given to the fit of the single photon-electron (SPE) spectrum; the results of this study are reported in Section 3.4.

3.1 A model of the PMT response

Following the argumentation of Bellamy et al. (1994), the function to describe the SPE spectra and its derivation method are presented here. The bases for the calibration of a PMT are the deconvolution of its pulse height spectrum and the extraction of its main parameters. The PMT is usually considered as an instrument consisting of two independent parts:

- the photocathode where the photons are converted in an electric signal (electrons);
- the amplifier (dynode system), which amplifies the initial signal emitted by the photocathode.

Therefore the operation of a PMT can be divided into two independent procedures: photoconversion, including also electron collection, and amplification.

Photoconversion and electron collection

The photon incident on the PMT photocathode produces photoelectrons via the photoelectric effect. In case of real circumstances the number of photons hitting the photocathode is not a constant but it follows the Poisson distribution. This is due to the fact that only a fraction of the incident photons is gathered by the PMT. A random binary process describes the conversion of photons into electrons and their subsequent collection by the dynode system. Therefore the distribution of the number of photoelectrons can be expressed as a convolution of Poisson and binary processes. The probability $P(n, \mu)$ that n photoelectrons will be observed when their averaged number is μ is:

$$P(n, \mu) = \frac{\mu^n e^{-\mu}}{n!} \,. \tag{3.1}$$

The variable, representing the mean number of photoelectrons collected by the first dynode, is defined as $\mu = mq$,where m is the mean number of photons hitting the photocathode and q the quantum efficiency of the photocathode.

Amplification

It is possible to approximate the response of a multiplicative dynode system to a single photoelectron with a Gaussian distribution, when the coefficient of secondary electron emission by the first dynode is large (> 4) and the coefficient of secondary electron collection by the first few dynodes is close to one. The response is therefore described by:

$$G_1(x) = \frac{1}{\sigma_1\sqrt{2\pi}} exp\left(-\frac{(x-q_1)^2}{2\sigma_1^2}\right) \,, \tag{3.2}$$

where x is the variable charge, q_1 is the average charge at the PMT output when one electron is collected by the first dynode and σ_1 is the corresponding standard deviation of the charge distribution. In case of more than one photoelectron that are gathered by the first dynode, the PMT output charge distribution can be derived from Formula 3.2 under the assumption that the amplification processes of the charges initiated by different photoelectrons are mutually independent. In this case the charge distribution when the process is initiated by n photoelectrons, is derived as the convolution of n one-electron cases:

$$G_n(x) = \frac{1}{\sigma_1\sqrt{2\pi n}} exp\left(-\frac{(x-q_n)^2}{2n\sigma_1^2}\right) \,. \tag{3.3}$$

where q_n is the average charge at the PMT output when n electrons are collected by the first dynode. The expression 3.3 is correct in case the chance of a photoelectron missing the first dynode and being captured by one of the subsequent dynodes is negligible.

The response of an ideal (noiseless) PMT can be derived as a simple convolution of the distributions 3.1 and 3.3:

$$S_{ideal}(x) = P(n:\mu) \otimes G_n(x) = \sum_{n=0}^{\infty} \frac{\mu^n e^{-\mu}}{n!} \frac{1}{\sigma_1 \sqrt{2\pi n}} exp\left(-\frac{(x-q_n)^2}{2n\sigma_1^2}\right) . \quad (3.4)$$

Background processes

In addition to the process of conversion of light and amplification of electric charge, various background processes are present in a real PMT which basically generate some additional charge (noise). The background noise can be distinguished in two contributions: a noise signal in the anode circuit that could be generated even in the absence of a light signal and in an additional component of noise generated in the presence of light.

The possible origins of the noise, reported in Bellamy et al. (1994) are: thermoelectron emission from the photocathode and/or the dynode system; leakage current in the PMT anode circuit; electron autoemission by electrodes; photon and ion feed-backs; external and internal radioactivity, etc. Spurious signals of small amplitude can also appear at the PMT output which are due to the incident photon flux. Possible origins of these signals are: photoemission from the focusing electrodes and dynodes, photo-electrons missing the first dynode, etc. It is expected that the amplitude of these signals decreases approximately exponentially.

The resulting spectrum, in the presence of background noise, is a convolution of the ideal PMT spectrum 3.4 with the background charge distribution.

The background processes can be divided into two groups with different distribution functions:

1. the low charge processes (e.g. the leakage current, etc.), which are present in each event and they are responsible for the nonzero width of the signal distribution when no photoelectrons are emitted from the photocathode (pedestal);

2. the discrete processes which can, with nonzero probability, accompany the measured signal (such as thermoemission, noise initiated by the measured light, etc.).

The processes of type I can be described by a Gaussian and those of type II by an exponential function. Calling w the probability that, within these events, a background signal of type II can occur, the background can be parameterize as

$$B(x) = \frac{1-w}{\sigma_0 \sqrt{2\pi}} exp\left(-\frac{x^2}{2\sigma_0^2}\right) + w\,\theta(x)\alpha\, exp(-\alpha x) \quad (3.5)$$

where σ_0 is the standard deviation of the type I background distribution, α is the coefficient of the exponential decrease of type II background and θ is the step function:

$$\theta(x) = \begin{cases} 0 & x < 0 \\ 1 & x \geq 0. \end{cases} \tag{3.6}$$

The first term in Eq. 3.5 describes only the low charge background processes, instead the second term refers to the presence of both groups of background.

The realistic response function of a PMT

Considering the ideal PMT spectrum 3.4 and the background charge distribution 3.5, the realistic PMT spectrum can be derived as the convolution Bellamy et al. (1994):

$$S_{real}(x) = \int S_{ideal}(x')B(x-x')dx' = \sum_{n=0}^{\infty} \frac{\mu^n e^{-\mu}}{n!} \times [(1-w)G_n(x-q_0) + w\, I_{G_n \otimes E}(x-q_0)] \tag{3.7}$$

$$I_{G_n \otimes E}(x-q_0) = \int_{q_0}^{x} G_n(x'-q_0)\alpha\, exp[-\alpha(x-x')]dx' = \frac{\alpha}{2} exp[-\alpha(x-q_n-\alpha\,\sigma_n^2)] \times \left\{ erf\left(\frac{\mid x-q_n-\sigma_n^2 \mid}{\sigma_n\sqrt{2}}\right) + sign(x-q_n-\sigma_n^2\alpha) \times erf\left(\frac{\mid x-q_n-\sigma_n^2\alpha \mid}{\sigma_n\sqrt{2}}\right) \right\} \tag{3.8}$$

where $q_n = q_0 + nq_1$ and $\sigma_n = \sqrt{\sigma_0^2 + n\sigma_1^2}$.

For this, the response function 3.7 of a real PMT contains seven free parameters. Two of them (q_0 and σ_0) define the pedestal. Two others (w and α) describe the discrete background, and the remaining three parameters (q_1, σ_1 and μ) describe the spectrum of the real signal. Of these three parameters, one (μ) is proportional to the intensity of the light source, and two remaining ones (q_1 and σ_1) characterize the amplification process of the PMT dynode system. The absolute PMT gain coefficient is given by the parameter q_1.

A typical spectrum for a PMT signal is presented in Figure 3.1. It corresponds to an average illumination of 1.7 photoelectrons collected from the PMT photocathode.

3.2 Analysis description

The analysis of the data from the PDP modules is mainly subdivided in three steps.

- Pre-Calibration. It checks the working channels and returns for each of them the calibration parameters for the timing (pole-zero correction, raw data time of maximum (ToM), differentiated ToM, upsampled ToM, pole-zero corrected ToM) as well as the

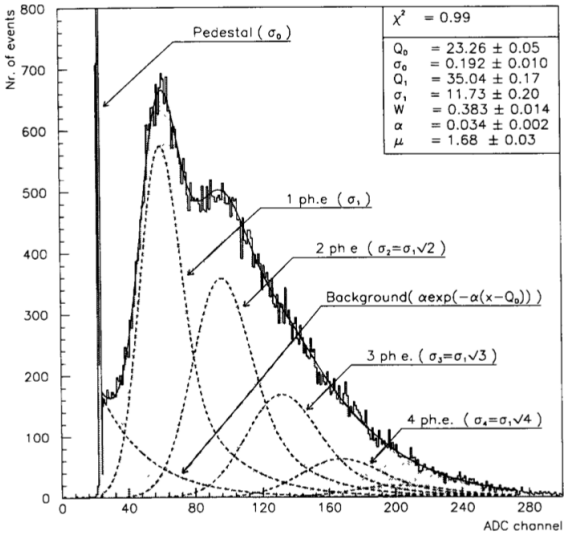

Figure 3.1: *Typical deconvoluted SPE spectra. The solid line corresponds to the PMT response function 3.7, with fitted parameters as given in the plot. The dashed curves represent the background and the partial charge distributions corresponding to n = 1, 2, 3 ... photo-electrons emitted by the photocathode. Figure taken from (Bellamy et al. 1994).*

center of gravity of the trigger event for the reference channels. The pre-calibration is performed only once per PMT for a given batch of measurements (without the NSB light, fixing the NSB light and varying the NSB light). Figure 3.2 shows an example of raw data. The traces are recorded using a readout window of 128 ns in 4 ns bins.

- Trace-analysis. During the trace analysis, after subtracting the baseline value from the respective trace, every trace is upsampled by a factor 4 to reach a nanoseconds sampling. This is done by repeating three times each value and then smoothing the resulting signal using a running mean (see Figure 3.3 for an example of upsampled traces). The pulse response of the PDP-module preamplifier, which acts as a first order low-pass filter, results in an exponential falling edge of the recorded pulses which is then corrected in the analysis. Those pole-zero (pz) corrected values are then used to deconvolve pulses of any amplitude to receive their original pulse shapes. For more information about this method see W. (1997). The reconstruction of the trace is performed for each channel and for all the illuminations (FW positions) and NSB-current values. The Trace-analysis uses as input the raw data and the results of the Pre-calibration. It returns as output, for each channel and each event, the value of the parameters describing the event:
  - baseline (pedestal);
  - integral (also called 'intsum' since the integral is derived as the sum of the all the values in a trace);
  - pole-zero maximum: maximum of the pole-zero corrected trace;

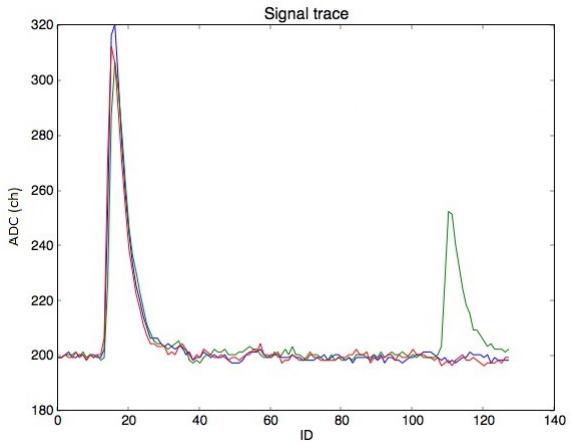

Figure 3.2: *Raw data traces for a fixed channel and three different events in the low illumination regime. The traces are recorded using a readout window of 128 ns in 4 ns and a baseline value of about 200 ADC channels. The plot is made using the data collected with the first prototype camera assembled in Heidelberg.*

  - pole-zero trace, raw-data trace and upsampled trace;
  - time parameters $t0$, $t1$, ToM, which are the time when the event starts, finishes and has a maximum, respectively;
  - the center of gravity and the value at the maximum, for the following cases: raw data, differentiated data, upsampled data and pole-zero corrected data.

- SPE fit. The fit of the SPE spectra is performed for each channel in the low illumination regime ($2800 \leq \mathrm{FW} \leq 3450$). The function implemented by Bellamy et al. (1994) is used for the fit as description of the PMT response, see also Section 3.1. The output values of the fit are basically the pedestal q_0, the gain q_1 the mean number of photons μ and their standard deviations σ_0 and σ_1, as well also the probability w and the exponential index α for the noise signal. The fit is repeated for the different FW positions at low illumination since, at the beginning it is necessary to verify the stability of the fit in the low illumination regime. In the future, the fit analysis is supposed to be performed only for one illumination. Figure 3.4 shows the SPE spectra (on the left) and best fit function (on the right) for a 7-dynode PMT in the low illumination regime (FW=3000).

The tools for the basic steps of the analysis (Pre-Calibration, Trace-analysis and SPE fit) are contained in the FlashCAM library (FClib) which was implemented by the FlashCAM group.

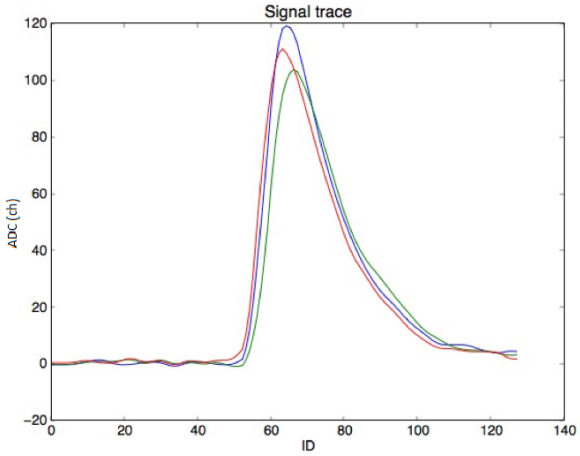

Figure 3.3: *Upsampled traces for a given channel and three different events. A baseline value, of about 200, has been subtracted in the upsampled data. Data collected with the first prototype camera assembled in Heidelberg.*

Absolute calibration

The estimation of the mean number of photons can be directly done in the low illumination regime thanks to the fit analysis on the SPE spectra. This is possible only in the low illumination regime ($\mu < 5$ p.e). Since the fit is strongly dependent on the determination of the pedestal position, moving towrds higher illumination the pedestal peak starts to disappear and the PMT response function (see Section 3.1) does not describe the spectra anymore.

In alternative, the mean number of photons can be derived from the other statistical parameters describing the trace, e.g., pole-zero maximum and the integral value (intsum). They are a good representative of the mean number of photons for medium and high illumination. At large μ a Gaussian with standard deviation $\sqrt{\mu}$ takes over the Poisson distribution that characterizes the low illumination regime. Therefore the mean number of photoelectrons μ can be derived for each pixel using the formula (G. 1990):

$$\mu = \frac{1 + \sigma_{SPE}^2}{\sigma_M^2} \tag{3.9}$$

where $\sigma_{SPE} = \frac{\sigma_1}{q_1}$ is the relative width of the SPE spectra and it is determined with the parameter results of the SPE fit, instead $\sigma_M = \frac{\sigma_i}{mean_i}$ is the relative width of the pulse area distribution of the Gaussian signal. Therefore the mean number of photoelectrons μ is derived from two separate measurements: one for σ_{SPE} and one for σ_M. This method can be used to extend the estimation of the mean number of photons μ also at medium and high illumination $\mu > 5$ p.e.

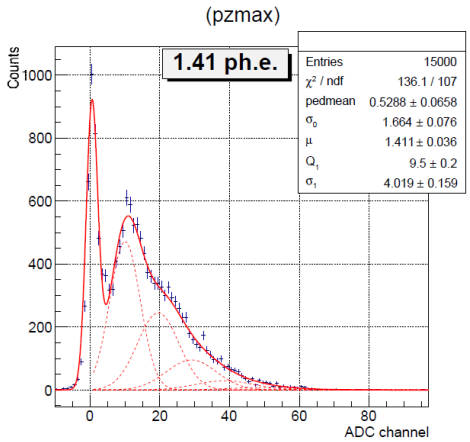

Figure 3.4: *SPE spectra for a 7-dynode channel in the low illumination regime (FW=3000). The solid line represents the best-fit and the dashed lines the derived Gaussian for each photon event.*

In the high illumination regime ($\mu > 100$ p.e.) the pulse reaches the saturation regime. Therefore it is not possible anymore to use the pole-zero maximum for the estimation of the mean number of photons. In order to extend the determination of the mean number of photons toward higher illumination, it is possible to use the intsum parameter since its value is only partially affected by the saturation of the pulse and it still contains information about the mean number of photons. The gain is calculated only for pzmax, since the Formula 3.9 is not valid for intsum. Thanks to the direct proportionality between the pzmax and intsum values, it is possible to use the intsum value to estimate the pzmax using the best fit of their proportionality and to utilize it to reconstruct the pzmax value for illumination with $\mu > 100$ p.e.. Finally the illumination μ is calculated with the Formula 3.9.

Figure 3.5-left shows the distribution of the pole-zero maximum and intsum value varying the illumination (FW position) for a given channel. The plot shows that, around FW position equal to 1600, the pulse starts to saturate and the pole-zero maximum does not increase anymore, instead the intsum value is still increasing proportionally to the number of incident photons.

For this reason, in the pipeline implemented in this work, it was decided to use for the reconstruction of the mean number of photons the pole-zero maximum in the medium illumination regime ($2000 \leq \text{FW} \leq 2800$, corresponding to the illumination range $3 \lesssim \mu \lesssim 200$ p.e.) and the intsum value in the high illumination regime (2000<FW corresponding to an illumination μ >200 p.e.). Figure 3.5-right shows the reconstruction of the mean number of photons using the method described above.

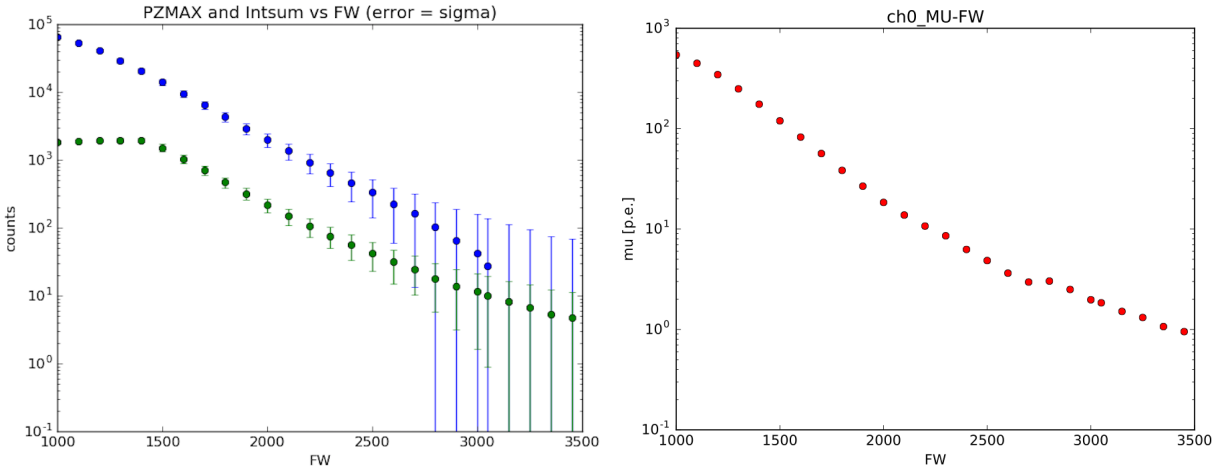

Figure 3.5: *Left: distribution of the pole-zero maximum, green points, and the intsum value, blue points, varying the illumination (FW position) for a given channel. Right: reconstructed mean number of photons for the given channel.*

Automatic insertion of the results into a database

The goal of this work is to create a completely automatic pipeline which

- analyzes the data taken by a measurement of new PDP modules;
- compares them with the previous results of properly working PDP modules;
- automatically inserts the results into a database.

The procedure to automatically insert the results of the new measured modules in a database has been implemented in this work. The database contains all the summarized results of the PDP modules analyzed during the pre series test. Those modules have been analyzed and their correct performance has been verified also inside the first prototype of the FlashCam camera in Heidelberg. The results of the pre-series group of PDP modules (first 86 PDP modules) are used in the ECAP test setup as expected values for the verification of later PDP modules.

Figure 3.6 shows a screen-shot of the database interface. The format of the database allows an easy data management and comparison among the different PMT types, with a real time selection of the data and plot creation.

3.3 The summary analysis

In order to analyze the large amount of data collected during the verification of the PDP-module functionality (more than 3 Gigabyte per PDP module, as described in Section

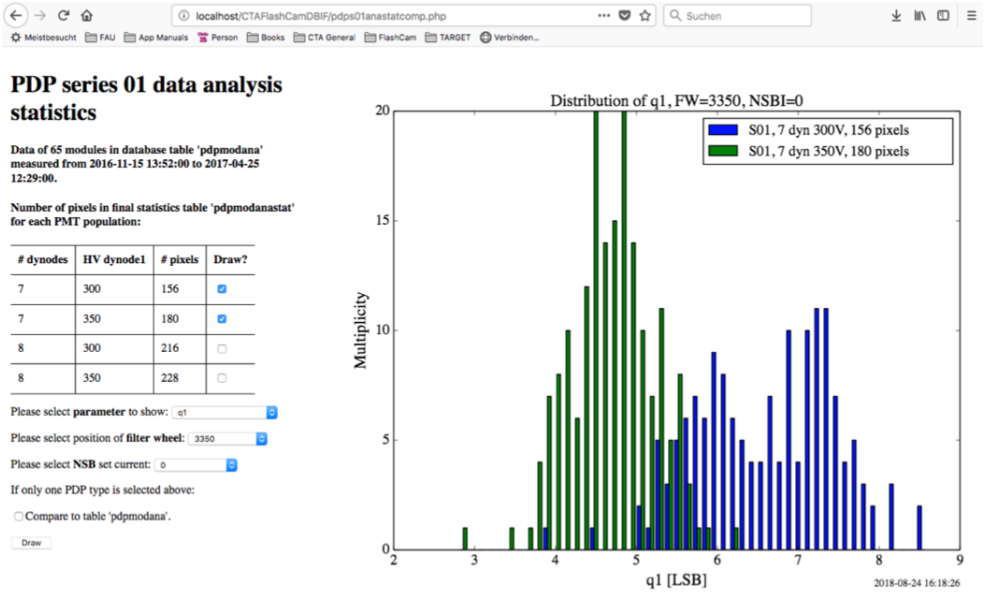

Figure 3.6: *Screen-shot of the database interface. In the plot shown here, the distribution of the gain value* $q1$ *of the 7-dynodes 300V and 7-dynodes 350 V PMTs are compared.*

2.4), an automatic pipeline for the analysis (Runscript) and one for summarizing the main results (Superscript) have been implemented for this work.

Runscript It makes use of some of the tools contained in the FClib in order to make the basic steps of the analysis (pre-calibration, trace-analysis and SPE-fit) and to extract the main information. It performs automatically the analysis of all events for all channels. Data is taken for different illuminations and for the three different types of measurements (without NSB light, fixing the NSB light and varying the NSB light). The NSB light was simulated using a LED with DC illumination.

Superscript It summarizes the essential information from the results of the analysis in order to check the characteristics and proper functionality of each PDP module. It makes a comparison, among all channels, of the results of the SPE fit (in case of low illumination regime), the reconstructed number of photons and the baseline values:

- for a fixed illumination (FW position),
- varying illumination (in case of no NSB light or fixed NSB light),
- varying NSB light (variation of the NSB-LED current).

The detailed steps of the analysis for different illumination scenarios are described in the following sections (Sections 3.3.1, 3.3.2, 3.3.3 and 3.3.4).

3.3.1 Fixed illumination

For each illumination (FW position) it is possible to compare among all the channels the results of the parameters describing the single pulses (pedestal q_0, gain q_1, mean number of photoelectrons μ, polo-zero maximum, intsum) in order to see if there is any particular deviation.

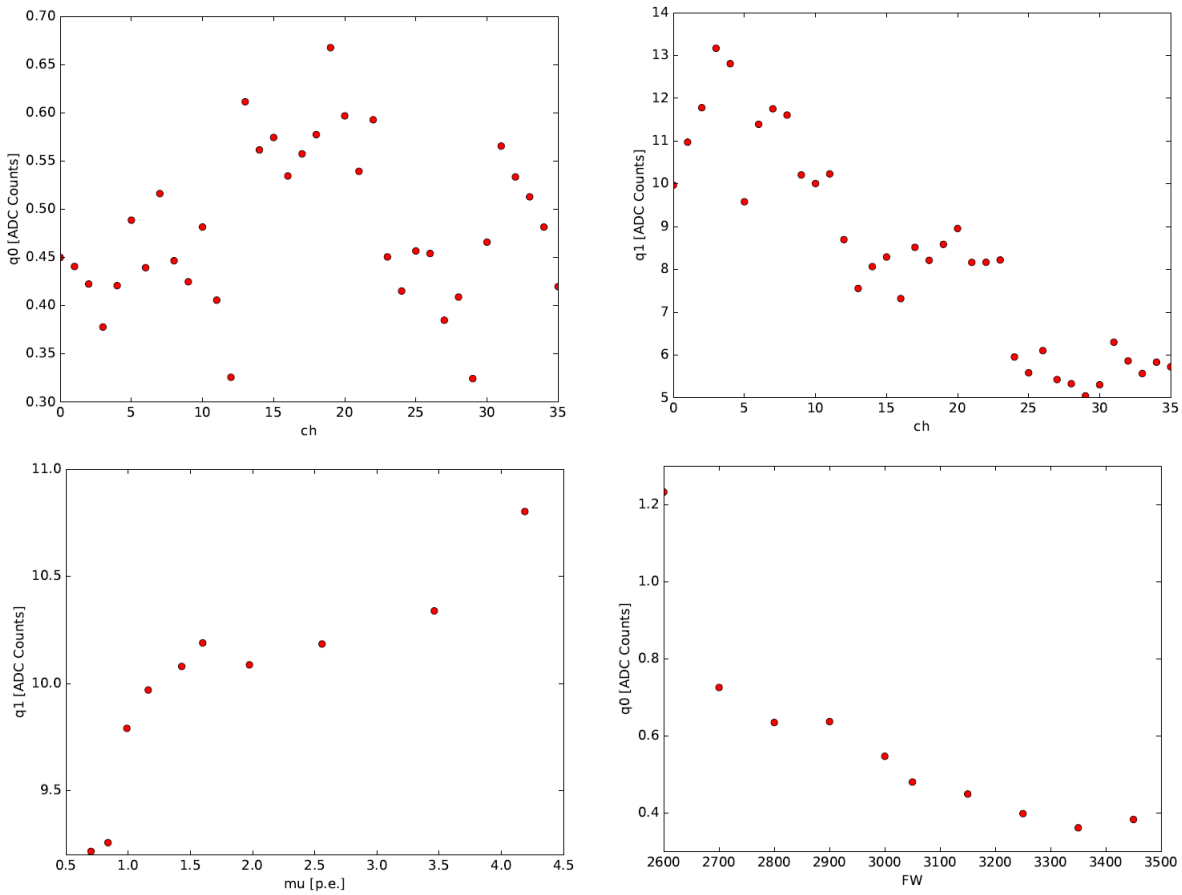

Figure 3.7: *Top: plots of the pedestal q_0 (on the left) and of the gain value q_1 (on the right) for 36 PDP channels measured in the ECAP experimental setup. Channels 0-11 are 7-dynode PMTs and channels 12-35 are 8-dynodes PMTs. The results are obtained for FW=3150. Bottom: distributions of the gain value q_1 (left plot) and the pedestal value q_0 (right plot) for the low illumination regime ($2800 \leq FW \leq 3450$) for one channel.*

The top plots in Figure 3.7 show the values of the pedestal q_0 (on the left) and the gain q_1 (on the right) for the different PMTs in the 36-channels PDP-module cluster. In the right plot it is possible to distinguish the different gain levels between the 7-dynodes PMTs (first 12 channels: 0 – 11) and the 8-dynodes PMTs (remaining channels: 12 – 35).

3.3.2 Varying illumination

In the low illumination regime the SPE fit is performed in order to estimate the main characteristics of each PMT, such as baseline q_0 (pedestal) and gain q_1, that are necessary for a correct determination of the mean number of photons in the medium and high illumination regimes as well also for the case with NSB light. For this purpose it is important to check the stability of the SPE fit at varying number of incoming photons in the low illumination regime. The bottom plots in Figure 3.7 show the resulting gain q_1 (left plot) and pedestal q_0 (right plot) from the SPE fit for different illuminations (FW positions) in the low illumination regime. Below 2 p.e (FW $>$ 3000), it is possible to observe a small variation of the gain and pedestal values varying the illumination. The values are instead more stable above 2 p.e. Therefore, for future measurements, it will be better to perform the SPE fit above 2 p.e. in order to obtain stable results of gain and pedestal.

Reconstruction of the illumination μ

In all the measurements, in order to check if all the PMTs are working correctly, the mean number of photon-electrons is compared among all the channels. The mean number of photons μ is estimated directly by the SPE-fit in the low illumination regime, instead in the medium and high illumination regime the value μ is estimated using respectively the mean value of the pole-zero maximum and of intsum (see Section 3.2). The plots of Figure 3.8 show the comparison of the mean number of photons determined for each single PMT varying the illumination (FW position). Thanks to the clear visualization it is possible to immediately distinguish if a PMT is not correctly working comparing its measured number of photons with the same for the other PMTs.

3.3.3 Fixed NSB light

For the measurements where NSB light is present, it is not possible to perform the SPE-fit. This is due to the fact that the NSB light gives a contribution to the collected photons by the PMTs. Because of this contribution, the baseline is not resolved and it is not possible to estimate the gain. The distribution of pzmax follows a Gaussian distribution. The mean number of reconstructed photons μ is then estimated using the gain value determined in the measurements without NSB light. Figure 3.9 shows, for a comparison, the mean number of photoelectrons reconstructed in the presence of NSB light (plot on the left) and without NSB light (plot on the right). The two measurements are taken with the same PMTs and at the same illuminations (FW positions) the only difference is the presence of the NSB light (LED with current of $14{\times}10^{-4}$ A, corresponding to a NSB frequency of about 900 MHz). In the low illumination regime, a shift toward smaller values ($\mu_{withNSB} < \mu_{withoutNSB}$) is observed between the measurements with and without NSB light. This is connected to the problem of correctly resolving the baseline in the presence of NSB light. In the medium and high illumination regime the estimated number of photons is similar in both cases.

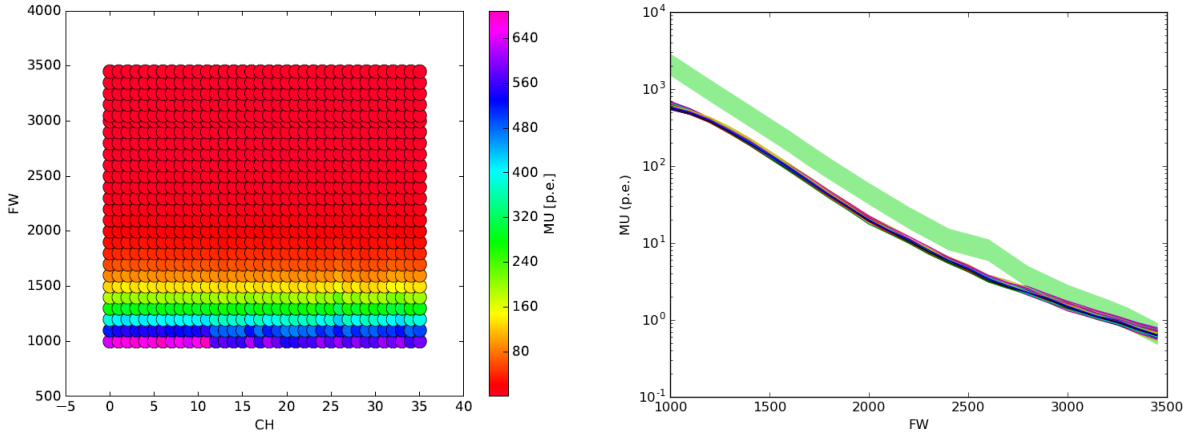

Figure 3.8: *Distribution of the reconstructed mean number of photons varying the illumination ($1000 \leq FW \leq 3450$) for 36 channels contained in the PDP-module cluster (3 PDP modules). Left: 3D plot of measured number of photons (z-axis), for the different channels in a PDP cluster (x-axis) and illuminations (y-axis). Right: mean number of photons (y-axis), varying the illumination (x-axis), of 36 PMTs. Each color line represents the mean number of photons measured by a PMT. The green band is a rough expectation of the mean number of photons measured with a photo-diode. Due to the different method used, and the different position of the instrument inside the dark box, an incompatibility between the two measurements is observed. A new measurement of the expected number of photons is planned for the next year for which it will be used a robot arm and a calibrated PMT to correctly scan the dark box and to provide a precise estimation of the expected number of photons.*

3.3.4 Varying the NSB light

For these measurements the light from the laser is turned off and only the frequency (current) of the NSB is varied. The plots in Figure 3.10 show the variation of the baseline varying the NSB LED frequency. The baseline grows directly proportionally with the NSB frequency.

Correlation in the trace

The measurement where the laser is switched off and the NSB-LED current is set to 0 A has been used to test the noise in all the PMTs contained in the PDP-module cluster. The TraceCorrelator script, inside LibFC librabry, checks for trigger in at least more than one channel if the signal goes above a certain threshold. The TraceCorrelator processes all the events searching for trigger correlations of the electronic noise between the channels. It returns the Pearson correlation value, which is an estimate of the correlation of the electric noise between the channels. The Pearson correlation is a measure of the linear correlation between two variables X and Y, and it is expressed with a value between 0, no correlation,

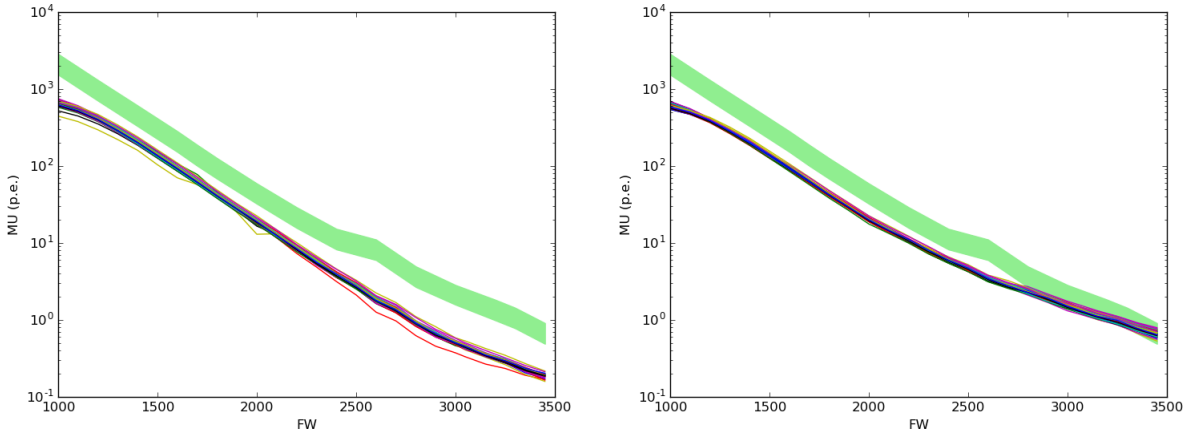

Figure 3.9: *Distribution of the reconstructed mean number of photons (1000 ≤ FW ≤ 3450) for 36 channels in a given measurement run (3 PDP modules), in the presence of NSB light, LED current equals to 14×10^{-4} A (left plot) and without NSB light (right plot). The color lines represent the mean number of photons measured by each PMT. The green band is a rough expectation of the mean number of photons measured with a photo-diode. See caption of Figure 3.8 for more information.*

and 1, perfect correlation.

Figure 3.11 shows the matrix of the correlation. The main diagonal represents the correlation of the PMT signal with itself, instead the different square observed are the correlations of a the channels inside a PDP module (12 PMTs) with the channels inside the other PDP modules (the square along the main diagonal are correlation of the channels inside the same PDP module). It is possible to see in the plot that the correlation of the channels inside the same PDP module is larger than that one for channels in different PDP modules. This is probably due to electric noise in ground of the printed circuit board of each PDP module.

Depending on the different PDP-module version and the different grounding provided, different results of correlation are observed. Inside the plot is also possible to note some pixel lines with larger correlation corresponding to channels that show more noise.

3.4 Study of the PMT response function

In the determination of the performance of a PMT an important role is played by the reconstruction of the mean number of photons for the illuminations with μ >3 p.e. A specific study was performed during this work in order to check the validity of the fit of the PMT response. For that a separate script provided by Oleg Kalekin[1] was used in order

[1]Oleg Kalekin, ECAP, Erlangen Univeristy

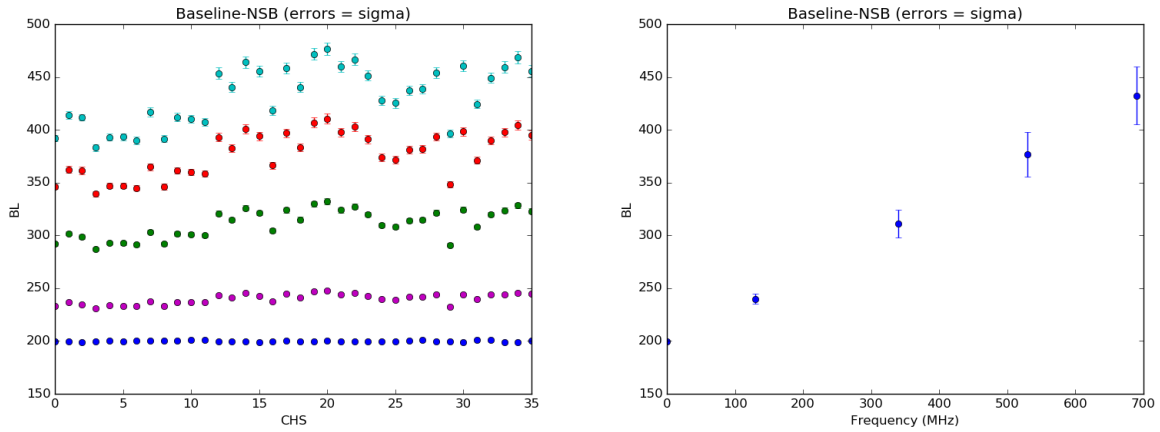

Figure 3.10: *Distributions of the of baseline varying the frequency of the NSB LED. Left: distribution, for each channel, of the baseline values varying the frequency of the NSB LED: 0 MHz (blue), 220 MHz (magenta), 590 MHz (green), 900 MHz (red) and 1200 MHz (light blue). Right: distribution of the mean baseline value averaged on 36 channels for each NSB LED frequency.*

to verify all the possible improvements on the SPE-fit.

The script makes the following steps:

- fit of the pedestal distribution with a Gaussian function and preliminary estimation of the mean number of photons using the Poisson distribution,
- preliminary fit of the signal region using a Gaussian function in order to have a rough estimate of the single photon spectrum parameters,
- fit of the signal region with multi-Gaussian distributed according to the Poisson distribution,
- final fit of the entire PMT response using the response function introduced in 3.1.

Thanks to the different steps, it is possible to make a preliminary estimation of the main parameters (Q_0 and μ) and to perform the fit on the whole spectrum successively. The preliminary estimates of the parameters are then passed as initial values for the final fit of the PMT response function in the whole spectra. This method, thanks to the several steps, allows a more accurate determination of the PMT-response function parameters compared to the FCSPEFit script inside the FClib.

3.4.1 Test on fitting method of the PMT response function

In order to verify and improve the efficiency of the fit on the SPE spectra, several tests on the fit process and the range of the fit parameters have been tried. Figure 3.12 shows the

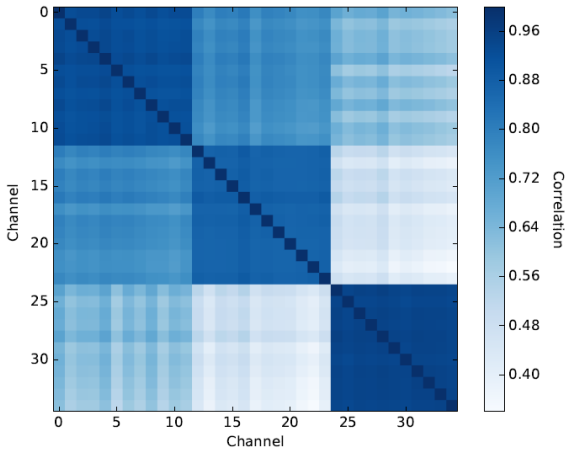

Figure 3.11: *Matrix of the Pearson correlations among the noise signal (NSB-LED frequency equals to 0 MHz) of all the channels in the PDP-module cluster.*

response of a PMT for a signal of about 1.6 p.e. In this case, as well as for all the other measurements, the best fit function for the PMT response (red line in the plot) does not match very well the data (blue histogram). In particular the PMT response function does not describe correctly the single photoelectron peak.

In order to try to reduce this discrepancy and optimize the fit of the PMT response function several trials have been performed :

- varying the lower limit for the entire fit,
- fitting the noise or not,
- fixing the parameters for the pedestal (Q_0 and $sigma_0$) in the final fit,
- varying the upper limit of the preliminary fit of the pedestal.

Despite the several trials preformed it was observed that the response function could not completely describe the data: there is a clear extra signal in the valley between the pedestal and signal region. Besides that, varying the initial parameters of the fit, it is possible to describe the pedestal better but not the photon signal or viceversa. It is not possible with the given PMT response function (see Section 3.1) to simultaneously nicely fit both the pedestal and the photon signal. Therefore it is presumed the presence of a structure between the pedestal and the single photon peak that is not contained in the used PMT response function.

3.4.2 Left tail on the single photon peak

In order to verify the presence of this extra contribution between the pedestal and signal region in the response of the PMT, special measurements were taken using larger statistics

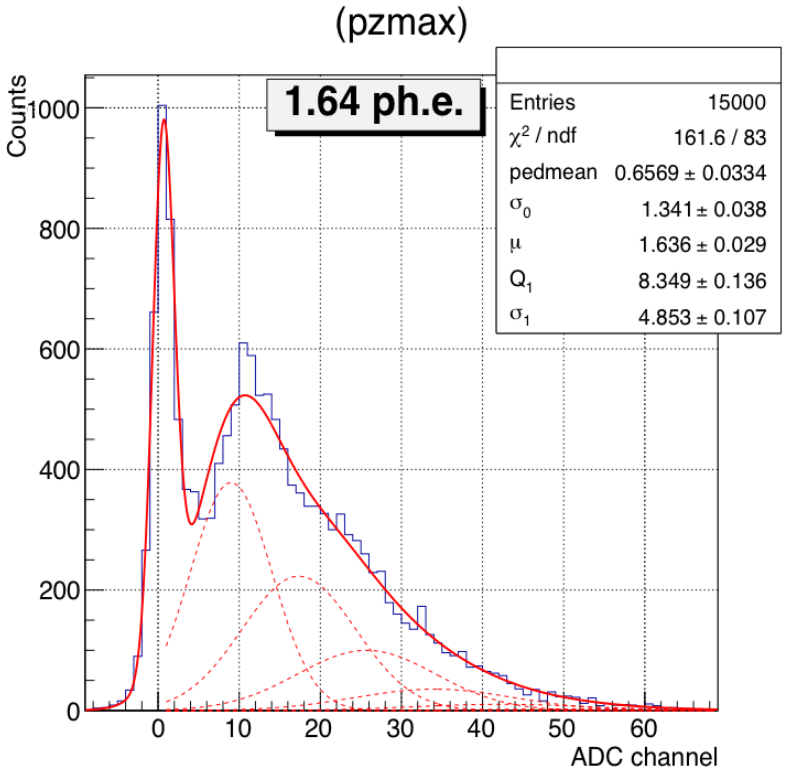

Figure 3.12: *Spectrum distribution (blue line) of a 8 dynodes PMT for an illumination of about 1.6 p.e. The red line represents the best fit of the PMT response. The red dashed lines show the Gaussian distributions connected to 1, 2, 3... photons.*

(500000 events), higher gain (+150 V with respect to the nominal HV value), and fixing the position of the pedestal. The PMT response is first verified using no illumination (laser off) in order to check the characteristic of the pedestal alone.

Figure 3.13 shows the PMT response without illumination, as well as the best fit of the pedestal (Gaussian function) and the residual after the subtraction of the obtained Gaussian to the data.

The Gaussian function describes the PMT response very nice around the maximum but there are some residuals in both the sides that indicate the need of a second Gaussian in order to completely describe the pedestal. After the fit of the pedestal the position has been then fixed in the following fit of the PMT response in the presence of illumination. Thanks to the higher gain used it is possible to increase the space between the pedestal and the signal region in order to better analyze the range among them.

Figure 3.14 shows the plots of the distribution of the PMT response function in the low illumination regime (FW=3450) in the case where the PMT is alimented with its nominal voltage and in the case where it has 150 V more than the nominal voltage. In the plot on the right, thanks to the larger gain due to the higher voltage, it is possible to clearly

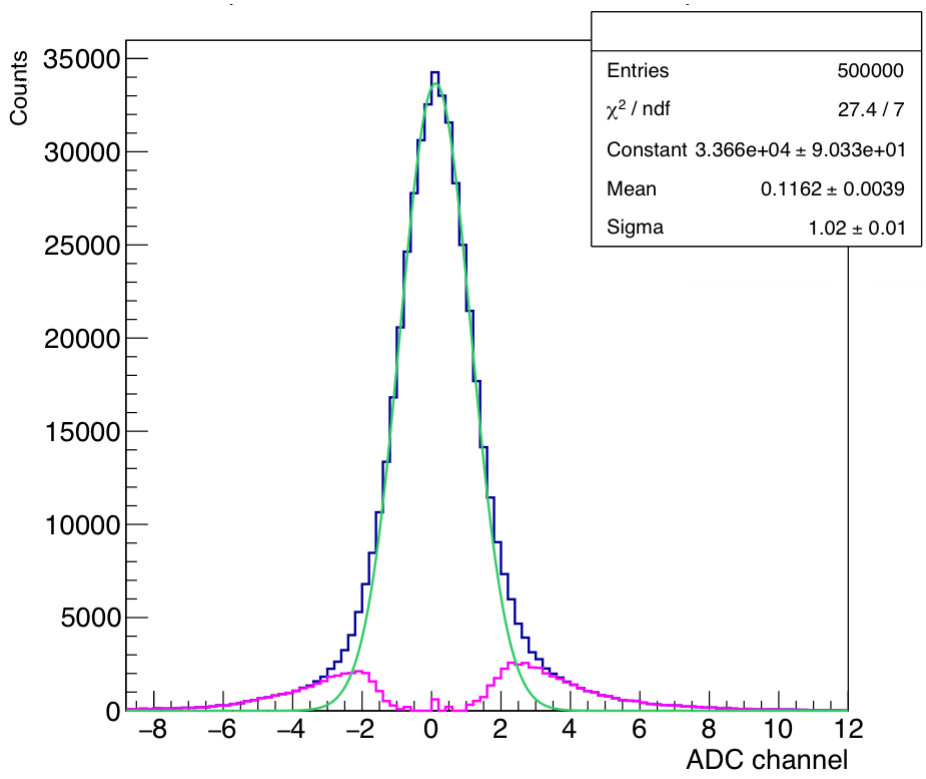

Figure 3.13: *PMT response (blue line) for the case of no illumination. The green line represents the best fit of the pedestal obtained with a single Gaussian (see Section 3.1 for the description of the PMT response function), instead the magenta line indicates the residuals between the pedestal data and the best fit.*

distinguish a structure between the pedestal and signal region that is not described by the response function used so far. This left tail on the single photoelectron peak is possibly due to a backscattering of the photoelectrons at the first dynode that escape from the PMT reducing the number of secondary electrons that reach the second dynode. Namely, when a photoelectron reaches the first dynode, several second electrons are emitted by the dynode. It could happen that not all the electrons emitted by the first dynode reach the second dynode, but some of them could return back to the photocathode and escape from the PMT. This reduces the number of the electrons which reach the anode at the end of the PMT. This phenomenon is called backscattering of the photoelectrons.

A confirmation of the results obtained here comes from the CTA-LAT camera group that in a simultaneous analysis (Takahashi et al. 2018) found similar results in the study of the response of a similar PMT version (1.5 inch PMT HAMAMATSU R11920-100). They found that the single photoelectron peak signal departs from a Poisson distribution at low signal intensities. They motivate this process with a backscattering of the photoelectrons at the first dynode. It reduces the number of secondary electrons that proceed to the second dynode, since some of them may return to the cathode. Consequently, the signal intensity

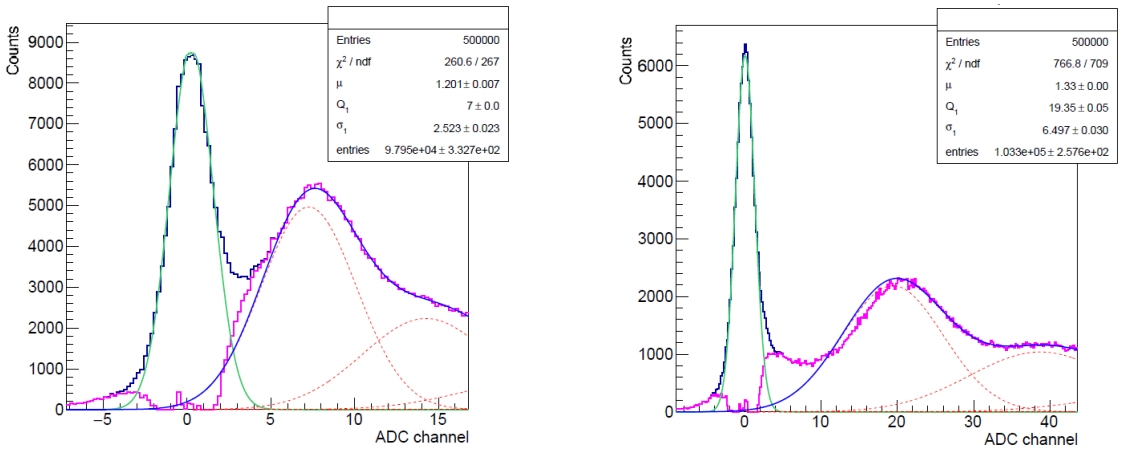

Figure 3.14: *Distribution of the PMT response function in the low illumination regime (FW=3000) in the case where the nominal voltage is supplied to the PMT (left plot) and for a voltage of 150 V above the nominal voltage (right plot). Although the mean number of photons μ is similar in both the cases, the gain Q_1 is larger in the case with a voltage of 150 V above the nominal value ($Q_1 \sim 19$) with respect to the case with nominal voltage ($Q_1 \sim 7$). The green line represents the best fit of the pedestal obtained with a single Gaussian, the magenta line indicates the residuals between the pedestal data and the best fit of the pedestal. The blue curve represents the best fit of the signal region, the red dashed lines show the Gaussian distribution connected to 1,2,3 .. photons.*

of such events decreases. Therefore in Takahashi et al. (2018) an alternative method was used. It estimates the amplification factor and its error from the number of noise events, without first determining the value of single photoelectron peak.

The reason why this effect was not observed before is that it was not possible to resolve with such accuracy the PMT response with the older technology used for processing the signal. The better performance of the new technology allows the possibility to better resolve the PMT response and in particular the region between the pedestal and the signal region. For the future investigation of the PMT response it is planned to add to the classical PMT response function (see Section 3.1) a component for the tail or in alternative to use an indirect way to estimate the position of the single photoelectron peak (q_1).

CHAPTER 4

Conclusions

The goal of this work was the study of the PDP modules for CTA and the creation of a mass test for their verification. In the first part special attention was given to the study of the main parameters which describe the functionality of the PDP modules. Thereafter the analysis was optimized in order to accurately verify the proper operation of the PDP modules. An automatic pipeline to analyze the PDP-module data, summarize the results and insert the data inside the database has been developed in this work.

Between the years 2016 and 2018, 86 PDP modules (corresponding to 1032 PMTs) have been analyzed in the ECAP experimental setup. Section 4.1 presents the summarized results of the analyzed modules. In Section 4.2 the criteria for the rejection of the new PDP modules are discussed. Finally in Section 4.3 the resulting charge resolution of the PDP modules analyzed in this work are compared the CTA MST-camera requirements.

4.1 Summary results of the first 86 PDP modules

Among the 86 PDP modules analyzed in this work, four different implementations of the PMT (Hamamatsu 1.5 inch R12992, with 7 dynodes, and R11920, with 8 dynodes) have been tested:

- 22 PDP modules with 7 dynodes PMT (300 V),
- 22 PDP modules with 7 dynodes PMT (350 V),
- 21 PDP modules with 8 dynodes PMT (300 V),
- 21 PDP modules with 8 dynodes PMT (350 V),

where the different voltages (300 V and 350 V) correspond to the voltage applied between the photocathode and the first dynode, which allows different acceleration of the primary electron. The number of dynodes represents the number of stages where each electron is multiplied in several electrons (secondary emission). The groups of different configurations of number of dynodes in the PMT and the voltage applied between the photocathode and the first dynode are hereafter simply called population of PDP modules. In this section the main results from the different types of PMTs are compared. A comparison between the results of the different populations of PDP modules is performed in order to verify the different characteristics of the PMTs and have enough information in order to help the FlashCam group in making a decision of the PMT type that will be used in the FlashCam cameras for the CTA medium-sized telescopes.

Gain (q_1) and baseline (q_0)

The main parameters that characterize each PMT are the information about the gain (q_1 and σ_1) and the baseline (q_0 and σ_0). Figure 4.1 shows the distributions of the averaged values, among the different version of PMTs, of the gain q_1 and baseline q_0 and their relative averaged sigma σ_1 and σ_1.

The different populations of PDP modules present a similar baseline value but different gain values. As expected, for a fixed voltage, the 8 dynodes population have a larger gain (about 30% larger) with respect to the one with 7 dynodes due to the higher number of electron multiplication stages. A similar difference is found also between the PMT populations, for a fixed number of dynodes, with different voltages between the photocathode and the first dynode. The 300 V PMTs have a larger gain than the 350 V ones. Since the total voltage provided to the PMT is the same in both cases. If a larger voltage is provided between the photocathode and the first dynode then the remaining voltage for all the dynodes is smaller. Therefore due to the smaller voltage provided at each dynode, less secondary electrons are emitted for each primary electron. Consequently the gain is smaller in the case where the voltage between the photocathode and the first dynode is larger. A larger voltage between the photocathode and the first dynode, consequently generating a stronger electric field, is generally applied for increasing the number of primary electrons created in the photocathode that reach the first dynode. This is usually adopted when a good precision for a measurement with low illumination is needed.

In the four populations of PDP modules it is possible to note a tendency: a small increase of the measured gain q_1 when increasing the illumination (reducing the value of the FW position). The variation of the estimated gain q_1 is possibly connected to the extra component, the left tail on the single photoelectron peak, observed in the data (see Section 3.4.2). Due to this extra-component not included in the PMT response function, the gain results to be shifted towards lower values moving to fainter illuminations. This could be explained by the fact that this extra component appears to influence mainly the faint illumination (large FW position) where the number of events (counts) inside the distribution of the single photon peak is fewer than for a bit higher illuminations where

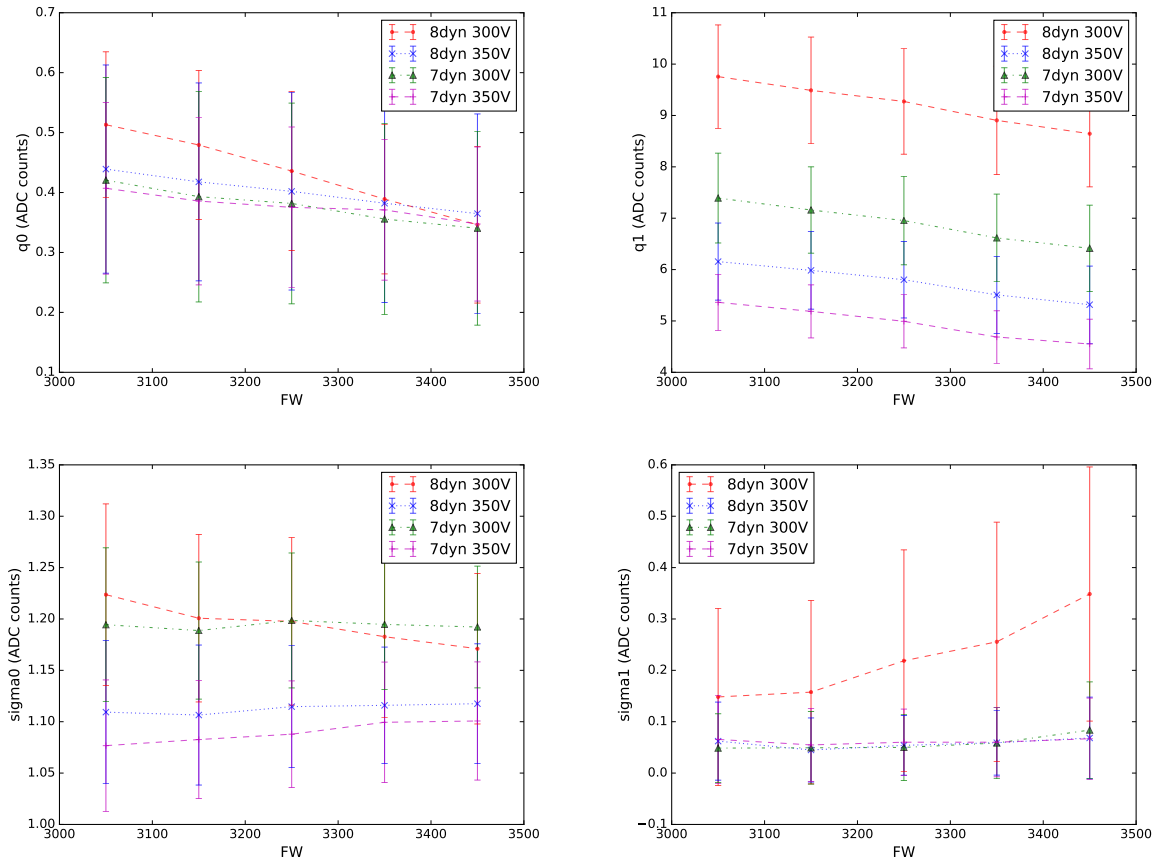

Figure 4.1: *The averaged baseline q_0 (top left plot) and gain q_1 (top right) values and their relative averaged sigmas, sigma0 σ_0 (bottom left) and sigma1 σ_1 (bottom right), for a total of 86 PDP modules of four different populations. The measurements are performed without NSB light and in the low illumination regime ($3050 \leq FW \leq 3450$). See Sections 2.4 and 3.3 for a description of the measurements and the results of the analysis. The error bars represent the standard deviation of the values around the mean.*

the larger number of events provide a minor influence of the tail to the fit of the PMT response.

The sigma value of the gain σ_1, that is an estimate of the dispersion (standard deviation) of the single photoelectron peak, does not present differences between the two 7 dynodes 300 V, 7 dynodes 350 V and 8 dynodes 350 V PMT types. The 8 dynodes 300 V PMTs have σ_1 values larger than in the other populations. This difference could be explained by the observed left tail of the single photoelectron peak. This tail, as presented in Section 3.4.2, could be clearly resolved only in the case of a large gain, because for small values of the gain the pedestal and the single photoelectron peaks is really close to each others and therefore making it difficult to note the presence of the tail. In the case of the PMTs type with 8 dynodes and 300 V, the gain results to be much larger then the other PMT types

and large enough to be more sensitive to the presence of this tail. Since σ_1 is an estimate of the dispersion of the Gaussian distribution of the single photon peak, subsequently the left tail influences this estimate making it larger.

Regarding the baseline values q_0, no special differences among the populations of the PDP modules are observed. Instead for the broadness of the pedestal peak, described by σ_0 the 350 V PMTs present a narrower distribution with respect to the 300 V PMTs. This is connected to the larger number of secondary electrons emitted at each dynode, which dispersion increases with the number of electrons emitted.

Reconstruction of the mean number of photons

The plots of the averaged values (among all the PMTs for each PMT type) of pzamx ($pzmax\_mean$), intsum ($intsum\_mean$) and mean number of reconstructed photons (μ) are shown in Figure 4.2. Despite the different gain values, a good agreement is observed in the values of the mean number of reconstructed photons between the different populations of PDP modules (bottom plots). A good agreement between the results of the different populations of PDP modules is observed also in the case of the fixed NSB illumination (NSB frequency of 900 MHz).

Baseline estimation by varying the NSB light frequency

The baseline changes when varying the NSB light frequency are reported here in order to check the contribution of the noise in the different population of PDP modules. Figure 4.3 shows the distributions of the averaged baseline values (bl_mean) and their relatives averaged errors (bl_var) for each PMT version.

The PMT with 8 dynodes presents an averaged baseline values larger than those with 7 dynodes. This is connected to the higher number of amplification stages of the electric signal in the case of the 8-dynodes PMTs. As a consequence of the larger voltage distributed among the dynodes in the 300 V PMTs with respect to the 350 V ones, the averaged baseline is larger in the 300 V PMTs than the 350 V ones. Increasing the illumination (NSB frequency different from zero) the baseline value increases as well. The dispersion of the baseline σ_0 increases exponentially with the NSB frequency. This dispersion is also influenced by the use of a common LED for simulating the NSB light which does not provide a perfectly stable illumination.

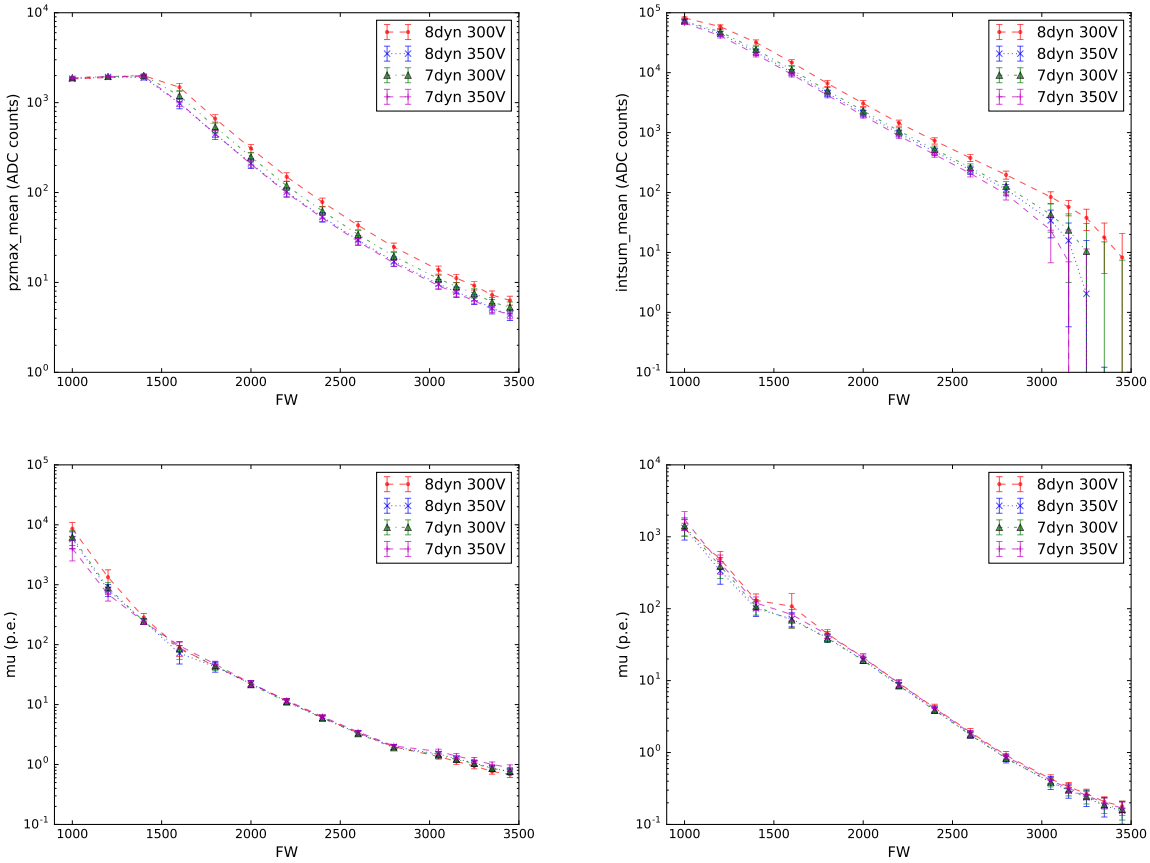

Figure 4.2: *Averaged values of pzmax (top left plot), intsum (top right) and mean number of reconstructed photons μ in case of no NSB light (bottom left) and the same with a fixed (frequency of 900 MHz) NSB light (bottom right) for the different populations of PDP modules. See Sections 2.4 and 3.3 for a description of the measurements and the results of the analysis.*

4.2 Definition of rejection criteria for the PDP module

All the PDP modules that have been tested and considered working well at ECAP, have been shipped and mounted in the assembled FlashCam prototype camera in Heidelberg[1]. All the modules that were correctly working in the ECAP experimental setup did not present so far any anomaly during the test of the FlashCam prototype camera in Heidelberg. This gives a confirmation of the efficient verification analysis performed in this work.

Thanks to the results of the measurements and the experience collected from the verification of the first 86 PDP modules, it will be possible to define some criteria for the rejection of the new PDP modules using the results of the measurements already per-

[1]Max-Planck-Institut für Kernphysik, Heidelberg (Germany)

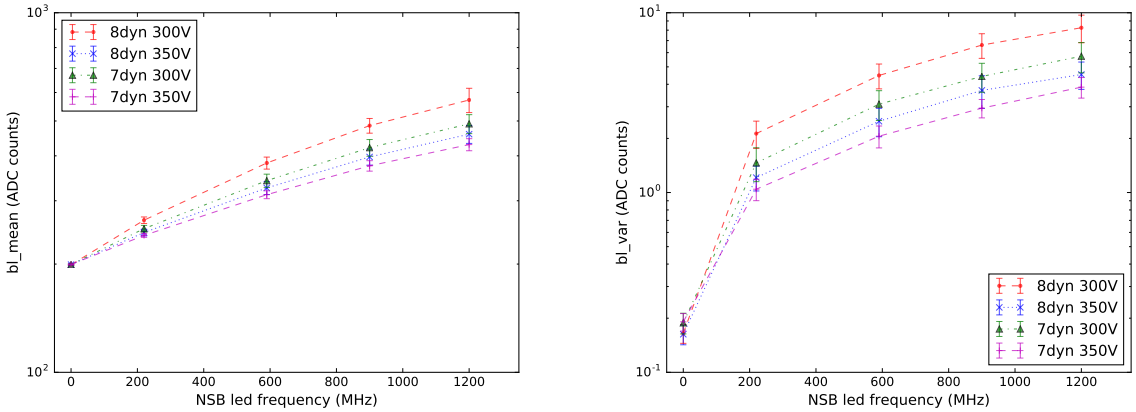

Figure 4.3: *Averaged values of the baseline bl_mean (left plot) and its variance bl_var (right plot) varying the NSB frequency for the different populations of PDP modules. See Sections 2.4 and 3.3 for a description of the measurement and the results of the analysis.*

formed. Depending on the confidence level that will be selected for the rejection, it will be possible to define a range for the acceptance (as well for rejection) of a PDP module comparing the performance of the new PDP modules with the results from the measurements of the first 86 PDP modules (see previous Section) perfomed in this work.

4.3 A comparison with the MST camera requirements

The CTA observatory released performance requirements for all the CTA telescopes and cameras, including the MST camera. The requirements are determined in order to be able to achieve the science goals for CTA. The requirements, that are discussed in this work, were defined by the Collaboration (2013).

The charge resolution is calculated as the broadness of the distribution of pzmax divided by the mean of the distribution. Since the the pzmax saturates in the high illumination regime, the charge resolution, in this work, is estimated only in the low and medium illumination regimes (μ <100 p.e.). Figure 4.4 shows the plots of the fractional charge resolution σ_Q/Q for the different type of PMTs (top) and for each single PMT (bottom) in the case of no NSB light (plots on the left) and in the presence of NSB light (plots on the right). For a comparison the requirements and goal for the charge resolution of the medium-sized telescopes as well the Poisson limit (corresponding to $\sqrt{Q}/Q$) are plotted.

The measured fractional charge resolution is in the entire range below the CTA requirements. This is valid averaging the PMT of each population of PDP modules as well also for each single PMT. In particular if at low charge (low illumination) the fractional charge resolution is placed between the CTA resuirements and CTA goal, at high charge (high illumination) the fractional charge resolution is well below the CTA requirements and

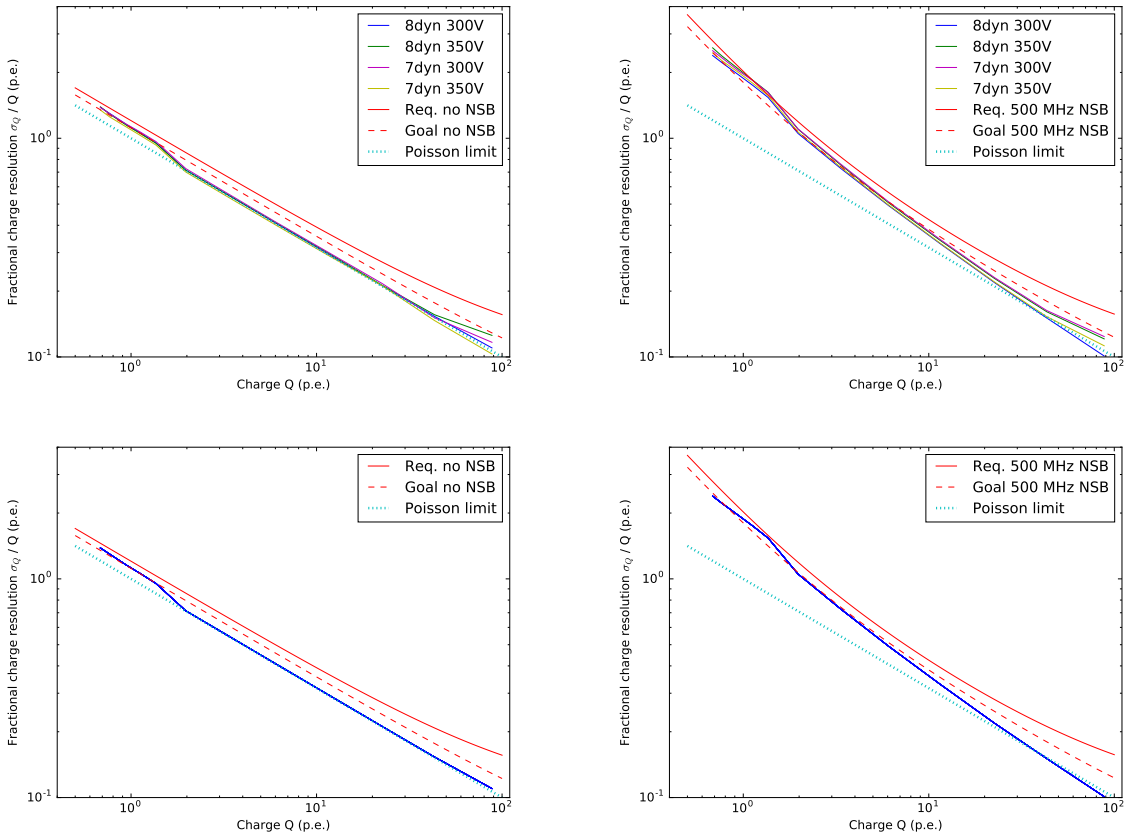

Figure 4.4: *Top: Fractional charge resolution averaged for each population of PDP modules, in the case of no NSB light (plot on the left) and in the presence of NSB light (plot on the right). Bottom: Fractional charge resolution for each PMT analyzed in this work in the case of no NSB light (plot on the left) and in the presence of NSB light (plot on the right). For a comparison the requirements and goal for the charge resolution of the medium-sized telescopes as well the Poisson limit are plotted.*

it approches the Poisson limit. Although this verification was not made using the entire FlashCam camera, for which the requirements were made, but only smaller part composed by three PDP modules, power supply and workstation, this result confirms the proper operation of all the PDP modules analyzed in this work. All the PDP modules, which have been tested and considered working well in this work, satisfy the general requirements for the cameras of the CTA medium-sized telescopes. A similar verification is planned to be done in Heidelberg where the entire FlashCam camera will be entire assembled and tested.

Appendix

Problem with the two modes of the laser

During the analysis of the PDP-module measurements an anomaly in the laser functionality was found. It was observed that, probably be due to the environment conditions (temperature, humidity etc.) or to the temperature of instruments (laser or FW), in some cases two different intensities are simultaneously present. Figure 4.5 shows the plots of the raw-data maximum values (maximum of each events) for a fixed illumination (FW position) in the high illumination regime.

The dispersion of the raw-data maximum instead of being a single Gaussian presents two separate distributions. On the plot of the left, where the raw-data maximum is plotted versus the event time, it is possible to observe that the two populations are present during the entire data acquisition (few minutes). It is not possible to see this feature in the low illumination regime due to the broadness of the event maximum distribution. It was verified with measurements performed in different periods that this inconvenience does not come from temperature variation. To avoid this problem it was planned to insert a quick check of the laser stability before starting each PDP-module measurement.

Varying the NSB light

Figure 4.6 contains the plots for each fixed NSB frequency: 0 MHz, 130 MHz, 340 MHz, 530 MHz and 690 MHz.

Summary plots

In this part additional plots of the summary results regarding the measurements of the first 86 PDP modules are presented. In Figure 4.7 are showed some plots about the values of intsum, pzmax, baseline and its sigma measured for each of all the PMTs measured with the ECAP experimental setup: 1032 PMTs corresponding to 86 PDP modules.

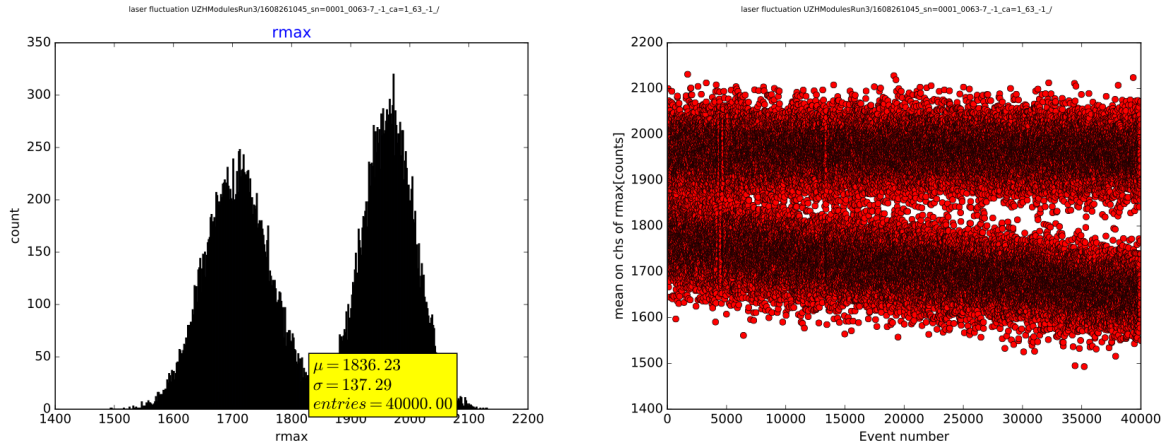

Figure 4.5: *Left plot: distribution of the of raw data maximum value for a fixed illumination (FW=1400). Right plot: distribution of the of raw data maximum values plotted versus time (events) for a fixed illumination (FW=1400).*

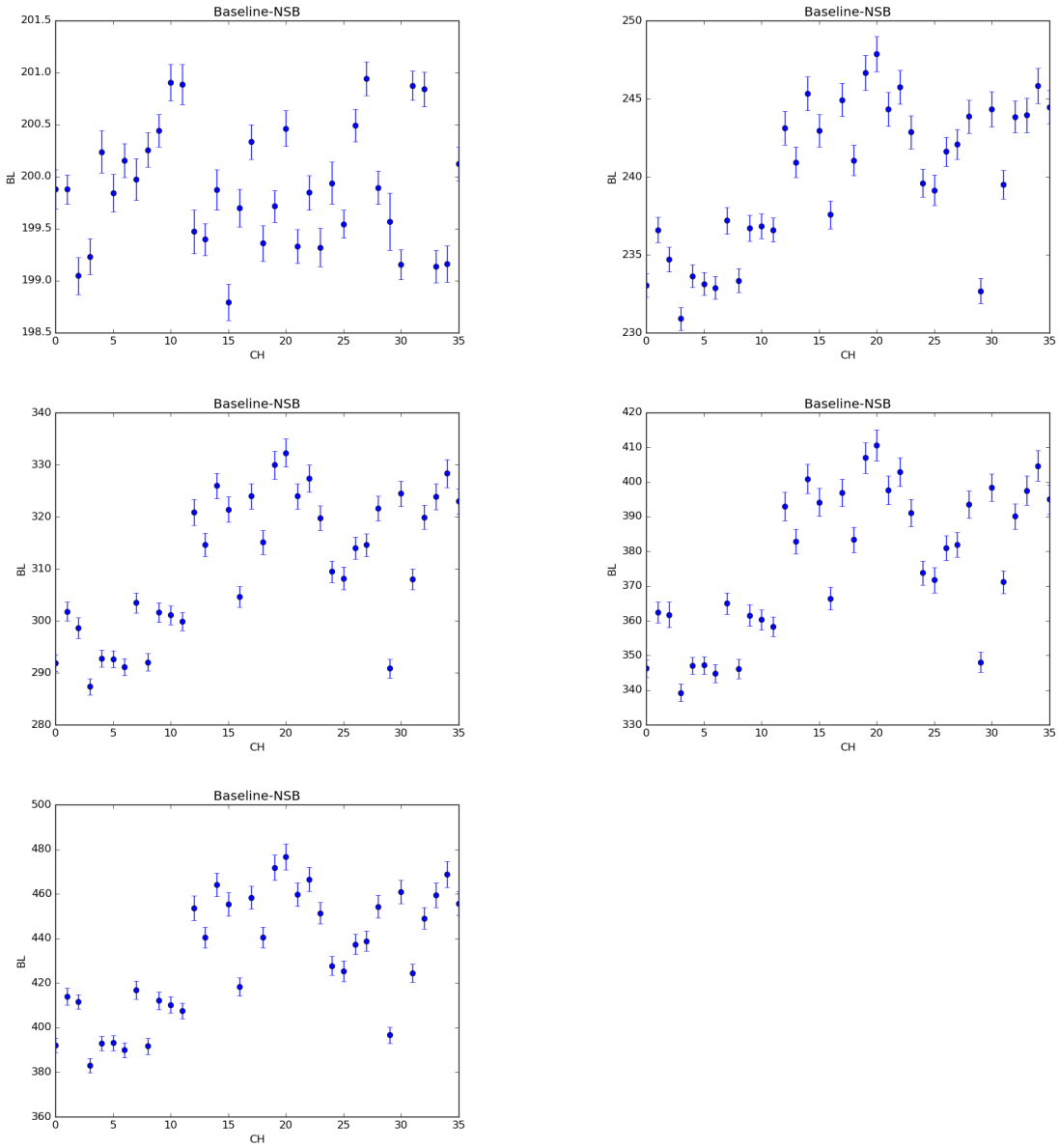

Figure 4.6: *Distribution of the of baseline varying the frequency of the NSB LED. In the plots are plotted for each channel the variation of the baseline varying the frequency of the NSB LED: 0 MHz (top left plot), 220 MHz (top right), 590 MHz (middle left), 900 MHz (middle right) and 1200 MHz (bottom). Increasing the background illumination it is possible to distinguish two types of PMT mounted in the PDPs modules: the first module contains twelve 8 dynodes 350 V PMTs, the second and the third modules contain instead twelve 8 dynodes 300 V PMTs.*

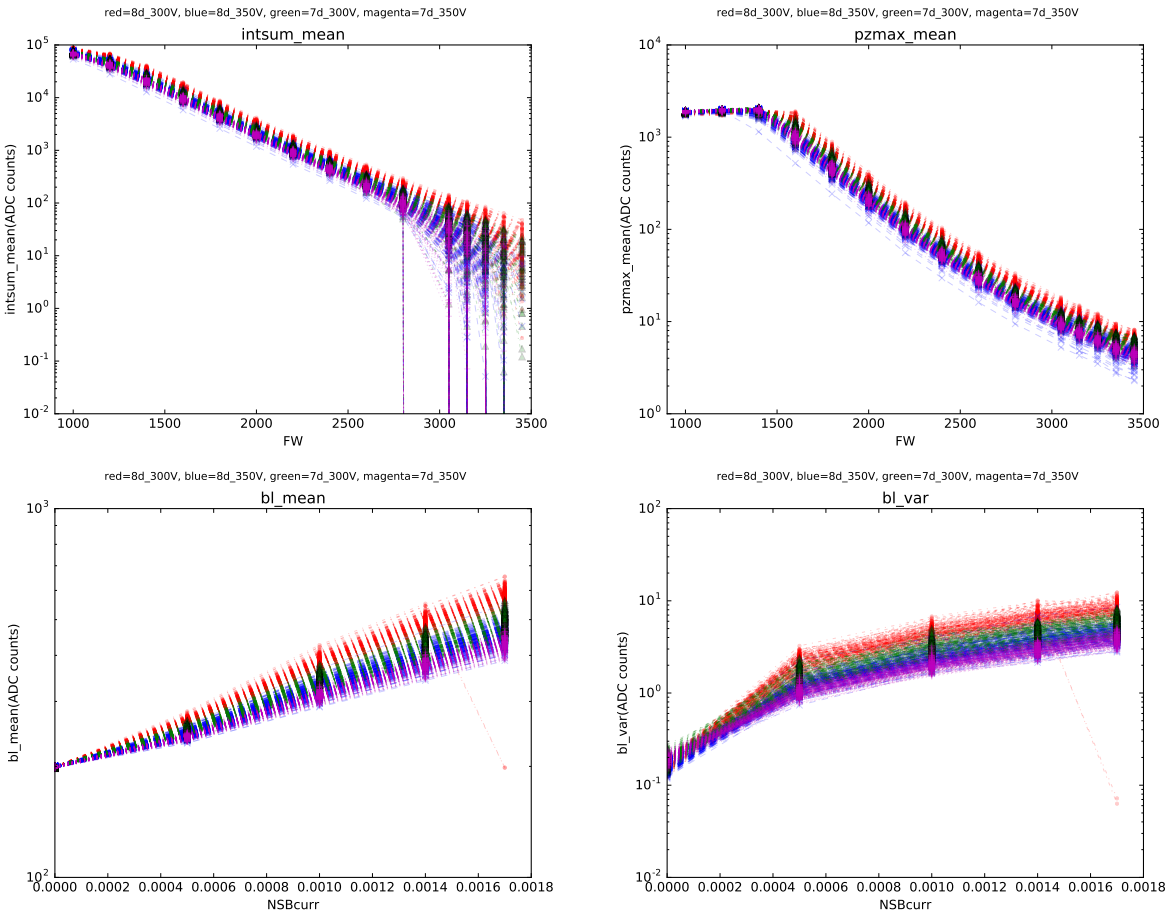

Figure 4.7: *Top plots: distributions of pzmax (on the left) and intsum (on the right) varying the intensity of the illumination (FW values) in case of no NSB light. Bottom plots: distributions of the of baseline (on the left) and its sigma/broadness (on the right) varying the frequency of the NSB LED. In the plots the different types of PMTs are plotted with different colors: in red the 8 dynodes 300 V PMTs, in blue the 8 dynodes 350 V PMTs, in green the 7 dynodes 300 V PMTs and in magenta the 7 dynodes 350 V PMTs.*

Bibliography

Abbott, B. P., Abbott, R., Abbott, T. D., et al. 2017, ApJ, 848, L12

Abdo, A. A., Ackermann, M., Ajello, M., et al. 2009a, Astroparticle Physics, 32, 193

Abdo, A. A., Ackermann, M., Ajello, M., et al. 2009b, Phys. Rev. D, 80, 122004

Abdo, A. A., Ajello, M., Allafort, A., et al. 2013, ApJS, 208, 17

Abdo A. A., e. a. F.-L. C. 2009, Phys. Rev. D, 80

Acero, F., Ackermann, M., Ajello, M., et al. 2015, ApJS, 218, 23

Acero, F., Ackermann, M., Ajello, M., et al. 2016, ApJS, 223, 26

Ackermann, M., Ajello, M., Albert, A., et al. 2012, ApJS, 203, 4

Ackermann, M., Ajello, M., Albert, A., et al. 2017a, ApJ, 840, 43

Ackermann, M., Ajello, M., Atwood, W. B., et al. 2015, ApJ, 810, 14

Ackermann, M., Ajello, M., Baldini, L., et al. 2017b, ApJ, 843, 139

Actis, M., Agnetta, G., Aharonian, F., et al. 2011, Experimental Astronomy, 32, 193

Aharonian, F., Akhperjanian, A. G., Bazer-Bachi, A. R., et al. 2006, A&A, 460, 365

Ajello, M., Atwood, W. B., Baldini, L., et al. 2017, ApJS, 232, 18

Aleksić, J., Ansoldi, S., Antonelli, L. A., et al. 2016, Astroparticle Physics, 72, 76

Ambrosi, G., Awane, Y., Baba, H., et al. 2013, ArXiv e-prints

Antonucci, R. 1993, ARA&A, 31, 473

Arons, J. 1981, in IAU Symposium, Vol. 95, Pulsars: 13 Years of Research on Neutron Stars, ed. W. Sieber & R. Wielebinski, 69–85

Atkins, R., Benbow, W., Berley, D., et al. 2000, Nuclear Instruments and Methods in Physics Research A, 449, 478

Atoyan, A. M., Aharonian, F. A., & Völk, H. J. 1995, Phys. Rev. D, 52, 3265

Atwood, W., Albert, A., Baldini, L., et al. 2013, ArXiv e-prints

Atwood, W. B., Abdo, A. A., Ackermann, M., et al. 2009, ApJ, 697, 1071

Baldini, L. et al. 2007, AIP Conf. Proc., 921, 190

Bellamy, E. H., Bellettini, G., Gervelli, F., et al. 1994, Nucl. Instrum. Meth., A339, 468

Bernlöhr, K. 2008, Astroparticle Physics, 30, 149

Bignami, G. F., Boella, G., Burger, J. J., et al. 1975, Space Science Instrumentation, 1, 245

Bignami, G. F. & Hermsen, W. 1983, ARA&A, 21, 67

Breiman, L., Friedman, J. H., Olshen, R. A., & Stone, C. J. 1984, Classification and Regression Trees (Monterey, CA: Wadsworth and Brooks)

Bretz, T. & Ribordy, M. 2013, Astroparticle Physics, 45, 44

Brown, A. M., Abchiche, A., Allan, D., et al. 2016, in Proc. SPIE, Vol. 9906, Ground-based and Airborne Telescopes VI, 99065K

Calabretta, M. R. & Greisen, E. W. 2002, A&A, 395, 1077

Caraveo, P. A. 2014, ARA&A, 52, 211

Cheng, K. S., Ho, C., & Ruderman, M. 1986, ApJ, 300, 500

Cherenkov Telescope Array Consortium, T., :, Acharya, B. S., et al. 2017, ArXiv e-prints

Chiang, J. & Romani, R. W. 1994, ApJ, 436, 754

Clifton, T. R., Lyne, A. G., Jones, A. W., McKenna, J., & Ashworth, M. 1992, MNRAS, 254, 177

Collaboration, C. C. 2013, CTA internal note, 80

Cordes, J. M. & Lazio, T. J. W. 2002, ArXiv Astrophysics e-prints

CTA Consortium, T. 2017, ArXiv e-prints

Damiani, F., Maggio, A., Micela, G., & Sciortino, S. 1997, ApJ, 483, 350

Daubechies, D. 1992, Ten Lectures on Wavelets

Davis, J. E. 2001, ApJ, 548, 1010

De Angelis, A., Tatischeff, V., Grenier, I. A., et al. 2017a, ArXiv e-prints

De Angelis, A., Tatischeff, V., Tavani, M., et al. 2017b, Experimental Astronomy, 44, 25

De Angelis, A., Tatischeff, V., Tavani, M., et al. 2017c, Experimental Astronomy

Fichtel, C. E., Hartman, R. C., Kniffen, D. A., et al. 1975, ApJ, 198, 163

Finley, J. P., Srinivasan, R., & Park, S. 1996, ApJ, 466, 938

Funk, S. 2015, Annual Review of Nuclear and Particle Science, 65, 245

G., H. 1990, Dissertation Thesis

Galbraith, W. & Jelley, J. V. 1953, Nature, 171, 349

Ghisellini, G., Righi, C., Costamante, L., & Tavecchio, F. 2017, MNRAS, 469, 255

Giommi, P., Padovani, P., Polenta, G., et al. 2012, MNRAS, 420, 2899

Glicenstein, J.-F. & Shayduk, M. 2017, in American Institute of Physics Conference Series, Vol. 1792, 6th International Symposium on High Energy Gamma-Ray Astronomy, 080009

Goldreich, P. & Julian, W. H. 1969, ApJ, 157, 869

Górski, K. M., Hivon, E., Banday, A. J., et al. 2005, ApJ, 622, 759

Grenier I.A., e. a. F.-L. C. 2005, science, 307

Grondin, M.-H., Funk, S., Lemoine-Goumard, M., et al. 2011, ApJ, 738, 42

H. E. S. S. Collaboration, Abdalla, H., Aharonian, F., et al. 2018, ArXiv e-prints

Harding, A. K. & Kalapotharakos, C. 2017, in Proceedings of the 7th International Fermi Symposium

Hartman, R. C., Bertsch, D. L., Bloom, S. D., et al. 1999, ApJS, 123, 79

Hartman, R. C., Bertsch, D. L., Fichtel, C. E., et al. 1992, in NASA Conference Publication, Vol. 3137, NASA Conference Publication, ed. C. R. Shrader, N. Gehrels, & B. Dennis

HAWC Collaboration, Abeysekara, A. U., Alfaro, R., et al. 2013, ArXiv e-prints

IceCube Collaboration, Aartsen, M. G., Ackermann, M., et al. 2018, Science, 361, eaat1378

Jelley, J. V. & Porter, N. A. 1963, QJRAS, 4, 275

Kellermann, K. I., Sramek, R., Schmidt, M., Shaffer, D. B., & Green, R. 1989, AJ, 98, 1195

Klebesadel, R. W., Strong, I. B., & Olson, R. A. 1973, ApJ, 182, L85

Kozłowski, S. 2017, ApJS, 228, 9

Kraushaar, W. L. & Clark, G. W. 1962, Physical Review Letters, 8, 106

Kraushaar, W. L., Clark, G. W., Garmire, G. P., et al. 1972, ApJ, 177, 341

Kuiper, L. & Hermsen, W. 2015, MNRAS, 449, 3827

Maccarone, M. C. 2017, ArXiv e-prints

Mattox, J. R., Bertsch, D. L., Chiang, J., et al. 1996, ApJ, 461, 396

McEnery, J. E. 2017, in AAS/High Energy Astrophysics Division, Vol. 16, AAS/High Energy Astrophysics Division #16, 103.13

Meagher, K. J. 2014, in Proc. SPIE, Vol. 9145, Ground-based and Airborne Telescopes V, 914533

Meegan, C., Lichti, G., Bhat, P. N., et al. 2009, ApJ, 702, 791

Mirzoyan, R., Mï¿½ller, D., Toyama, T., et al. 2016, PoS, PhotoDet2015, 018

Morrison, P. 1958, Il Nuovo Cimento, 7, 858

Nisa, M. U. 2018, PoS, ICRC2017, 340

Orlando, E., Johannesson, G., Moskalenko, I. V., Porter, T. A., & Strong, A. 2017, ArXiv e-prints

Özel, F., Psaltis, D., Narayan, R., & Santos Villarreal, A. 2012, ApJ, 757, 55

Park, N. & VERITAS Collaboration. 2015, in International Cosmic Ray Conference, Vol. 34, 34th International Cosmic Ray Conference (ICRC2015), 771

Porth, O., Vorster, M. J., Lyutikov, M., & Engelbrecht, N. E. 2016, MNRAS, 460, 4135

Principe, G., Hinton, J., MItchell, A., Parson, D., & Funk, S. 2019, in preparation

Principe, G. & Malyshev, D. 2016, ArXiv e-prints

Principe, G. & Malyshev, D. 2017, in American Institute of Physics Conference Series, Vol. 1792, 6th International Symposium on High Energy Gamma-Ray Astronomy, 070016

Principe, G., Malyshev, D., Ballet, J., & Funk, S. 2018a, in preparation

Principe, G., Malyshev, D., Ballet, J., & Funk, S. 2018b, A&A, 618, A22

Principe, G., Malyshev, D., & Funk, S. 2018c, ArXiv e-prints

Puehlhofer, G., Bauer, C., Bernhard, S., et al. 2015, in International Cosmic Ray Conference, Vol. 34, 34th International Cosmic Ray Conference (ICRC2015), ed. A. S. Borisov, V. G. Denisova, Z. M. Guseva, E. A. Kanevskaya, M. G. Kogan, A. E. Morozov, V. S. Puchkov, S. E. Pyatovsky, G. P. Shoziyoev, M. D. Smirnova, A. V. Vargasov, V. I. Galkin, S. I. Nazarov, & R. A. Mukhamedshin, 1039

Pühlhofer, G. 2017, in American Institute of Physics Conference Series, Vol. 1792, 6th International Symposium on High Energy Gamma-Ray Astronomy, 080002

Pühlhofer, G., Bauer, C., Biland, A., et al. 2012, in American Institute of Physics Conference Series, Vol. 1505, American Institute of Physics Conference Series, ed. F. A. Aharonian, W. Hofmann, & F. M. Rieger, 777–780

Pühlhofer, G. & for the H. E. S. S. collaboration. 2018, ArXiv

Schönfelder, V., Bennett, K., Blom, J. J., et al. 2000, A&AS, 143, 145

Slane, P. 2017, Pulsar Wind Nebulae, ed. A. W. Alsabti & P. Murdin, 2159

Smith, D. A., Guillemot, L., Kerr, M., Ng, C., & Barr, E. 2017, ArXiv e-prints

Sreekumar, P., Bertsch, D. L., Dingus, B. L., et al. 1998, ApJ, 494, 523

Sturrock, P. A. 1971, ApJ, 164, 529

Swanenburg, B. N., Bennett, K., Bignami, G. F., et al. 1981, ApJ, 243, L69

Takahashi, M., Inome, Y., Yoshii, S., et al. 2018, Nuclear Instruments and Methods in Physics Research A, 894, 1

Tavani, M., Barbiellini, G., Argan, A., et al. 2009, A&A, 502, 995

Thompson, D. J. 2004, in Astrophysics and Space Science Library, Vol. 304, Cosmic Gamma-Ray Sources, ed. K. S. Cheng & G. E. Romero, 149

Toyama, T., Mirzoyan, R., Dickinson, H., et al. 2013, ArXiv e-prints

Urry, C. M. & Padovani, P. 1995, PASP, 107, 803

Völk, H. J. & Bernlöhr, K. 2009, Experimental Astronomy, 25, 173

W., S. S. 1997, The Scientist and Engineer?s Guide to Digital Signal Processing

Wakely, S. P. & Horan, D. 2008, International Cosmic Ray Conference, 3, 1341

Weekes, T. C., Cawley, M. F., Fegan, D. J., et al. 1989, ApJ, 342, 379

Werner, F., Bauer, C., Bernhard, S., et al. 2017, Nuclear Instruments and Methods in Physics Research A, 876, 31

Wood, M., Caputo, R., Charles, E., et al. 2017, ArXiv e-prints